University of Alberta

Radio Frequency Noise Studies for a linac-MRI System

by

Michael Joseph Lamey

A thesis submitted to the Faculty of Graduate Studies and Research
in partial fulfillment of the requirements for the degree of

Doctor of Philosophy
in
Medical Physics

Department of Physics

Spring 2010
Edmonton, Alberta

Examining Committee

Dr. Gino Fallone, Physics\Oncology, University of Alberta

Dr. Satyapal Rathee, Oncology, University of Alberta

Dr. Nicola De Zanche, Oncology, University of Alberta

Dr. Richard Marchand, Physics, University of Alberta

Dr. Sharon Morsink, Physics, University of Alberta

Dr. James Balter, Radiation Oncology, University of Michigan

Abstract

A prototype system which has integrated a linear accelerator (linac) with a magnetic resonance imager (MRI) has been constructed at the Cross Cancer Institute. The real time operation of a linac-MRI system will require proper radio frequency (RF) shielding such that the MRI images can be acquired without extraneous RF noise from the linac. This thesis reports on the steps taken to successfully RF-shield the linac from the MRI such that the two devices can operate independently of one another. The RF noise from functioning multileaf collimators (MLC) is measured using near field probes and MRI images are acquired with the MLC near the MRI. This included measuring the RF noise as a function of applied magnetic field strength. Several measurement and simulation scenarios are discussed to determine the major sources of RF noise generation from the modulator of a linac. Finally RF power density levels are reported internally and externally to the RF cage which houses the linac and the MRI. The shielding effectiveness of the RF cage has been measured in the frequency range 1 – 50 MHz and is presented. MRI images of two phantoms are presented during linac operation.

The MLC studies illustrate that the small RF noise produced by functioning MLC motors can be effectively shielded to avoid signal-to-noise degradation in the MRI image. A functioning MLC can be incorporated into a linac-MRI unit. The RF noise source investigations of the modulator of a linac illustrate that the major source of RF noise involves the operation of a magnetron. These studies also eliminate the pulse forming network (PFN) coil and the grid voltage spikes on the thyratron as possible major sources of RF noise. The main result is that for linac-MRI systems the modulator of a linac should be housed in a separate RF cage from the MRI. Finally imaging work with the linac operating illustrates that the accelerating structure of a linac and an MRI can be housed within the same RF cage. The 6 MV linac can be operated to produce radiation with no experientially measurable degradation in image quality due to RF effects.

Acknowledgements

Many people have contributed to the work presented in this thesis. Dr. Rathee provided excellent supervision throughout. Dr. Carlone supervised the work presented in Chapter 2 and parts of chapter 4. Dr. DeZanche provided excellent knowledge in the field of RF research. Thanks to the guys in the machine shop (Ken, Curtis and Gary) and the guys in RT service (Cory, Doug, Dan and Jason) for answering or attempting to answer my many questions and help out with all the hardware related work. A special thanks to Emanuel for the assisting in much of the work presented in chapters 3, 4 and 5.

Ben, you've been an awesome friend and a great person to work with. I'll miss our regular morning discussions! I couldn't have asked for a better student and friend to come in at the same time with, good luck finishing up and all the best in the future. Thanks to all the other graduate students for being great sports and putting up with my odd games; Amr, Artur, Dave, Donata, Jay, Joel, Leslie, Matt, Yingli, Ryan, Sandra, Tony. Sandra and Dave you will be remembered for your legendary discussions. Matt and Amr you will be remembered as the winners of a certain game.

Thank you to the department members at the Cross for teaching me over the years. Finally I would like to thank my supervisor Dr. Gino Fallone. Thanks for putting me on a great project and setting me up to succeed. Thanks for the supervision over the years of study.

Table of Contents

List of Tables

List of Figures

Figure 4.33: Measured inductance of the saturable reactor as a function of applied current through the DC winding around the reactor.
Figure 4.34: Measured RF power spectral density from the modulator with and without saturable reactors placed along the two grid lines of the thyratron.

Figure 5.1: Plan view of the prototype linac-MRI system at the Cross Cancer Institute illustrating the layout of the RF cage, MRI, linac, modulator cabinet, waveguide and MRI hardware.

Figure 5.2: Setup used to measure the shielding effectiveness of the RF cage housing the linac-MRI system. Loop antennas were used to measure the H field SE while rod antennas were used to measure the E field SE.

Figure 5.3: Measured power spectral density externally and internally to our RF cage while the linac produced radiation. The data shown is in 50 kHz bin widths.

Figure 5.4: Measured shielding effectiveness of the RF cage housing our linac-MRI prototype system. The shielding effectiveness was measured using a set of loop antennas for the H field and a set of rod antennas for the E field.

Figure 5.5: MRI images of a right rectangular prism phantom, (left) linac not producing radiation (right) linac producing radiation with lead blocking the coil from the x-ray radiation.

Figure 5.6: MRI k-space data of the images shown in Figure 5.5, (left) linac not producing radiation (right) linac producing radiation with proper RF shielding.

Figure 5.7: MRI images of a gel phantom, (left) linac not producing radiation (right) linac producing radiation with lead blocking the coil from the x-ray radiation.

Figure 5.8: k-space data of the images shown in Figure 5.7, (left) linac not producing radiation (right) linac producing radiation with proper RF shielding.

Figure 5.9: k-space data of the first (left) and second (right) phantoms taken during linac pulsing while the RF shielding was insufficient. The data illustrates a “line” in k-space from the RF picked up by the MRI coil.

Figure A.1: General definition of the setup of a arbitrary current distribution.

Figure A.2: The two main probes used in this work. The electric field probe (left) and the magnetic field probe (right) [© Rohde and Schwarz, 2009 with permission].

Figure A.3: Performance factors for the electric field probe (left) and the magnetic

List of Abbreviations

CBCT	Cone beam computed tomography
CT	Computed tomography
CTV	Clinical tumour volume
DFT	Discrete Fourier transform
E	Electric (field)
EPID	Electronic portal imaging device
GTV	Gross tumour volume
H	Magnetic (field)
ICRU	International commission on radiological units
IM	Internal margin
IMRT	Intensity modulated radiotherapy
ITV	Internal target volume
KCL	Kirchoff’s current law
kV	Kilovoltage
LU	Lower upper
MLC	Multileaf collimator
MRI	Magnetic resonance imager
MV	Megavoltage
OBI	On board imager
OR	Organ at risk
PET	Positron emission tomography
PFN	Pulse forming network

PML	Perfectly matched layer
PRV	Planning organ at risk volume
PTV	Planning target volume
QA	Quality assurance
RF	Radio frequency
SE	Shielding effectiveness
SM	Setup margin
SNR	Signal to noise ratio
SPECT	Single photon emission computed tomography
SPICE	Simulation program with integrated circuit emphasis
SR	Saturable reactor
T	Tesla
TLM	Transmission line matrix
VHF	Very high frequency
VMAT	Volumetric modulated arc therapy

Chapter 1: Introduction

1.1 Introduction and Background

The Canadian cancer society has estimated that 171,000 new cases of cancer and 75,300 cancer related deaths will occur in the year 2009 [Canadian Cancer society 2009]. In the 2004 annual report [Canadian Cancer Society 2004] it was estimated that by 2010 Cancer related deaths will surpass heart disease as the number one leading cause of death in Canada. These statistics speak to the importance of research and development into new and innovative cancer treatment solutions.

The goal of the radiotherapy process is to maximize curing potential while simultaneously minimizing possible future complications. This goal is accomplished by delivering a uniform radiation dose to the entire tumour and by sparing normal tissue. The use of image guided radiotherapy is a step toward this ultimate goal. Complications arise due to the fact that there are several sources of geometrical errors involved in the radiotherapy process. These can consist of setup variation of the patient on the treatment couch, organ movement which can occur intrafraction or interfraction, organ movement which can occur due to breathing motion, organ filling and peristalsis. It is well known that organ motion occurs from day to day [Booth et al. 1999, Hector et al. 2000, Langden et al. 2001 and Rietzel et al. 2004].

Significant work has been undertaken in the past decade in the area of image guided radiotherapy (IGRT); the multitude of review articles in this area of research attests to this [Bucci et al. 2005, Dawson et al. 2006, Dawson et al. 2007, Mackie et al. 2003, Mageras et al. 2005, Meyer et al. 2007, Sharpe et al. 2007, Verellen et al. 2007 and Verellen et al. 2008]. Fundamentally, 2D or 3D images of the patient are obtained at the time of patient setup before the treatment. These images are then registered to the similar or transformed images from the planning computed tomography (CT) images of the patient. Thus the patient is aligned to the treatment beam using the images taken just before the treatment instead of relying upon skin markers. The skin marks are known to move independently of the internal patient anatomy and do not provide an accurate or precise method of aligning the patient to the treatment beams. The rationale for research and advancements into image guided radiotherapy is evident from the improvements in tumor control and reductions in normal tissue complications [Eisbruch et al. 1999, Ghilezan et al. 2004 and Song et al. 2005].

Correction strategies that are used to align the patient with the treatment beam can be classified as either offline or online techniques. Offline techniques involve the acquisition of images while the patient is set up on the treatment couch. However, many fractions are delivered to the patient before the acquired images are used to perform a statistical analysis of the systematic and random errors involved in the overall patient's setup error. A correction is then made for the remaining treatment fractions. Online techniques involve daily imaging while the patient is setup on the treatment couch, any deviations from the expected patient position is then addressed.

1.2 Current Image Guidance Techniques

1.2.1 Megavoltage Electronic Portal Imaging

Currently the most widespread [Verellen et al. 2007] device used for image guidance is the Electronic Portal Imaging Device (EPID) [Antonuk et al. 2002 and Herman et al. 2001]. The radiotherapy beam can be used with an amorphous silicon panel to provide megavoltage (MV) patient radiographic images. The main advantage of on-board EPID systems is that the actual treatment beam is used for imaging so no transformation between the treatment and imaging coordinates is required. The EPID can be used for verification of dose as calculated during treatment planning and for quality assurance [Hansen 1996 et al. and van Zijtveld et al. 2006]. Drawbacks of the technology are that the images are of poor contrast due to the 2D projection of 3D patient anatomy and the use of MV x-rays; especially for soft tissues.

1.2.2 Optical Tracking

A system consisting of an infrared camera and a reflecting device placed on the patient can be used to track the patient's skin placement during the treatment. It is generally assumed that the motion of the reflecting device placed on the patient skin is a good indicator of the position of the diseased volume. The device is simple and is popular for use of tracking motion due to breathing. However, no patient image is obtained and the accuracy of external markers, in terms of being a good surrogate of tumour motion, has been questioned [Hoisak J. D. et al. 2004].

1.2.3 Radio Frequency Tracking

A recent technology involves a system for real time tracking of tumour position with the use of implanted radio frequency (RF) transponders [Litzenburg et al. 2007 and Seiler et al. 2000]. The position of the transponders is monitored using an external antenna array. The real time position of the tumour volume is related to the position of the transponders. Drawbacks of the system include the invasiveness of the implanted transponders and a lack of 3D imaging of the patient anatomy.

1.2.4 Stereotaxic Radiotherapy

Stereotaxic radiotherapy involves target localization using a three dimensional coordinate system to precisely direct radiation. The concept was first introduced by Leksell [Leksell 1951]. The process consists of directing large quantities (as compared to the fractionated radiotherapy process) of focused radiation at the target. The focus of stereotaxic radiotherapy is benign and malignant brain tumors [Podgorsak et al. 1989 and Wu 1992]. Three dominant systems are used clinically for stereotaxic radiotherapy: Gamma Knife manufactured by Elekta (Elekta, Stockholm, Sweden), CyberKnife manufactured by Accuray (Accuray, Sunnyvale, California, USA) and the Novalis system manufactured by BrainLAB (BrainLAB, Feldkirchen, Germany).

The Gamma Knife system consists of 201 ^{60}Co sources for treatment; these sources are located along a ring geometry around an isocenter. A patient is fitted with a head frame, and an MRI or CT image is acquired and 3-D localization of the tumour is established with respect to the head frame. Before treatment, the head frame is attached to the Gamma knife which localizes the tumour position. Advantages of the system include: minimal preventative maintenance and simple QA. While disadvantages include: the Cobalt source decay and reload, and a lower patient throughput.

The Cyberknife system [Antypas et al. 2009] involves the use of robotic arms with 6 degrees of freedom and a 6 MV linac to deliver the radiation. The Cyberknife image tracking system consists of two diagnostic x-ray sources mounted 90° with respect to one another above the patient. There are three tracking options; a skull based system uses the patient skull as a reference, and a fiducial system with markers that either move or do not move with respect to patient breathing motion. Advantages of the Cyberknife system include: improved dose uniformity over Gamma Knife, higher patient volume than Gamma Knife and versatility in treatment planning (ioscentric and nonisocentric). Disadvantages include: longer treatment times, more involved QA and more preventative maintenance than Gamma Knife.

The BrainLAB system consists of a commercially available Varian (Varian medical systems, Palo Alto California, USA) Trilogy linac for treatment and a 120 leaf multileaf collimator (MLC) for radiation sculpting. The system includes a room mounted ExacTrac x-ray 6D imaging system for tumour tracking. The ExacTrac system tracks infrared external markers. Two kV sources with two amorphous silicon flat panel imagers are used to check the setup isocenter [Yin et al. 2004]. Advantages of the system include: better dose uniformity than Gamma Knife of Cyberknife, the capability of fractionation and highest patient volume.

Disadvantages include: higher preventative maintenance and more QA than Gamma Knife.

1.2.5 kV Imaging

When compared to MV imaging, kilo voltage (kV) imaging offers better images due to superior contrast of bones and implanted markers. kV imaging systems are designed to localize bony anatomy or markers. Fluoroscopy, for real-time marker or bone tracking, is available with kV imaging. Localization is attained by taking at least two radiographs at two distinct known angles. The system can be attached to the linac [Biggs et al. 1985] or room based [Schewe et al. 1998]. A three dimensional system will consist of x-ray sources and corresponding fluoroscopic image intensifiers [Shirato H. et al. 2000]. kV imaging has the advantages over MV imaging that for a given contrast the dose delivered by kV imaging is less. Disadvantages of a kV imaging system are that they are not along the MV treatment axis, a kV system introduces a third isocenter which must be maintained with the linac and laser isocenter and like an MV image the patient receives an additional dose beyond the treatment dose.

1.2.6 Ultrasound

The use of ultrasound for patient setup can be advantageous. Ultrasound can provide images of superior soft tissue contrast to that of computed tomography (CT) images in certain locations such as prostate [Sharpe et al. 2007]. Ultrasound systems for prostate image guidance have been investigated [Holupka et al. 1996 and Lattanzi et al. 1999]. A drawback of ultrasound is that there can be user variability [Artignnan et al. 2004 and Langen et al. 2003].

1.2.7 Tomotherapy

Tomotherapy (Tomotherapy, Madison, Wisconsin, USA) is a treatment system in which radiation is delivered in a slice-by-slice fashion using a 6 MV linac [Mackie et al. 1993 and Mackie et al. 1999]. The patient is slowly moved through the system bore while being treated using intensity modulated radiation therapy (IMRT, IMRT will be discussed in section 1.3). Essentially the unit is a CT scanner whose diagnostic x-ray tube has been replaced with a 6 MV linac and whose collimating has been replaced with binary multileaf collimators (MLC). The binary MLC positions change as a function of gantry angle, thus allowing for a multitude of degrees of freedom while producing a conformed dose distribution to the cancerous volume. The unit has MV CT imaging based on fan beam and helical acquisition; the MV images taken just before the treatment allow for patient positioning, tumour alignment and dose verification [Langen et al. 2005 and Welsh et al. 2004]. A disadvantage of Tomotherapy includes longer QA to verify dose delivery on specific patient plans.

1.2.8 Cone Beam Computed Tomography

Cone beam computed tomography (CBCT) systems allow for volumetric images to be obtained with a 2D device such as an EPID. Many, typically hundreds [Sharpe et al. 2007, Dawson et al. 2006], 2D projections are taken and a 3D image of the patient can be obtained; this is referred to as image reconstruction from cone beam projections [Feldkamp et al. 1984]. Furthermore the addition of an orthogonally mounted x-ray source, used in conjunction with a flat panel imager, can produce images with good spatial resolution and soft tissue contrast [Jaffray et al. 2002]. kV cone-beam image reconstruction has been used to verify patient setup [Godfrey et al. 2006 and McBain et al. 2006]. A draw back of this system is that volumetric imaging is limited to patient setup before treatment begins [Verellen et al. 2007]. These systems are available commercially on linac units; for example the on board imager (OBI) on Varian units and Synergy systems on Elekta Oncology systems.

1.3 Radiation Delivery Techniques

A recent advancement in radiotherapy involves the implementation of intensity modulated radiotherapy (IMRT). IMRT spatially modulates radiation beam fluence using a dynamic MLC to sculpt radiation to the target of interest [Webb 2003]. A finite number of fields are used to treat a patient from different angles. If a large number of uniform circular radiation fields intersected at a common point the resulting dose distribution would be uniformly spherical, similarly if six uniformly square orthogonal fields were made to intersect at a common point the resulting 3d dose distribution would be a uniform cube. By modulating the fluence of particular intersecting beams, we can sculpt a radiation pattern to either miss critical structures or to apply a uniform dose to a cancerous volume of irregular shape.

Two technologies which implement the use of IMRT are Rapid Arc (a Varian technology) and Volumetric Modulated Arc Therapy (VMAT) (an Elekta technology) which uses a dynamic x-ray source rotation around the patient while the treatment beam is on (tomotherapy is the predecessor of this type of treatment delivery). Both technologies operate in a similar fashion treating a patient using IMRT in one rotation of the linac gantry; this is accomplished using variable dose rate, variable gantry speed, variable collimator angle and dynamic MLCs. The benefits of these technologies include decreased treatment delivery time and an increase in the number of degrees of freedom available to produce a conformed dose to a cancerous volume.

1.4 Linac-Magnetic Resonance Imaging system at the Cross Cancer Institute

As stated previously, improvements in patient outcome to radiation therapy have been evidenced over the past few decades due to improved image guidance using EPID, MVCT, MVCBCT, kV imaging, kV CBCT and ultrasound systems. However, some studies have shown that the use of additional imaging, capable of improved soft tissue contrast with reduced or zero radiation dose in image acquisition obtained near real-time, may be required to further improve the current target localization techniques [Chen et al. 2004 and Mah et al. 2002]. With its exquisite soft tissue delineation magnetic resonance imaging (MRI) is the ideal imaging tool.

Clinically, the International Comission on Radiation Units has produced a report [ICRU50 1993] which is used to account for patient organ motion and other setup errors. This report called for the definition of three target volumes: the gross target volume (GTV) which includes the visible or palpable extent of the diseased tissue, the clinical target volume (CTV) which includes the GTV plus a margin due to the microscopic extent of the tumour, and the planning target volume (PTV), that uses a setup margin (SM) around the CTV to account for day-to-day geometric variations in the tumour location. Difficulties arise in defining the PTV when a tumor is in close proximity to radiosensitive normal tissue (i.e. the prostate is near the bladder and rectum). The ICRU62 [ICRU 1999] report defined three further clinical sites: the internal target volume (ITV) which is used to account for target motion such as breathing motion enclosed in an internal margin (IM), the organ at risk (OR) which defines the volume of nearby organs and the planning organ at risk volume (PRV) which is an expansion of the OR to account for organ motion. These definitions are shown in Figure 1.1.

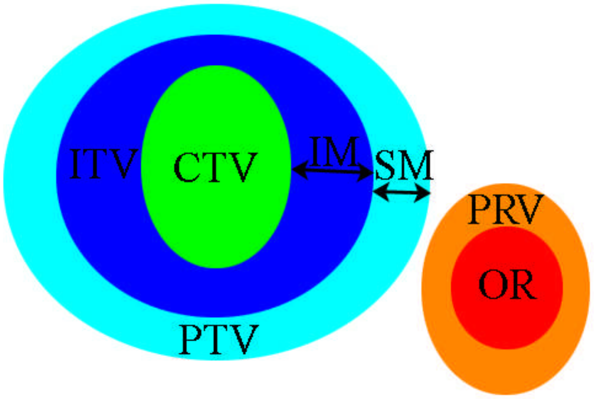

Figure 1.1: ICRU50/ICRU62 volume definitions when planning radiotherapy on a cancerous volume (IM is the internal margin, SM is the setup margin).

References [ICRU50 1993 and ICRU62 1999] provide some guidelines regarding the microscopic extent, internal and setup margins to arrive at a suitable PTV. However, [ICRU62 1999] states that “In practice, at present, the PTV must be delinated by the radiation oncology team based on experience and judgement drawn from observation and evaluation of the risk of failure and complications”.

The volumes illustrated in Figure 1.1 are those of an ideal case; it is not uncommon for the PRV and PTV to overlap. Problems occur in such a situation, since a minumim treatment dose is required for the PTV and a maximum limiting dose is prescribed for the PRV. These two requirements generally conflict with each other. Thus a comprimise is generally made where part of the PTV would not receive treatment dose. Statistically due motionof the CTV, this part of the PTV will be occupied by the CTV tumour cells for a certain fraction of the treatment duration. If the comprimise is reversed, i.e. the PTV is treated with the full treatment dose and the nearby healthy tissue receives a higher dose, then the limiting prescibed dose will result in an increased risk of treatment-related future complications. Clearly a system which could reduce the IM, SM and PRV margins would allow for greater separation between the PTV and OR resulting in larger healthy tissue sparing. Fundamentally, in order to reduce these margins with a high degree of confidence, knowledge of the tumour location with respect to the treatment beam *at times during irradiation* is required. This requirement has not been met by any of the aforementioned image guidance systems.

To this end a prototype linac-MRI unit has been constructed at the Cross Cancer Institute in Edmonton, Alberta. The attachment of an MRI to a linac is the key to providing clinically-usable image guidance. The MRI uses no mechanical rotation or radiation beam for imaging. Thus it is functionally and mechanically independent of the x-ray beam generation system of the linac. Contrary to most other imaging modalities, MRI can be used as often as desired since no additional ionizing radiation is delivered to the patient. The use of MR images provides the needed soft tissue contrast for target localization. The system consists of a 6 MV linac for radiotherapy treatment and a 0.22 T MRI for both pretreatment images and real-time image guided adaptive radiotherapy. The first MR images of a phantom acquired during simultaneous MV irradiation were reported by Fallone [Fallone et al. 2009]. The prototype design of the linac-MRI system is shown in Figure 1.2. A patient would lie on a couch between the MRI poles and then be treated using the 6 MV radiation.

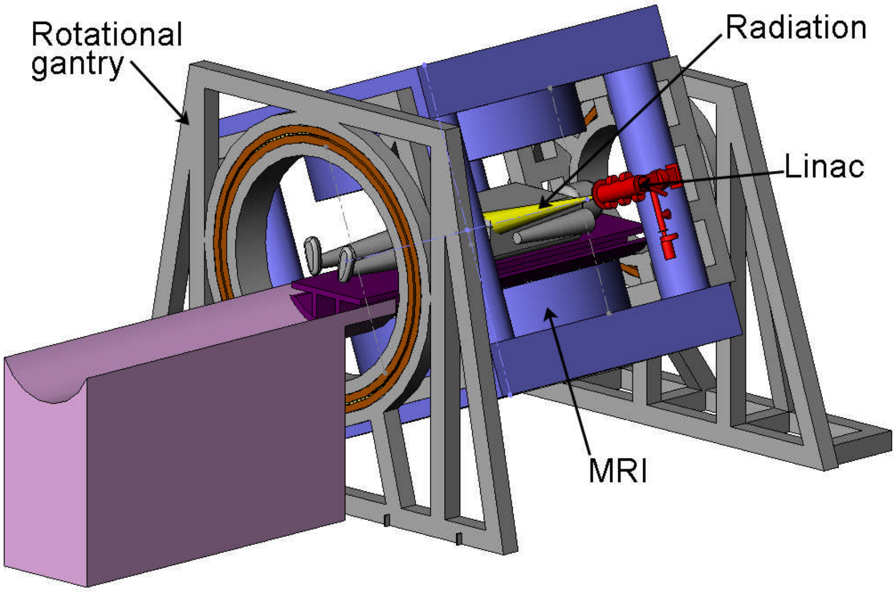

Figure 1.2: Human design of the linac-MRI system at the Cross Cancer Institute showing the relationship between the linac, MRI and rotational gantry. By permission from Emanuel Blosser.

1.5 Megavoltage Treatment-MRI System Integration Work at Other Institutions

Two other groups are currently developing a clinical system comprised of an MRI with megavoltage treatment: an integrated linac-MRI system from the University of Utrecht in the Netherlands and an MRI system integrated with cobalt sources from Viewray [Viewray Inc.].

The Netherlands group proposes the use of a superconducting solenoid magnet 1.5 T MRI [Lagendijk et al. 2008, Raaijmakers et al. 2008, Raaijmakers et al. 2007a, Raaijmakers et al. 2007b, Raaijmakers et al. 2007c, Raaijmakers et al. 2005 and Raaymakers et al. 2004] . The linac is mounted outside the magnet, perpendicular to its axis. The linac rotates about the stationary MRI and irradiates the patient by irradiating through the magnet. An advantage of the Netherlands group is the higher MRI field strength (the signal-to-noise ratio (SNR) is higher at higher fields). However, a disadvantage is the dosimetry problem at higher fields; the electron trajectories in the magnetic field are greatly affected producing deleterious hot and cold spots, particularly at air-tissue interfaces [Kirkby et al. 2008].

The Viewray system is comprised of an open split solenoid 0.3 T MRI and a three headed ^{60}Co γ-ray unit [Dempsey 2006 and Viewray Inc.] for treatment. The advantage of this design is that it avoids RF interference by utilizing three ^{60}Co sources, which do not operate using pulsed RF radiation. As well, this approach removes the possibility of a magnetic effect on the electron path in the accelerating structure of a linac (a large enough fringe field from the MRI could deflect the accelerated electrons). Disadvantages of this proposed system is that Cobalt is ferromagnetic, rotation of the source within the fringe field of the MRI may cause small variations in the field homogeneity, the lower energy of a Cobalt source does not provide satisfactory dose distribution for deep-seated tumours, there is a larger penumbra effect from the increased size of the source, the system requires greater maintenance and the source must be replaced approximately every 5 years by external contractors.

1.6 Research Motivation

Possible technical problems with the integration of the MRI and linac include: mutual magnetic interference; RF noise created by the linac interferes with the MRI and mechanical interference when rotating the linac about the patient and MRI. Magnetic fields of sufficient strength can deflect the electron beam into the side walls of the accelerating structures of the linac preventing them from reaching the x-ray production target. It can also interfere with the electron-beam steering process in the linac, just before the target (location of radiation field production for treatment).

In our prototype, the linac is coupled directly to the same gantry within the fringe field of the MRI system. This coupling removes the mechanical interference since the linac and MRI rotate together around the patient; however, magnetic and RF interferences must still be addressed. Research related to the magnetic interferences and more innovative designs of magnet systems suitable for linac mounting are being addressed in separate doctoral theses.

The linac is a source of pulsed RF noise [Burke et al. 2009]; these RF signals can interfere with the operation of the MRI because the MRI uses RF signals in its transmitting and receiving coils. Images are obtained using RF signals from the object to be imaged and are received at or near the Larmor frequency by the coil(s) of the MRI. These RF signals are used to produce an image, the RF noise produced by a linac can be picked up by the coil as well, and fed into the signal processing system of the MRI; this unwanted RF noise will produce deleterious image artefacts.

1.7 Thesis Outline

This work focuses on the RF issues pertaining to the integration of a linac with an MRI. The work was four-fold: (1) determination of the room effects on an RF source, (2) determination and elimination of RF interferences from an MLC, (3) determination or elimination of components in the modulator of a linac as RF sources and (4) shielding of RF noise for MR imaging while operating the 6 MV linac. Each of these will be addressed individually as separate chapters (chapters two-five). Each chapter will be structured as a self-contained manuscript including introduction and motivation, theory, materials and methods, results, discussion and conclusion.

Chapter two discusses simulations which were used to estimate the effect of an enclosed room on the distribution of RF fields from elementary RF antennas. The simulations were compared to measurements made with near field electric and magnetic field probes. The purpose of the study was to determine the magnitude of the effect that an enclosed environment has on the distribution of the RF field from a dipole antenna, when compared to the fields produced in a free space environment.

Chapter three pertains to the studies of the RF noise, produced by the operation of DC motors, from an MLC and the electromagnetic shielding of the MLC. Measurements of the RF power spectral density from current clinical motors, used to drive the leaves of the MLC, are presented. Next the effects of placing a functioning MLC close to the MRI of our linac-MRI system are shown. Images of a phantom are used to validate that an MLC system can be appropriately RF-shielded to prevent the production of image artefacts on MR images.

Chapter four presents the results of our work on the sources of RF noise within the modulator of a linac. The elements in the modulator of a linac are introduced. The goal of this work is to isolate the production of RF noise from the individual components in the modulator. This was accomplished by modeling the electronic components in the modulator and by measuring the RF noise from the modulator with a near field probe set.

Chapter five discusses the RF shielding for a linac-MRI system from the noise produced by the modulator of a linac. The purpose of the chapter was to acquire linac-noise free MR images of a phantom while radiation was simultaneously produced. The chapter discusses the RF shielding of the linac-MRI apparatus, shielding effectiveness studies of the RF cage and MR imaging during the time the linac produced radiation.

Chapter six will summarize and conclude the work presented in the thesis.

Five appendices are included: Appendix A outlines the antenna theory relevant to this work, Appendix B presents an introduction to the transmission line matrix method, Appendix C presents the basics of MRI theory, Appendix D introduces the techniques used in the SPICE simulation method and Appendix E summarizes our measurements of the electric and magnetic fields from a Siemens MD2 mevatron modulator.

1.8 References

Antonuk L. E., “Electronic Portal Imaging Devices: a Review and Historical Perspective of Contemporary Technologies and Research” Phys. Med. Biol. **47** R31-R65 2002.

Antypas C. and Pantelis E. “Performance Evaluation of a CyberKnife G4 Image-Guided Robotic Stereotactic Radiosurgery System” Phys. Med. Biol. **53** 4697-4718 2009.

Artignnan X., Smitsmans M. H., Lebsque J. V., Jaffray D. A., van Her M., Bartelink H. “Online Ultrasound Image Guidance for Radiotherapy of Prostate Cancer: Impact of Image Acquisition on Prostate Displacement” Int. J. Radiat. Oncol. Biol. Phys. **59** 595-601 2004.

Biggs P. J., Goitein M. and Russel M. D. “A diagnostic X ray field verification device for a 10 MV linear accelerator” Int. J. Radiat. Oncol. Biol. Phys. **11** 635-643 1985.

Booth J. T. and Zavgorodni S. F. “Set-up Error and Organ Motion Uncertainty: a Review” Aust. Phys. Eng. Sci. Med. **22** 29-47 1999.

Bortfield T. and Chen G. T. Y. “Introduction: Intrafraction Organ Motion and its Management” Sem. Radiat. Oncol. **14** 1 2004.

Bucci M. K., Bevan A. ans Roach M. “Advances in Radiation Therapy: Conventional to 3D, to IMRT, to 4D and Beyond” A. Cancer. J. Clin. **55** 117-134 2005.

Burke B., Lamey M., Rathee S., Murray B. and Fallone B.G. “Radio frequency noise from clinical linear accelerators” Phys. Med. Biol. **54** 2483-2492

2009.

Canadian Cancer Society (2004) http://www.cancer.ca/canada-wide/about%20cancer/cancer%20statistics/~/media/CCS/Canada%20wide/Files%20List/English%20files%20heading/pdf%20not%20in%20publications%20section/Canadian%20Cancer%20Statistics%20-%202004%20-%20EN%20-%20pdf_195986411.ashx

Canadian Cancer Society (2009) http://www.cancer.ca/canada-wide/about%20cancer/cancer%20statistics/~/media/CCS/Canada%20wide/Files%20List/English%20files%20heading/pdf%20not%20in%20publications%20section/Stats%202009E%20Cdn%20Cancer.ashx

Chen L., Price R. A., Wang L., Li J., Qin L., McNeeley S. et al. "MRI-based Treatment Planning for Radiotherapy: Dosimetric Verification for Prostate IMRT" Int. J. Radiat. Oncol. Biol. Phys. **60** 636-647 2004.

Dawson L. A. Sharpe M. B. "Image-Guided Radiotherapy: Rationale, Benefits and Limitations" Lancet Oncol. **7** 848-858 2006.

Daswon L. A. and Jaffray D. A. "Advances in Image-Guided Radiation Therapy" J. Clin. Oncol. **25** 938-946 2007.

Dempsey J. F. "An Image-Guided Device Providing 4D CINE MRI Simultaneous to Radiotherapy Delivery" J. Radiother. Prac. **5** 179 2006.

Eisbruch A., Dawson L. A., Kim H. M. et al. "Conformal and Intensity Modulated Irradiation of Head and Neck Cancer: the Potential for Improved Target Irradiation, Salvary Gland Function and Quality of Life" Acta. Otorhinolaryngol Belg. **53** 271-275 1999.

Fallone B.G., Murray B., Rathee S., Stanescu T., Steciw S., Vidokovic S., Blosser E. and Tymofichuk D. “First MR images obtained during megavoltage photon irradiation from a prototype linac-MR system” *Med. Phys.* **36** 2084-2088 2009.

Feldkamp L.A., Davis L. C. and Kress J. W. “Practical cone-beam algorithm” J. Opt. Soc. A. **A6** 612-619 1984.

Ghilezan M., Yan D., Liand J. et al. “Online Image-Guided Intensity-modulated Radiotherapy for Prostate Cancer: How Much Improvement can we Expect? A Theoretical Assessment of Clinical Benefits and Potential Dose Escalation by Improving Precision and Accuracy of Radiation Delivery” Int. J. Radiat. Oncol. Biol. Phys. **60** 1602-1610 2004.

Godfrey D. J., Yin F. F., Oldham M. et al. “Digital Tomosynthesis with an on-Board Kilovoltage Imaging Device” Int' J' Radiat. Oncol. Biol. Phys. **65** 8-15 2006.

Hansen V. N., Evans P. M., Swindell W. “The Application of Transit Dosimetry to Precision Radiotherapy” Med. Phys. **23** 713-721 1996.

Hector C. L., Webb S. and Evans P. M. “The dosimetric Consequences of Inter-Fractional Patient Movement on Conventional and Intensity-Modulated Breast Radiotherapy Treatments” Radiother. Oncol. **54** 57-64 2000.

Herman et al. “Clinical use of Electronic Portal Imaging: Report of AAPM Radiation Therapy Committee Task Group 58” Med. Phys. **28** 712-737 2001.

Hoisak J. D., Sixel K. E., Tirona R., Cheung P. C., and Pignol J. P. “Correlation of lung tumour motion with external surrogate indicators of respiration" Int. J. Radiat. Oncol. Biol. Phys. **60** 1298-1306 2004.

Holupka E. J., Kaplan I. D., Burdette E. C. et al. "Ultrasound Image Fusion for External Beam Radiotherapy for Prostate Cancer" Int. J. Radiat. Oncol. Biol. Phys. **35** 975-984 1996.

ICRU50 "Prescribing, Recording and Reporting Photon Beam Therapy" ICRU Bethesda. MD, 1993.

ICRU62 "Prescribing, Recording and Reporting Photon Beam Therapy (supplement to ICRU report 50)" ICRU Bethesda. MD, 1999.

Jaffray D. A., Siewerdsen J. H., Wong J. W. and Martinez A. A. "A Flat Panel Cone-Beam Computed Tomography for Image Guided Radiation Therapy" Int. J. Radiat. Oncol. Biol. Phys. **53** 1337-1349 2002.

Kirkby C., Stanescu T., Rathee S., Carlone M., Murray B. and Fallone B. G. "Patient dosimetry for hybrid MRI-radiotherapy systems" Med. Phys. **35** 1019-1027 2008.

Lagendijk J. J. W. et al. *MRI/Linac Integration* Radiother. Oncol. **86** 25-29 2008.

Langden K. M. and Jones D. T. "Organ motion and its Management" Int. J. Radiat. Oncol. Biol. Phys. **50** 265-278 2001.

Langen K. M., Pouliot J., Anezinos C. et al. "Evaluation of Ultrasound-Based Prostate Localization for Image-Guided Radiotherapy" Int. J. Radiat. Oncol. Biol. Phys. **57** 635-644 2003.

Langen K. M., Meeks S. L., Poole D. O. et al. "The use of Megavoltage CT (MVCT) Images for Dose Recomputations" Phys. Med. Biol. **50** 4259-4276

2005.

Lattanzi J., McNeeley S., Pinover W. et al. “A comparison of Daily CT Localization to a Daily Ultrasound-Based System in Prostate Cancer” Int. J. Radiat. Oncol. Biol. Phys. **43** 719-725 1999.

Leksell L. “The Sterotaxic Method and Radiosurgery of the Brain” Acta. Chir. Scand. **102** 316-319 1951.

Litzenburg D. W., Willoughby T. R., Blater J. M. et al. “Positional Stability of Electromagnetic Transponders used for Prostate Localization and Continuous Real-Time Tracking” Int. J. Radiat. Oncol. Biol. Phys. **68** 1199-1206 2007.

Mackie T. R., Holmes T., Swerdloff et al. “Tomotherapy: A New Concept for the Delivery of Dynamic Conformal Radiotherapy” Med. Phys. **20** 1709-1719 1993.

Mackie T. R., Balog J., Ruchala K., Shepard D. M., Aldridge K. S., Fitchard E. E. et al. “Tomotherapy” Semin Radiat. Oncol. **9** 108-117 1999.

Mackie T.R., Kapatoes J., Ruchala K., Lu W., Wu C., Olivera G. et al. “Image Guidance for Precise Conformal Radiotherapy” Int. J. Radiat. Oncol. Biol. Phys. **56** 89-105 2003.

Mageras G. S. “Introduction: Management of Target Localization Uncertainties in External-Beam Therapy” Semin. Radiat. Oncol. **15** 133-135 2005.

Mah D., Steckner M., Palacio E., Mitra R., Richardson T. and Hanks G. E. “Characteristics and Quality Assurance of a Dedicated Open 0.23 T MRI for Radiation Therapy Simulation” Med. Phys. **29** 2541-2547 2002.

McBain C. A., Henry A. M., Sykes J. et al. “x-ray Volumetric Imaging in Image-Guided Radiotherapy: the new Standard in on Treatment Imaging” Int. J. Radiat. Oncol. Biol. Phys. **64** 625-634 2006.

Meeks S. L., Tome W. A., Willoughby T. R., Kupelian P. A., Wagner T. H., Bautti J. M. et al. “Optically guided Patient Positioning Techniques” Semin. Radiat. Oncol. **15** 192-201 2005.

Meyer J. L., Verhey L., Xia P. and Wong J. “New Technologies in the Radiotherapy Clinic” pages 1-17 from “IMRT-IGRT-SBRT Advances in the Treatment Planning and Delivery of Radiotherapy” Front. Radiat. Ther. Oncol. **40** 2007.

Podgorsak E. B., pike G. B., Oliver A., Pla M. and Souhami L. “Radiosurgery with high Energy Photon Beams: a Comparison among Techniques” Int’ J’ Radiat. Oncol. Biol. Phys. **16** 857-865 1989.

Pollack A., Zagars G. K., Starkschall G. et al. “Prostate Cancer Radiation Dose Response: Results of the MD Anderson Phase III Randomized Trial” Int. J. Radiat. Oncol. Biol. Phys. **53** 1097-1105 2002.

Raaijmakers A. J. E., Raaymakers B. W. and Lagendijk J. J. W. “Magnetic-Field-Induced Dose Effects in MR-Guided Radiotherapy Systems: Dependence on the Magnetic Field Strength” Phys. Med. Biol. **53** 909-923 2008.

Raaijmakers A. J. E. et al. “Dose Optimization for the MRI-Accelerator: IMRT in the Presence of a Magnetic Field” Phys. Med. Biol. **52** 7045-7054 2007a.

Raaijmakers A. J. E. “Integrating a MRI Scanner with a 6MV Radiotherapy Accelerator: Impact of the surface Orientation on the Entrance and Exit

Dose due to the Transverse Magnetic Field” Phys. Med. Biol. **52** 929-939 2007b.

Raaijmakers A. J. E., Raaymakers B. W. and Lagendijk J. J. W. “Experimental Verification of Magnetic Field Dose Effects for the MRI-Accelerator” Phys. Med. Biol. **52** 4283-4291 2007c.

Raaijmakers A. J. E., Raaymakers B. W. and Lagendijk J. J. W. “Integrating a MRI Scanner with a 6 MV Radiotherapy Accelerator: Dose Increase at Tissue-Air Interfaces in a Lateral Magnetic Field due to Returning Electrons” Phys. Med. Biol. **50** 1363-1376 2005.

Raaymakers B. W. et al. “Integrating a MRI Scanner with a 6 MV Radiotherapy Accelerator: Dose Deposition in a Transverse Magnetic Field” Phys. Med. Biol. **49** 4109-4118 2004.

Rietzel E., Rosenthal S. J., Gierga D. P., Willet C. G. and Chen G. T. “Moving Targets: Detection and Tracking of Internal Organ Motion for Treatment Planning and Patient Set-up” Radiother. Oncol. **73** S68-S72 2004.

Schewe J. E., Lam K. L., Balter J. M. and Ten Haken R. K. “A room-based diagnostic imaging system for measurement of patient setup” Med. Phys. **24** 2385-2387 1998.

Seiler P. G., Blattman H., Kirsch S. et al. “A Novel Tracking Technique for the Continuous Precise Measurement of Tumour Positions in Conformal Radiotherapy” Phys. Med. Biol. **45** N103-N110 2000.

Sharpe M. B., Craig T. and Moseley D. J. “Image Guidance: Treatment Target Localization Systems” pp72-93, 2007, From “IMRT-IGRT-SBRT Advances in the Treatment Planning and Delivery of Radiotherapy" Front. Radiat. Ther. Oncol. **40** 2007.

Shirato H., Shimizu S., Kitamura M., Nishioka T., Kagei K., Hashimoto S., Aoyama H., Kunieda T., Shinohara N., Dosaka-Akita H., Miyasaka K. "Four-dimensional treatment planning and fluoroscopic real-time tumour tracking radiotherapy for moving tumour" Int. J. Radiat. Oncol. Biol. Phys. **48** 435-442 2000.

Song W., Schaly B., Bauman B., Battista J. and Van Dyk J. "Image-Guided Adaptive Radiation Therapy (IGART): Radiobiological and Dose Escalation Considerations for Localized Carcinoma of the Prostate" Med. Phys. **32** 2193-2203 2005.

van Zijtveld M., Dirkx M. L., de Boer H. C., et al. "Dosimetric Pretreatment Verification of IMRT Using an EPID; Clinical Experience" Radiother. Oncol. **81** 168-175 2006.

Verellen D., De Ridder M., Linthout N., Tournel K., Soete G. and Storme G. "Innovations in Image-Guided Radiotherapy" Nature Rev. Cancer **7** 949-960 2007.

Verellen D., De Ridder M. and Storme G. "A (short) History of Image-Guided Radiotherapy" Radio. Oncol. **86** 4-13 2008.

Viewray Inc. http://www.viewray.com/index.php (Visited Feb. 12th 2008)

Webb S. "The Physical Basis of IMRT and Inverse Planning" Br. J. Radiol. **76** 678-689 2003.

Welsh J. S., Bradley K., Ruchala K. J. et al. "Megavoltage Computed

Tomography Imaging: a Potential Tool to Guide and Improve the Delivery of Thoracic Radiation Therapy” Clin. Lung Cancer **5** 303-306 2004.

Wu A. “Physics and Dosimetry of the Gamma Knife” Neurosurg. Clin. N. Am. **3** 35-50 1992.

Yin F. F. et al. “Image-guided procedures for intensity-modulated spinal radiosurgery” J. Neurosur. Suppl. 3 **101** 419-424 2004.

Chapter 2: Investigation of the Room Effects on an RF Source

2.1 Introduction

A linac, specifically the modulator of a linac, is a source of RF noise [Burke et al. 2009]. The RF noise emitted within a room from a source reflects off various surfaces and structures. The measured RF noise at particular points away from the source is a result of constructive/destructive interferences. In this chapter, the effect of an enclosed room on the strength of RF noise at particular points within the room is investigated.

The software environment of Microstripes (Computer Simulation Technology, Darmstadt, Germany) was used to simulate the electric (E) and magnetic (H) fields from an elementary dipole antenna within a room. Simultaneous to the development of the simulation, a fellow student developed a measurement technique using constructed in-house transmit antennas and E and H near field probes from a commercially available near field probe set [Burke thesis 2008]. Measurements were conducted both within our laboratory and outdoors in a large field to simulate “free space” conditions. The purpose of the project was to determine the effect of an enclosed environment on an RF source, when comparing the fields to those from a “free” source, and to provide an experimental framework to validate our modeling.

The model included the effects of a measurement room. The permittivity of drywall and drop ceiling, of the room that was being simulated, were measured using an open-ended coaxial-sensor measurement technique [Grant et al. 1989].

Samples from the room which was simulated were used and the results from the measurements were input into the simulation.

2.2 Theory

The theory of the use of antennas is given in Appendix A.

2.2.1 Transmission Line Matrix (TLM) Theory

2.2.1.1 Introduction

The Microstripes simulation is based on a technique known as the transmission line matrix method (TLM). The technique is used to solve general electromagnetic problems, and was introduced in the early 1970's by P.B. Johns [Johns et al. 1971] and his co-workers.

The technique has been applied in both the time and frequency domains. A solution in the time domain allows one to solve for the broadband characteristics of the problem.

2.2.1.2 Basis of the TLM Method

The TLM method is based on the application of the discretization of Huygens' Principle. Huygens' Principle states that [Jordan et al. 1968] a wave front consists of a number of radiators that give rise to spherical wavelets. The envelope of these wavelets forms a new wave front, which gives rise to new spherical wavelets and so on.

Computer models require that Huygens' principle be discretized in both space and time. These quantities are related by the speed of light:

$$\Delta l = \Delta t / c. \tag{2.1}$$

Two Dimensional space can be modeled by a Cartesian grid separated by the length Δl, as illustrated in Figure 2.1, as a function of time increment Δt.

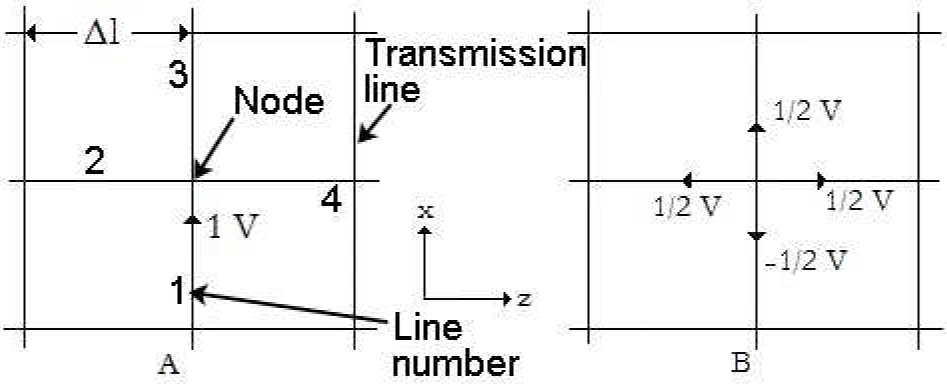

Figure 2.1: Cartesian grid of transmission lines. (A) A 1 Volt pulse incident upon a node. (B) Scattering of the voltage pulse at the node. The transmission lines are represented by the lines in the Figure.

Consider a delta impulse incident on a node, as per Figure 2.1 (A); the scattering of this pulse is governed by Huygens' Principle. The pulse is scattered (re-radiated) equally along each transmission line connected to the node. Each re-radiated pulse carries away 1/4 of the initial incident pulse energy. Since the energy is related to the square of the field quantities this means that the corresponding field quantity amplitudes are 1/2 in magnitude. We note that in order to maintain field continuity at the node, the reflection coefficient of the pulse reflected back toward the initial pulse must be negative. These three transmitted pulses and single reflected pulse, of 1/2 field amplitude, impinge upon the four adjacent nodes. Therefore, over a large mesh an initial input pulse is propagated throughout 2-D.

The TLM technique involves solving for the voltages and currents along the transmission lines. The electric and magnetic fields are then directly related to either the voltage or current (this relation is shown in Appendix B, section B.2).

2.2.1.3 Two Dimensional TLM Method

Consider the 2-D grid as shown in Figure 2.1. The reflected field amplitudes are determined using the reflection coefficient, Γ, which is defined as:

$$\Gamma = \frac{Z_{in} - Z_0}{Z_{in} + Z_0}, \tag{2.2}$$

where Z_{in} is the input impedance "seen" by the original pulse and Z_0 is the impedance of the line used to carry the pulse. Approaching a node, the pulse "sees" three lines in parallel, if the impedances of each line is normalized to 1, then the input impedance seen by the pulse is 1/3 (three parallel lines of impedance 1). This also assumes that locally we are in a homogeneous medium where each transmission line has the same impedance.

We then have:

$$\Gamma = \frac{1/3-1}{1/3+1} = -\frac{1}{2}, \tag{2.3}$$

the transmission coefficient, T, for each of the outgoing lines in parallel is:

$$T = 1 + \Gamma = \frac{1}{2}. \tag{2.4}$$

Therefore, a unit voltage pulse incident on a node will produce four re-radiated pulses which include; three transmitted pulses of amplitude 1/2 and one reflected pulse of amplitude -1/2. I.e. we now have a spherical wave of amplitude 1/2 traveling away from the node. The division of space into a fine grid of transmission lines produces propagation as described by Huygens. Each pulse emerging from one node is incident on the adjacent node and produces a spherical wave which travels away from a given node, this is Huygens principle.

The general case, which involves four impulses incident upon a node, can be determined by superposition of the above case. If at time $t = k\Delta t$ we have pulses incident i (designated as superscripts) of amplitude V, on a node given by; ${}_kV_1^i$, ${}_kV_2^i$, ${}_kV_3^i$, ${}_kV_4^i$ (where the subscripts on the right denote the line number (see Figure 2.1) into the node). Then the total reflected r (also designated as superscripts), pulse voltage along line n, n will take the value of 1, 2, 3 or 4 in 2D, at the time ${}_{k+1}\Delta t$ is (the propagation of a pulse from one node to the next is one time step):

$$ {}_{k+1}V_n^r = \frac{1}{2}\left(\sum_{m=1}^{4} {}_kV_m^i\right) - {}_kV_n^i, \tag{2.5}$$

where in 2D, for each of the individual four lines n into an arbitrary node, we sum over the four lines m into the node. The second term arises since the pulse incident along line n is reflected with inverted amplitude. As an example suppose the four incident amplitudes along lines 1, 2, 3 and 4 into a node were 1, 2, 3 and 4 respectively, then the reflected pulse along line 1 using Equation 2.5 would be: ${}_{k+1}V_1^r = \frac{1}{2}(1+2+3+4)-1 = 4$.

Equation 2.5 can be written in the form of a scattering matrix as:

$$ {}_{k+1}\begin{pmatrix} V_1 \\ V_2 \\ V_3 \\ V_4 \end{pmatrix}^r = \frac{1}{2}\begin{pmatrix} -1 & 1 & 1 & 1 \\ 1 & -1 & 1 & 1 \\ 1 & 1 & -1 & 1 \\ 1 & 1 & 1 & -1 \end{pmatrix} \cdot {}_k\begin{pmatrix} V_1 \\ V_2 \\ V_3 \\ V_4 \end{pmatrix}^i . \tag{2.6}$$

From the knowledge of how an incident pulse propagates away from a node, after reflection and transmission, and the fact that a pulse reflecting from a node at position (z, x) must become an incident pulse on the neighboring node we have:

$$\begin{aligned}
{}_{k+1}V_1^i(z,x) &= {}_{k+1}V_3^r(z,x-1)\\
{}_{k+1}V_2^i(z,x) &= {}_{k+1}V_4^r(z-1,x)\\
{}_{k+1}V_3^i(z,x) &= {}_{k+1}V_1^r(z,x+1)\\
{}_{k+1}V_4^i(z,x) &= {}_{k+1}V_2^r(z+1,x)
\end{aligned}. \qquad (2.7)$$

Equations 2.5 and 2.7 can be used in tandem, by operating on each node, to determine the magnitudes, positions and directions of all impulses at time *(k+1)Δt*, once the values for these variables are known at the *kΔt* time step.

The impulse response of the network is determined by applying successive operations on each node for each time step. The scattering process is illustrated in Figure 2.2. In Figure 2.2 an initial pulse along with the first two iterations are shown. Figures 2.2 (b) and (c) illustrate the spread of the initial pulse shown in (a) across a 2-dimensional network.

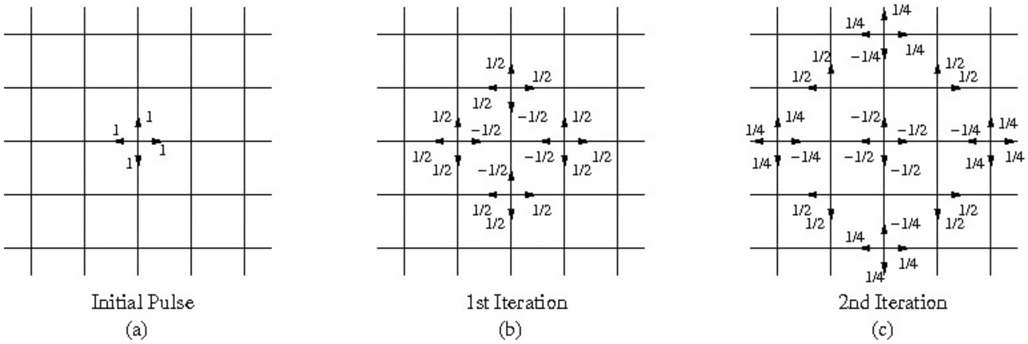

Figure 2.2: First two iterations after a Dirac input pulse is used to excite the system. (a) Initial pulse (b) 1st iteration (c) 2nd iteration.

A detailed discussion on the TLM method is included as Appendix B. In this appendix we discuss the relationship of the voltages and currents along the lines to the electric and magnetic field values, the three dimensional node and the errors involved in the TLM method.

2.2.2 Equivalent Circuit Open Ended Coaxial Sensor Theory

The following theory is the basis of a technique that is used for measuring the permittivity of samples. The equivalent circuit method is a subset of the open ended coaxial sensor theory, and is a technique used to estimate the complex permittivity of a sample. It is based on a model of the discontinuity at the termination of a coaxial line and was introduced by Stuchy et al. [Stuchy et al. 1974 and Rzepecks et al. 1975]. The model is shown below in Figure 2.3; it consists of a two capacitive paths between the inner and outer conductors of the coaxial cable: a capacitance through the coaxial line dielectric (C_L) and a capacitance through the sample at the end of the line (C_s) [Athey et al. 1982].

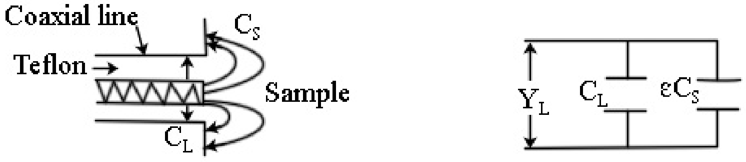

(A) (B)

Figure 2.3: Equivalent circuit model of a discontinuity at the end of a coaxial cable line. Two capacitances exist, one between the coaxial line conductors (C_L) and a second arising due to fringing fields within the sample (C_S).

For a line of impedance Z_0 terminated with an impedance Z, the complex reflection coefficient Γ is:

$$\Gamma = \frac{Z - Z_0}{Z + Z_0}. \qquad (2.8)$$

We can rearrange the equation to solve for the termination impedance Z:

$$Z = \frac{Z_0(1+\Gamma)}{(1-\Gamma)}. \qquad (2.9)$$

In terms of the admittance, *Y*, Equation (2.9) is given by Equation (2.10).

$$Y = \frac{Y_0(1-\Gamma)}{(1+\Gamma)} \qquad (2.10)$$

According to the equivalent circuit model the admittance of the sample is (i.e. Figure 2.3B):

$$Y = j\omega C_L + j\omega(\varepsilon' + j\varepsilon'')C_S, \qquad (2.11)$$

where ω is the angular frequency and the complex permittivity ε is defined as:

$$\varepsilon = \varepsilon' + j\varepsilon''. \qquad (2.12)$$

The real part describes the ability to store energy by polarization and the imaginary part describes any energy loss. Equations (2.10) and (2.11) can be used to eliminate the admittance *Y* and solve for the real and imaginary components of the complex permittivity. Equating the real and imaginary components yields:

$$\varepsilon' = \frac{-2Y_0|\Gamma|\sin\varphi}{\omega C_S(1+2|\Gamma|\cos\varphi + \Gamma^2)} - \frac{C_L}{C_S} \qquad (2.13)$$

and

$$\varepsilon'' = \frac{Y_0(1-\Gamma^2)}{\omega C_S(1+2|\Gamma|\cos\varphi + \Gamma^2)}, \qquad (2.14)$$

where $|\Gamma|$ and φ are the magnitude and phase of the reflection coefficient. Equations (2.13) and (2.14) can be used to estimate the real and imaginary components of the complex permittivity. Measurements of the reflection coefficient, line admittance, and the capacitances C_L and C_s are required. The system is calibrated using samples for which C_S is known and the reflection coefficient and line impedance is measured using a network analyzer. We determine ε', by rearranging Equation 2.13 to obtain an intercept C_t and a slope C_S (with abscissa-variable ε'). The known samples are used to generate a linear graph at each measurement frequency. Then the reflection coefficient of the unknown sample is measured and the result is cross referenced to the calibration curve at each frequency to determine the sample permittivity (Equation 2.14 is similarly linearized to determine ε''). This method of determining the complex permittivity is valid with the assumptions that the capacitances, C_L and C_S, are independent of the sample complex permittivity and that the probe (the end of the coaxial line in Figure 2.3A) does not act as an antenna.

2.2.3 Model of a Dipole Antenna above Earth

We must consider ground reflections when modelling a transmit antenna above the earth. The earth itself acts as an imperfect ground plane forming an image of the transmit antenna [Stutzman 1981 and Jordan et al. 1968]. At a particular point away from a transmit antenna there will exist reflections from the surface of the earth. To the receive point itself, these reflected waves act as if they come from an antenna located at the same height below ground as the transmit antenna is above ground. This is the location of the image antenna. In the very high frequency (VHF: 30-300 MHz) range and below, the operation of antennas are affected significantly by its environmental surroundings [Stutzman 1981]. For the presented work, investigations were performed at 400 and 500 MHz in order to perform our measurements in the far field. These frequencies were chosen to reduce complications associated with near field measurements. For example reactive power can circulate between the reactive near field and the source [Balanis 2005]. See Appendix A for a discussion on antenna field regions. The larger frequencies also enabled the reduction of the size of the antennas. These frequencies are near the VHF range and so ground reflections were considered important. As will be shown below, the inclusion of earth ground reflections was an important part of the simulation.

Consider the arrangement shown in Figure 2.4.

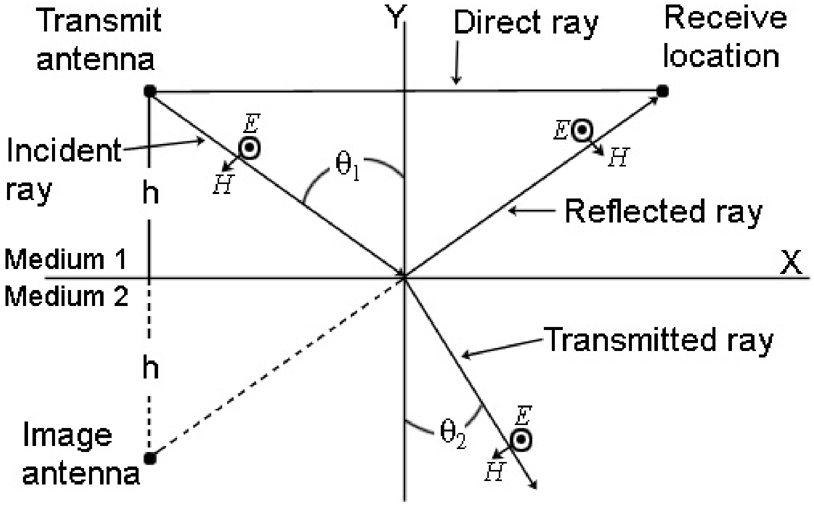

Figure 2.4: Arrangement of transmit and receive points above ground illustrating the effect of a ground wave. In this work medium 1 is air and medium 2 is ground.

For the case of horizontal polarization (E field horizontal with respect to the surface, i.e. into page in Figure 2.4), we apply the boundary condition which states that the tangential component of the E field must be continuous [Jackson

1999], that is:

$$E_i + E_r = E_t \, , \tag{2.15}$$

where the subscripts i, r and t denote the incident, reflected and transmitted waves respectively. Similarly for the magnetic field we require:

$$H_i \cos\theta_1 - H_r \cos\theta_1 = H_t \cos\theta_2 \, . \tag{2.16}$$

The negative sign results from the incident and transmitted H field being along the –x direction (see Figure 2.4). Using the relation $H = E/\eta$, Equation 2.16 can be re-written:

$$\frac{E_i}{\eta_1}\cos\theta_1 - \frac{E_r}{\eta_1}\cos\theta_1 = \frac{E_t}{\eta_2}\cos\theta_2 \, , \tag{2.17}$$

where η is the wave impedance, $\eta = \sqrt{\mu/\varepsilon}$ (μ is the permeability and ε is the permittivity, the relation holds for a material of negligible conductivity), and the subscript represents materials 1 (air) and 2 (ground) in Figure 2.4. Insertion of Equation (2.17) into (2.15) with the use of Snell's law ($\sin\theta_1 / \sin\theta_2 = \sqrt{\varepsilon_2/\varepsilon_1}$ and $\sqrt{\varepsilon_2/\varepsilon_1}\cos\theta_2 = \sqrt{\varepsilon_2/\varepsilon_1 - \sin^2\theta_1}$) and the fact that for dielectrics the permeability is approximately that of air (i.e. $\mu_1 \sim \mu_2$) [Jordan et al. 1968] yields:

$$\frac{E_r}{E_i} = \frac{\cos\theta_1 - \sqrt{\varepsilon_r - \sin^2\theta_1}}{\cos\theta_1 + \sqrt{\varepsilon_r - \sin^2\theta_1}} \, , \tag{2.18}$$

where ε_r is the relative permittivity of material two to material one. For the general case of a medium with conductivity, σ, the permittivity can be replaced by ε' where:

$$\varepsilon' = \varepsilon\left(1 + \frac{\sigma}{j\omega\varepsilon}\right) . \tag{2.19}$$

In this case Equation (2.18) can be written as:

$$\frac{E_r}{E_i} = \frac{\cos\theta_1 - \sqrt{\varepsilon_r' - \sin^2\theta_1}}{\cos\theta_1 + \sqrt{\varepsilon_r' - \sin^2\theta_1}}. \tag{2.20}$$

A horizontal dipole antenna above ground was modeled using Equation (2.20). Equation (2.20) provides the "image antenna" strength, at a height below ground, which is the same as the height of the antenna above ground. In MicroStripes this can be modeled by assigning an amplitude factor for a second antenna below ground.

The conductivity of earths ground, in Edmonton, was estimated using values presented by Clement [Clement 1961]. Clement provides a range of values between 14×10^{-3} and 28×10^{-3} mho/m for the conductivity of earth's ground. We used the midrange value of 20×10^{-3} mho/m in our analysis. Jordan [Jordan et al. 1968] also states that the relative permittivity of earth ranges from 7 to 30. We used the midrange value of 15 in this work. The range of values of θ_1 for our experimental setup was determined to be 5.7° to 33.7°; substitution of these values into Equation (2.20) at 500 MHz yields the plot shown in Figure 2.5.

Because the reflection amplitude (E_r/E_i) from Equation (2.20) contains real and imaginary components, there is a phase difference between direct and reflected rays. The phase difference was also determined using Equations 2.19 and 2.20, using the above estimated values for the conductivity and relative permittivity of earth, a plot of the phase shift as a function of incident angle is shown in Figure 2.6.

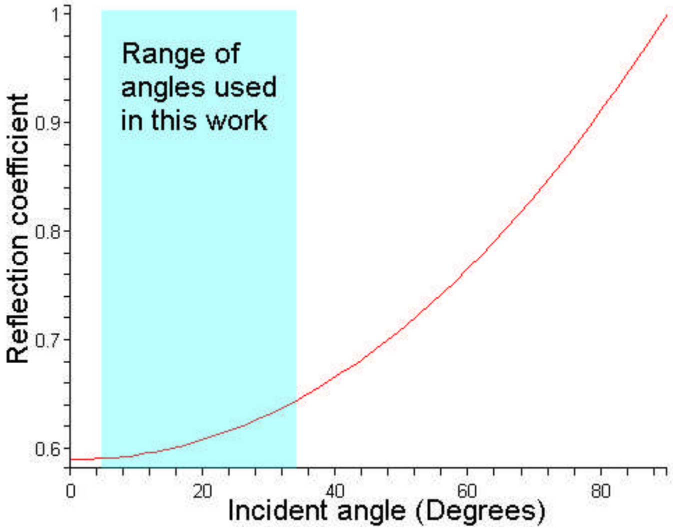

Figure 2.5: Plot of the reflection coefficient as a function of incident angle for a horizontal dipole above earth at 500 MHz.

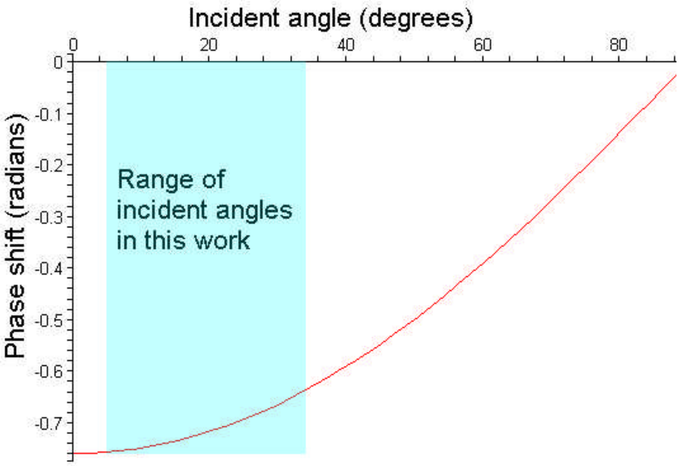

Figure 2.6: Phase shift of a reflected wave from a dipole antenna above ground at 500 MHz.

Only one value of the amplitude and phase shift could be implemented per simulation. The values shown for the amplitude and phase in Figures 2.5 and 2.6, respectively were the values used for 500 MHz. Different values of amplitude and phase were used for different frequencies. Due to the long simulation lengths, approximately 30 hours, it was unrealistic to simulate each angle for every measurement point (the simulated and measured data was taken as a function of distance from a dipole antenna source). An average of the values shown in the shaded region of Figures 2.5 and 2.6 was implemented at two frequencies; 400 and 500 MHz (the plots at 400 MHz are not shown, but are very similar). In order to gain an accurate representation of a reflecting ground, a large amount of equivalent earth material would have been required; this was an unrealistic addition to the simulation. The effects of a reflecting earth ground on a horizontal dipole antenna were approximated by inserting an image antenna with the above determined amplitude and phase relationship to the "real" dipole antenna.

2.2.4 Perfectly Matched Layer Boundary Condition

An important aspect of the simulation was the choice of the boundary conditions. Beyond the room walls a limited volume of free space could be modeled. As we increased the modeled free space, the number of nodes in the simulation also increased, therefore leading to large increases in the simulation times and problems with computer memory limitations. The perfectly matched layer (PML) was the boundary condition used in this model. A PML is a sheet of material which is thick, with respect to wavelength of the measured signal, and possesses unusual electromagnetic properties. These properties result in a perfectly reflectionless surface, i.e. the reflection coefficient is zero for any angle of incidence. Within the layer the wave is exponentially attenuated. Free space was thus modeled as a thin sheet of material using a PML. It was clearly not the case that free space existed outside the measurement room; however, it was unrealistic to model adjacent rooms because of the limitations on computer memory and simulation time. The boundary conditions were necessary to keep the simulation size reasonable. In order to accurately simulate the fields from the dipole, a minimum node separation of λ/10 was used as recommended by the software vendor [Microstrpies Reference Manual 2006], where λ is the wavelength.

The original concept of a PML for free space simulation was introduced by Berenger [Berenger 1994]. Today a slightly different formalism is used and Sacks [Sacks et al 1995] provides an outline of the complete derivation. The formulation used in this work followed that provided by Sacks.

2.2.5 Modeling Objectives

For a real time linac-MRI system, the linac will be a source of RF noise. The fields from the linac will be affected by the enclosed environment. The purpose of the simulations was to determine the magnitude of the effect that the enclosed environment had on the RF fields from the linac. The MRI will be near the linac; these RF emissions could be picked up by the RF coils used to generate an MR image. This RF noise would then produce image artefacts. The simulations were also used to validate measurements performed in the same environment.

2.3 Materials and Methods

2.3.1 MicroStripes Program

MicroStripes (Computer Simulation Technology, Darmstadt, Germany) is a software program which can be used to solve three-dimensional electromagnetic problems. MicroStripes is used to solve problems involving radiating systems or antennas [Shrivastava et al. 2008 and Singh et al. 2006]. The user defines the geometry by using an imported structure, or by using the built in geometry modeler. Next the type of excitation is set, and the user defines the outputs which he/she would like to obtain. Finally the problem is solved using the TLM technique as described in section 2.2.1 and the results can be viewed using built in visual software. An advantage of the TLM method is that a problem can be solved over a broad frequency range in one simulation run. The solution to the problem is determined in the time domain and a Fourier analysis is used to produce a broadband solution.

Figure 2.7 shows a view of the room modeled by our simulation. This is also the room in which measurements were performed. The room consists of drywall walls (light blue), a large lab-area bench (brown) with a drywall insert (aqua colour) and a concrete post (black), a file cabinet at the end of the bench, air conduits which are modeled as Aluminum (only the larger ones of which were modeled), drop ceiling (red), a door and glass panes and other equipment within the room. Although a floor is shown in Figure 2.7, as stated above no floor was used in the simulation but its effect was accurately accounted for by an image antenna, the floor is included for ease of visualization.

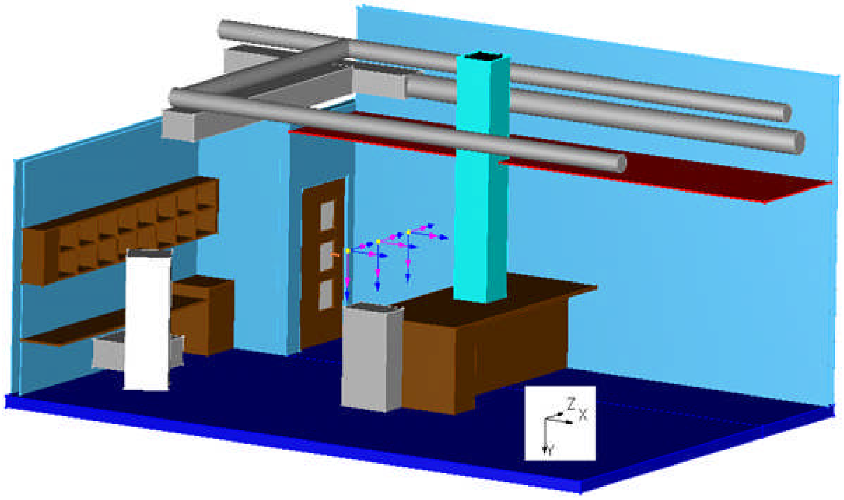

Figure 2.7: Partial view of the room simulated using MicroStripes. The three yellow points illustrate measurement points from a source. No floor was used in the model however one is shown here for clarification of the room setup. The substructures are: drywall walls (light blue), a large lab-area bench (brown) with a drywall insert (aqua colour) and a concrete post (black), a file cabinet at the end of the bench (grey), air conduits which are modeled as Aluminum (only the larger ones of which were modeled), drop ceiling (red), a door and glass panes and a other equipment within the room.

The fields from a small dipole antenna were physically measured [Burke thesis 2008], as well as simulated. The dipole antenna, in Figure 2.6, is situated about halfway between the centre table and the left wall; it is about 2 meters off the floor and is oriented along the x-axis. The dipole was also simulated in a free space environment. Material properties are specified in terms of their permittivity and conductivity. As previously mentioned the permittivities of drywall and drop ceiling were measured using the open ended equivalent circuit technique [Grant 1989], with an Agilent (Agilent Technologies, Santa Clara, California, USA) 85070A probe. The measurement technique is described below in section 2.3.2. The following material properties, and/or range of material properties, were used:

Metal conductivity: 3.5×10^7 S/m

Concrete relative permittivity: 4-10, conductivity: 0.0006 S/m

Drywall relative permittivity: 2.3, conductivity: 0 S/m

Drop Ceiling relative permittivity: 1.55, conductivity 0 S/m.

The program solved for the resulting field patterns by specifically including the effects of the surrounding environment (the laboratory). Simulations were performed for the emissions from a dipole that covered a frequency range of 2 to 500 MHz. The goal of the studies, along with the results generated in free space, was to generate a correction factor; this factor could then be applied to real physical measurements which would convert the measurements to a result that would be expected in free space (i.e. the actual source strength).

In the laboratory, the *E* and *H* fields from the dipole were measured separately using a Rohde and Schwarz (Rohde and Schwarz, Munich, Germany) HZ-11 near field probe set (the *E* and *H* field probes used are shown in Appendix A). The field probes were mounted on an RF transparent stand made of wood and Delrin® (Polyoxymethylene). The stand enabled variable positioning of a receive antenna (or probe) away from the transmit dipole antenna. Measurements of the fields from a dipole were performed as a function of distance from the dipole within the same room as simulated. The same set of measurements was subsequently performed in an open field; these measurements were an attempt to measure the fields from a dipole antenna in “free space”. The measurements are as described in the thesis by Burke [Burke thesis 2008].

2.3.2 Coaxial Sensor Setup

The system used to measure the complex permittivity of the room samples (drop ceiling and drywall) consisted of an Agilent 85070A open ended coaxial probe, an Agilent 4991A network analyzer, several samples of drywall and drop ceiling and samples with known permittivity.

The setup for the measurement is shown in Figure 2.8.

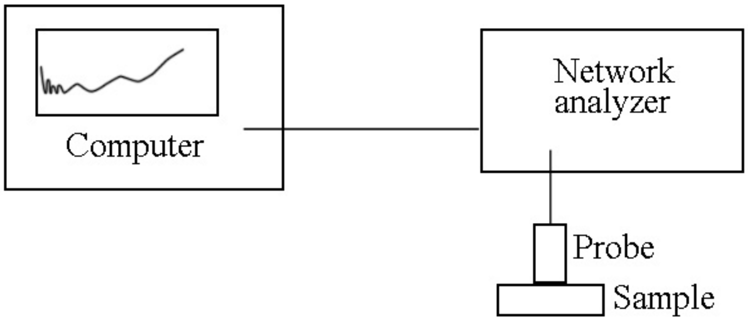

Figure 2.8: Setup used to measure the complex permittivity of the room materials.

The sensor was calibrated using a three step process involving known standards: no sample, shorted end of line and deionized water. The complex permittivity properties of these standards are well known. With nothing connected at the end of the sensor a measurement of the reflection is taken. This is done to record the effect of the cable connecting the probe to the network analyzer. Large changes in the cable positioning, including flexures in the cable, after the calibration procedure is completed can lead to inaccurate results. Secondly the end of the sensor is short circuited. The measurement data from the air standard (step 1) is used as a reference to calibrate the data from the short circuit setup. The data is then compared to the expected values to ensure proper calibration. Thirdly measurements from a deionized water sample are taken; again the data is compared to the expected values to determine if the probe has been properly calibrated.

Before the room samples (drywall and drop ceiling) were measured their surfaces were flattened and smoothed using sandpaper. This was important since it is known that samples with rough or uneven surfaces could lead to inaccurate measurement results [Aqil 2008]. After the calibration process was complete the samples were measured. As described previously (section 2.2.2) the standards determine a calibration curve which is used to determine the unknown permittivity. The data from the network analyzer was transferred to a computer using a GPIB interface and exported into an excel worksheet. No further offline analysis was required.

2.3.3 Probes, Antennas and Measurements

The receive probes used for measurements consisted of a loop and a “ball” probe from the Rohde and Schwarz near field probe set (See appendix A). The loop probe was used to measure the three orthogonal components of the H field, while the ball probe measured the total E field. An in-house constructed twelve centimetre long dipole antenna was used as a transmit antenna. A short dipole (and higher frequencies) was chosen to reduce complications arising from antenna and surrounding environment interactions. See appendix A for a discussion on the field regions of an antenna. An Agilent E4400B ESG Series signal generator was used as the RF power source for the transmit antenna. The signal from the receive probes was fed into a spectrum analyzer for measurement of the received power. A schematic of the setup is shown in Figure 2.9.

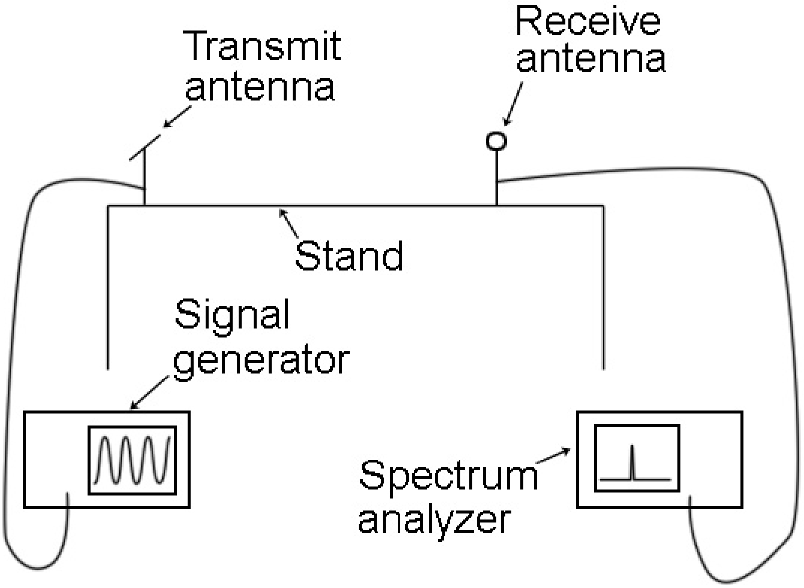

Figure 2.9: Setup used to measure the *E* and *H* fields from a transmit antenna. Measurements were taken both in a lab and in a large open field area.

2.4 Results

2.4.1 Measurements of the Complex Permittivity

The results of the real part of the measured complex permittivity for drop ceiling, drywall with no paper and drywall with paper are shown in Figure 2.10. The imaginary part of the measured complex permittivity is shown in Figure 2.11.

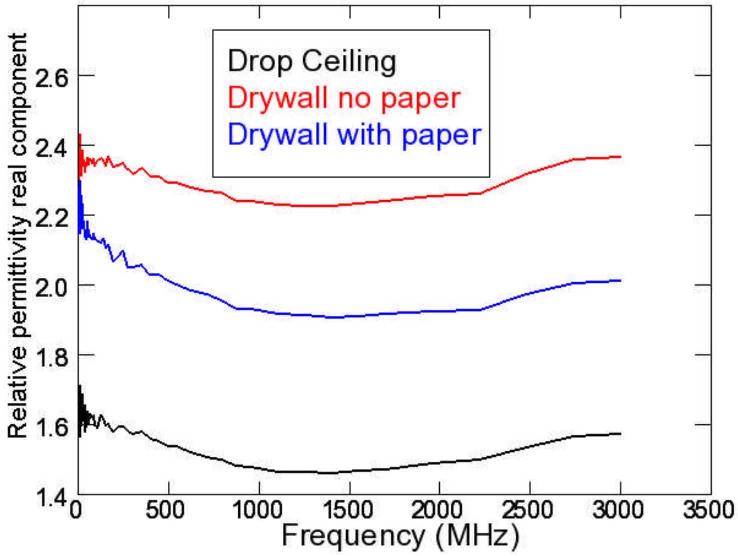

Figure 2.10: Real part of the complex permittivity of drop ceiling, drywall with paper and drywall with the paper sanded off.

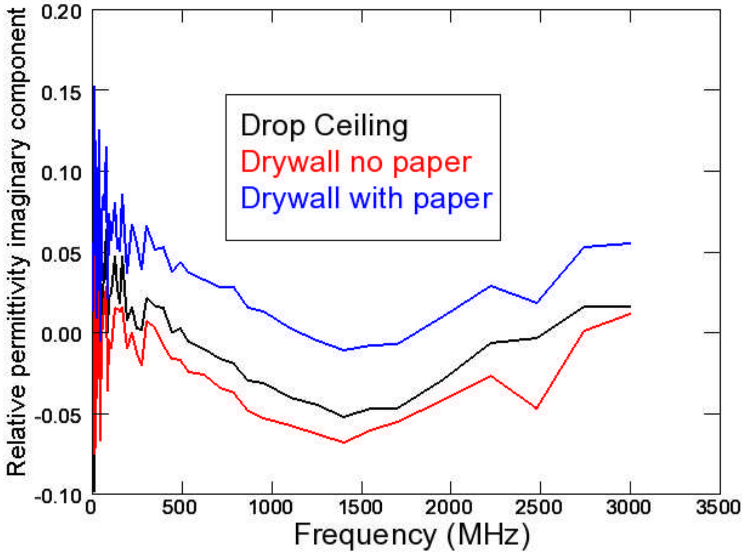

Figure 2.11: Imaginary part of the complex permittivity of drop ceiling, drywall with paper and drywall with the paper sanded off.

Because of the dryness of the sample it was expected that the imaginary part of the complex permittivity would be close to zero [Aqil 2008]. In the simulation model a constant permittivity for drywall and drop ceiling of 2.3 and 1.55 respectively was used. It should be noted that the value of the permittivity of the drywall without paper, in Figure 2.10, was greater than that of the normal drywall sample. This can be expected from the measurement process, the paper was removed to obtain a better estimate of the overall sample permittivity. The measurement process involves the determination of a reflection coefficient. The presence of paper at the surface can affect the measurements, as can be seen in Figure’s 2.10 and 2.11.

2.4.2 Results of the Room and Field Measurements

The results of the experimental measurements, taken on the wooden stand from a dipole transmit antenna, are shown in Figures 2.12 - 2.15. Each figure shows the data taken in the measurement room and then separately in an open large field. Data was taken at 400 and 500 MHz as a function of distance away from the dipole and at the same vertical height as the dipole. In the far field of a “free” dipole, we expect the field strengths to be inversely proportional to distance from the source [Balanis 2005]. In Figures 2.12 and 2.13 strong oscillations are seen in the measured *E* fields within the room at both 400 and 500 MHz. The *H* field does not show such strong oscillations.

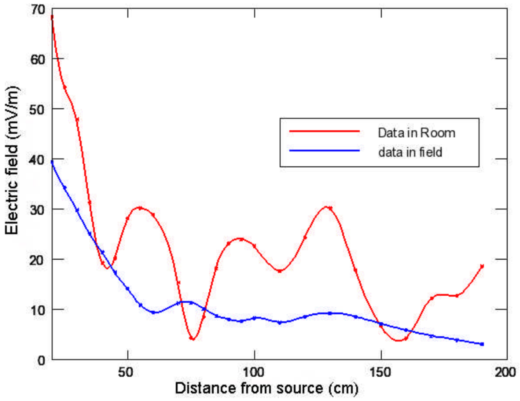

Figure 2.12 Measured Electric field as a function of distance from a dipole antenna at 400 MHz.

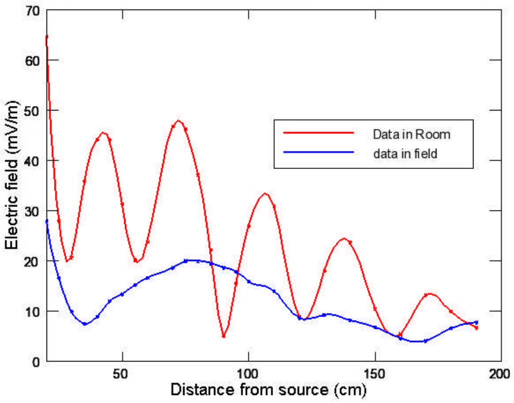

Figure 2.13 Measured Electric field as a function of distance from a dipole antenna at 500 MHz.

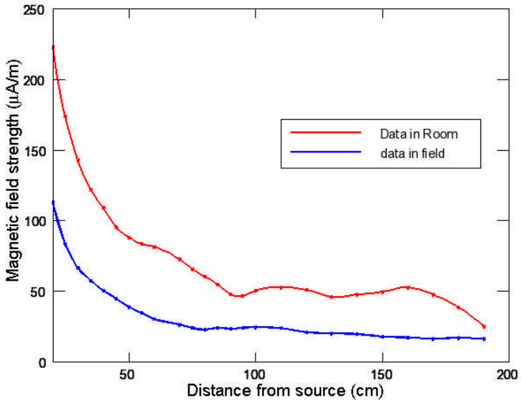

Figure 2.14 Measured Magnetic field strength as a function of distance from a dipole antenna at 400 MHz.

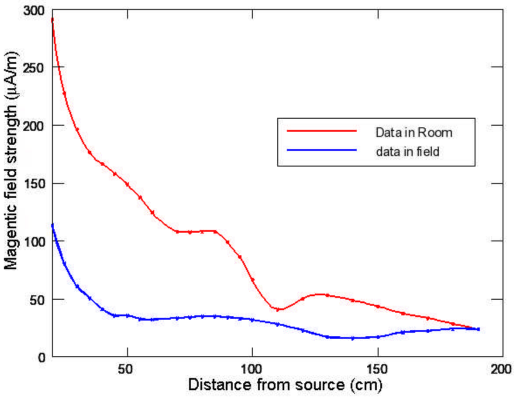

Figure 2.15 Measured magnetic field strength as a function of distance from a dipole antenna at 500 MHz.

2.4.3 Results of the Simulated Room and Free Dipole

Similarly to the measurements, the fields from a dipole were simulated at 400 and 500 MHz, both within the simulated room and in “free” space. Figures 2.16 - 2.19 show three curves: the simulation results in the measurement room, the simulation of a dipole in free space (no room) and the theoretical falloff of a dipole (the formulas given in appendix A were used). The simulations for the *E* field within the room do show oscillations, however, the occurrence of these oscillations do not reproduce the measured results very well. Similar to the case for the *H* field, fewer oscillations were observed in the simulated data. The theoretical curve was normalized to the simulated data using the knowledge of the input voltage and impedance in the simulation and inserting a determined value of I_0 into equations A.16 – A.18 of Appendix A.

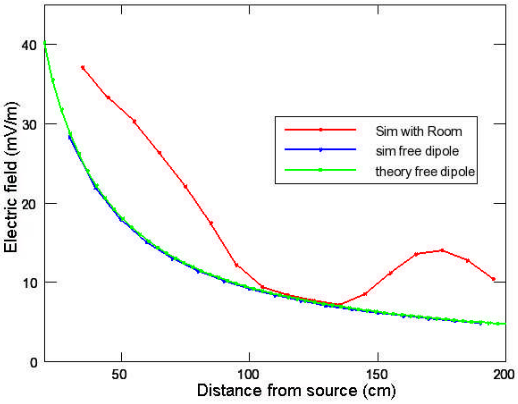

Figure 2.16 Simulated Electric field as a function of distance from a dipole antenna at 400 MHz.

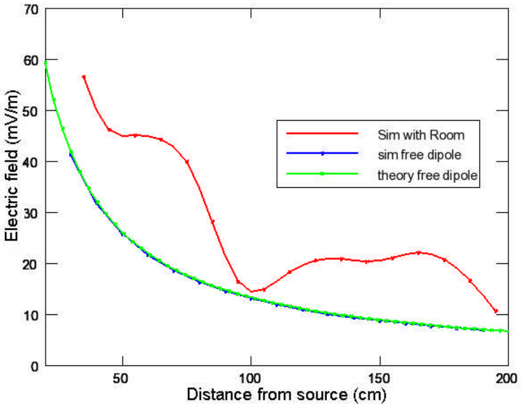

Figure 2.17 Simulated Electric field as a function of distance from a dipole antenna at 500 MHz.

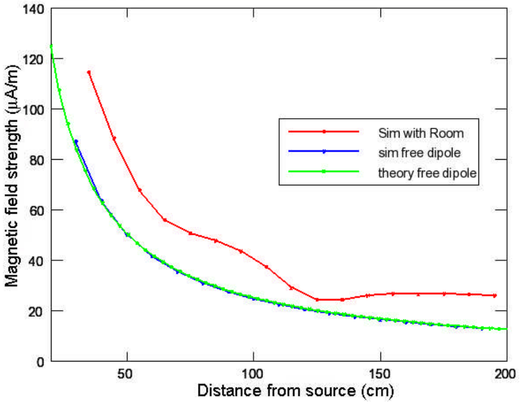

Figure 2.18 Simulated Magnetic field strength as a function of distance from a dipole antenna at 400 MHz.

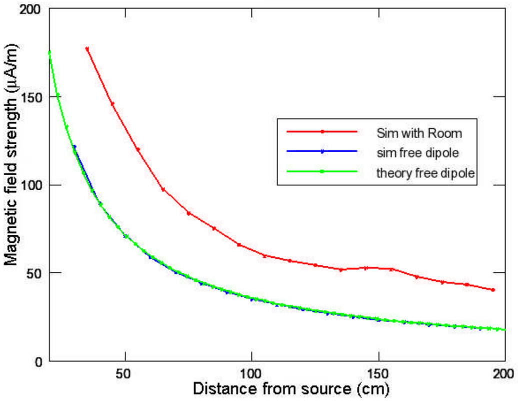

Figure 2.19 Simulated magnetic field strength as a function of distance from a dipole antenna at 500 MHz.

The simulated E field from the dipole antenna in two simulation scenarios is shown in Figure 2.20. The two scenarios were: an image antenna and a concrete floor. Figure 2.20 illustrates that very similar results were obtained using either method.

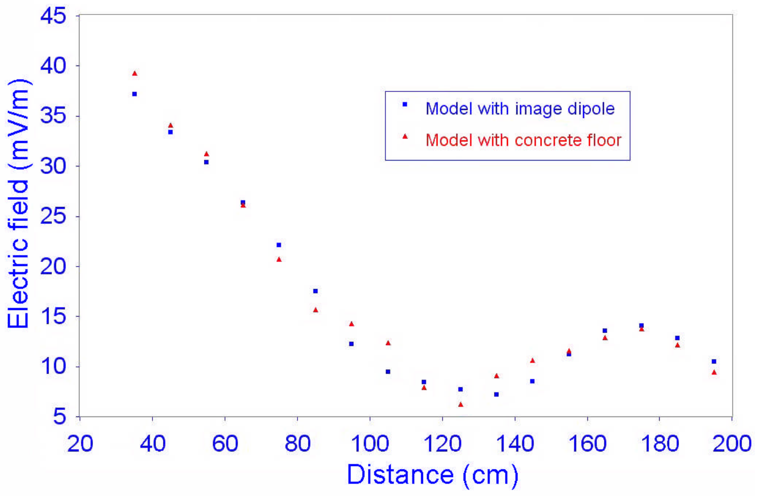

Figure 2.20 Simulated Electric fields at 400 MHz with an image antenna and a concrete floor. Very similar results were produced in the two scenarios.

2.5 Discussion

For a linac-MRI system the modulator of a linac, which is a source of RF, will be placed near the MRI component. An understanding of how an enclosed room would affect the distribution of *E* and *H* fields from an RF source was the main goal of the study. To this end, the measurement room and some of the materials within the room were modeled with our simulation. Simultaneously, while the model was being constructed an antenna measurement technique was being developed by a fellow student [Burke thesis 2008]. Measurements conducted within the room using the antenna measurement technique were performed to assess the validity of the simulation.

It can be seen from Figure 2.7 that the measurement room is not a large open area. Metallic objects along with an earth ground exist which can greatly influence the fields from the dipole. The simulation of such a room is useful for validation of the simulation process, as the proposed linac-MRI combination will have metallic objects (such as an RF cage and the linac itself). Figures 2.12 - 2.19 illustrate that the field strength can vary quite significantly from that of a free dipole. A major contributor to the difference in field strengths is that the earth below the dipole acts as a reflective plane. This plane produces a second image dipole with approximate amplitude 0.6 times the original dipole (see Figure 2.5), there is also a phase shift with respect to the original dipole (see Figure 2.6).

The simulated fields exhibit the proper falloff moving away from a free dipole when compared to theory. The simulated radiation field pattern shows interesting characteristics such as the peaks and valleys in the *E* and *H* field plots. The experimental results also show similar features such as these peaks and valleys. Overall, the simulations predicted that the measured field strength as a function of distance from the source would be increased within the room (Figures 2.16 - 2.19). This increase was about a factor of two. Our experimental results also show differences up to a factor of two as well.

Clearly the exact shape of the *E* field is not well reproduced. Our indoor measurements show many more peaks, and peaks with greater amplitude within the measurement range. There are a few possible reasons as to why our simulations did not reproduce the measurements more accurately. Our model was that of a single finite sized room. There are adjacent rooms which contain metallic equipment which could have been an important source of reflections. The material properties in the room could have been different than the ones used in the model. For example the permittivity of concrete can vary quite significantly with water content [Robert 1998] and reinforcement used. The model assumed that an image dipole existed (as a result of being above the earth) rather than a concrete floor. Details on the concrete floor thickness and the water content of the concrete were sought but could not be attained.

Although the simulations did not exactly match the measurements, both the measurements and simulations showed that compared to a free dipole source, the fields are affected by about a factor of order two. Since the measurements and simulations both suggest a factor of two between a free and non-free dipole we can expect that the fields near an RF source, placed within proximity to an MRI, will only be affected by about a factor of two from the expected 1/r falloff. This provides a “room factor” of approximately two. However this assumes that the results obtained in the frequency range of 400-500 MHz can be applied in the 1-100 MHz range; the range of clinical MRI’s. Within an enclosed environment, we can expect that the fields will not falloff as 1/r; rather they may fall between 1/r and 2/r (neglecting other physical constants). Furthermore, although not shown in this work there will exist modes within an RF cage in which the fields will be enhanced.

Studies performed after the completion of this work illustrated that within a clinical vault, the measured RF noise power density did not show dependence on distance from the linac [Burke et al. 2009]. It may be the case that the RF sources within the modulator of a linac (see chapter 4) do not act as a small dipoles. In fact, since the modulator casing is not a good RF shield, signals from inside the modulator escape and appear as many antennas. For example the seams along panels, vents etc. will all act as antennas radiating the RF power within. Thus the modulator will act as a large array of sources (approximately $2 \times 1 \times 1$ m^3) comprised of many antennas. Within a few meters of the modulator we may not see any distance effects from such a source. Furthermore, the material properties of a clinical vault are different than that of our measurement room. For instance the room walls for low energy (6 MV) vaults will be between 1.2 to 2.5 meters of concrete. The walls nearest the transmit dipole in our measurement room are made of thin sheets of drywall with 2 × 4 framing. This may also have a great effect on the distribution of the fields within the clinical vault.

From Figures 2.11 – 2.18 we can see that there is a large difference between the effects of a room on the E and H fields. Three criteria are given in Equation (A.15) to meet the near field. The third of these is that $d >> \lambda$, where d is the distance from the antenna and λ is the wavelength. At 400 and 500 MHz the wavelengths are 75 and 60 cm respectively. In the room the distance to the nearest wall was approximately 200 cm. Thus the above far-field criterion is not met. For an electric source (a source with high E/H impedance, such as a dipole) in the near field, the impedance is larger than the free space impedance. The reflection from a surface is dependent on the ratio of the wave impedance and the material impedance. Ott [Ott 1988] shows that in such a case larger reflections occur for the E field as compared to the H field. We would therefore expect more variations in the E field than the H field.

The major source of error, for the permittivity measurements of the sample in the room, for all three samples was the accuracy of the probe for the particular sample. The drop ceiling sample contains many air pockets, the existence of these air pockets can greatly affect the result. Five samples of each material were prepared and measured individually; the results shown in Figures 2.9 and 2.10 are an average of these five samples. The measured complex permittivity was shown to be reproducible. Other sources of uncertainty include the error associated with the measurement with the use of a network analyzer, and temperature drift which predominantly resides in the cables connecting the probe to the network analyzer. These errors are small when compared to the error associated with sample itself, i.e. the samples contain air pockets which can affect the measurement.

The largest error associated with the field measurement can be attributed to the performance factor used when converting between the measured signal and the field value. A systematic error of 10 % is attributed to the measured field values resulting from the performance factors. This 10 % error results from an error of 1 dB in reading the performance factor from the manufacturer’s table, see figure A.3 in the Appendix.

2.6 Conclusions

The fields from a small dipole antenna were measured and simulated both within an enclosed room and in a large open area or free space. The simulation work showed similar effects to the magnitude of the measured fields from a dipole, when comparing the fields within the room and in the open area. Details of the field falloff were not reproduced very well for the E field. A “room factor” of approximately 2 can be attributed to a small dipole within an enclosed room. Studies performed after the completion of this work showed that there was virtually no distance dependence on the RF fields from a linac within a clinical vault. This may be attributed to the fact that the modulator of a linac would act as an array of antennas rather than a single source and the non-negligible difference in the walls of a clinical vault compared to the walls of our measurement room.

2.7 References

Athey T.W., Stuchly M.A. and Stuchly S.S. “Measurement of the radio frequency of biological tissues with an open ended coaxial line, part 1” IEEE Trans. Microw. Theory Tech. **MTT-30** 82-86 1982.

Aqil S. Postdoctoral researcher, University of Alberta, Dept. of Phys. Private communication 2008.

Balanis C. “Antenna Theory” John Wiley and Sons Inc., New Jersey 2005.

Berenger J. P. “A perfectly matched layer for the absorption of electromagnetic waves” J. comp. phys. **114** 185-200 1994.

Burke B., Lamey M., Rathee S., Murray B. and Fallone B.G. “Radio frequency noise from clinical linear accelerators” Phys. Med. Biol. **54** 2483-2492 2009.

Burke B. “Measurement of radio frequency emissions from a medical linac” University of Alberta M.Sc. thesis 2008.

Christopoulos C. “The Transmission-Line Modeling (TLM) Method in Electromagnetics” Morgan and Claypool publishers, United States 2006.

Clement G. C. “A provisional ground conductivity map for Canada” Proc. IRE, **49** 1674-1678 1961.

De Cogan D., O'Connor W. J. and Pulko S. “Transmission Line Matrix in

Computational Mechanics" Taylor and Francis Group, New York 2006.

Grant J. P., Clarke R. N. Symm G. T. and Spyrou N. M. "A critical study of the open ended coaxial line sensor technique for RF and microwave complex permittivity measurements" J. Phys. E: Sci. Instrum. **22** 757-770 1989.

Hofer W. J. R. "Numerical Techniques for microwave and millimeter-wave Passive Structures" John Wiley and Sons Inc., New York Chapter 8 (edited by T. Itoh) 1989.

Jackson J. D. "Classical electrodynamics" John Wiley and Sons pp. 239-240 1999.

Johns P. B. "symmetrical condensed node for the TLM method" IEEE Trans. Microwave Theory Tech., vol. **MTT-35** pp. 370-377 1987.

Johns P. B. and Beurle R. L. "Numerical Solution of 2-Dimensional Scattering Problems using a transmission line matrix" Proc. Inst. Electr. Eng., **118**, 1203-1208 1971.

Jordan E. C. and Balman K. G. "Electromagnetic waves and radiating systems" Prentice-Hall Inc. New Jersey 1968.

Microstripes reference manual, Release 7.5, Copyright Flomerics 2006.

Ott H. W. "Noise reduction techniques in electronic systems" John Wiley and Sons Inc. 1988.

Robert A. "Dielectric permittivity of concrete between 50 MHz and 1 GHz and GPR measurements for building materials evaluation" J. Appl. Geophys. 89-94 1998.

Rzepecks and Stuchly S.S. "A lumped capacitance method for the measurement of the permittivity and conductivity in the frequency and time domain-a further analysis" IEEE Trans. Instrum. Meth. **IM-24** 27-32 1975.

Shrivastava V., Ranga Y "Ultra wide band CPW-fed printed pentagonal antenna with modified ground plane for UWB applications" IET int. conf. wireless mobile and multimedia networks 1-2 2008.

Singh M., Koul S.K., Basu A. "Coplanar Waveguide Fed Ultra Wide Band Monopole Antenna" RFM Int. RF and Mcirowave conf. 44-47 2006.

Stuchly S.S., Rzepecka P.A. and Iskander M.F. "Permittivity measurements at microwave frequencies using lumped elements" IEEE Trans. Instrum. Meth. **IM-23** 56-62 1974.

Stutzman W. L. and Thiele G. A. "Antenna theory and design" John Wiley and Sons Inc. New York 1981.

Chapter 3: Radio Frequency Noise from an MLC: a Feasibility Study of the use of an MLC for Linac-MRI Systems

A portion of this chapter has been submitted to the journal physics in medicine and biology: M Lamey, J. Yun, B Burke, S Rathee and B G Fallone "Radio frequency noise froman MLC: a feasibility study of the use of an MLC for linac-MR systems" Phys. Med. Biol.

3.1 Introduction

Due to the deleterious effects of extraneous RF noise on an MRI system, all possible RF sources in a linac-MRI system must be investigated. It is common practice to use multileaf collimators (MLC) for conformal or IMRT to shape a dose distribution around the target volume. If the position of a tumour was known in real-time during treatment, an MLC could be used to reduce the error margins used around the tumour by sculpting the radiation dose to the tumour. Several groups are actively studying the use of an MLC during real time tumour tracking, using non-MR imaging modalities, and the effects of MLC movement during radiotherapy [Sawant et al. 2008, Nill et al. 2005, Chen et al. 2009, Webb et al. 2008, Webb 2006a and Webb 2005]. It is well known that the DC motors which drive the MLC leaves produce RF noise [Suriano et al. 1998 and Jabbar 1991]. The RF noise is a result of the arcing between the commutator and brushes in the DC motor. A model of the noise production is introduced in section 3.2.2. Incorporation of an MLC into a linac-MRI system could create magnetic and RF interferences; these possible interferences must be studied.

The arrangement of an MLC is shown in Figure 3.1. The MLC consists of tungsten leaves which are used to attenuate radiation and sculpt the delivered dose. Power to provide motion to the leaves is implemented using DC motors. Within the motor casing is the gear box, the DC motor and an encoder which provides a specific number of pulses per turn. The information obtained from the encoder is used to determine the actual position of the leaf attached to a particular motor.

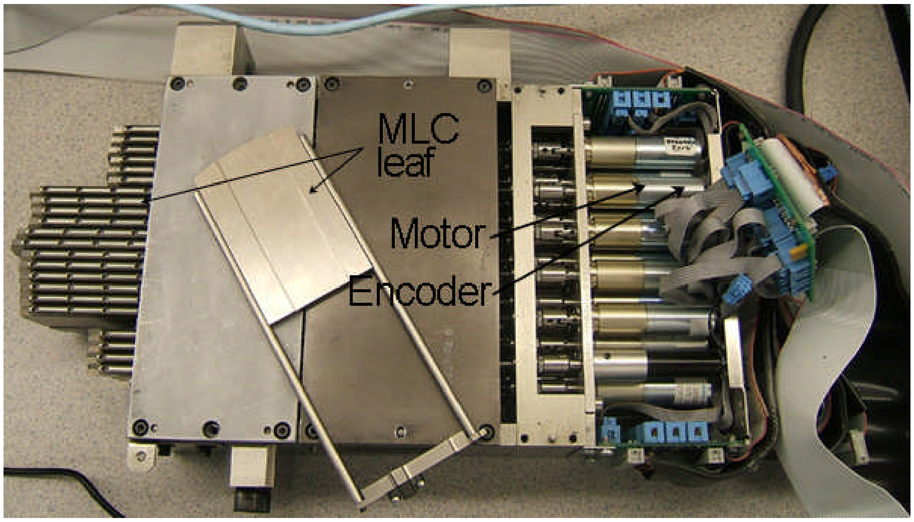

Figure 3.1: One half of a Varian 52 multileaf collimator showing the leaves, DC motors and encoders.

The investigation in this chapter reports on the results of studying the RF interference mentioned above. Using commercially available *E* and *H* field probes, the frequency spectrum of the RF noise from functioning MLC motors was measured as a function of the magnetic field applied to the motors (this thesis uses the convention of *H* when referring to magnetic field strength and *B* when referring to the magnetic field). In addition, MR images of a phantom were acquired with our linac-MRI system. The imaging was performed in order to study the effect of RF noise produced by the motors driving MLC leaves on: the signal to noise ratio (SNR) in images and difference maps between imaging with and without a functioning MLC.

3.2 Theory

The theory regarding the use of an MRI and MR imaging can be found in appendix C.

3.2.1 Probe Measurements

The measured RF noise from moving MLC leaves is presented as an RF power spectral density after subtracting background levels. Time domain signals from the E and H field probes were used to obtain measured spectral density, $M(f)$, in each case as follows:

$$M(f) = \sqrt{\frac{\sum_{i=1}^{N} \left|DFT_i\right|^2}{N}}, \tag{3.1}$$

where $DFT_i(f)$ is the discrete Fourier transform of one time domain acquisition, and N is the number of averages used in the estimation of $M(f)$.

The measured values, $M(f)$, from the E and H probes are related to the corresponding field strengths by applying a performance factor $PF(f)$. For example, the E field is related to the measurement as follows.

$$E = M(f) \cdot PF_E(f). \tag{3.2}$$

Substitute H for E in Equation (3.2) for the H field. A thorough analysis of the performance factors for the near field probes can be found in Appendix A. The approximate power spectral density (P) of the RF noise was then calculated using the following formula:

$$P_{Upper} = \frac{E \cdot H}{2}. \tag{3.3}$$

The use of Equation 3.3 provides an upper limit to the measured power. The time averaged power, P, is given by $P = \mathrm{Re}\left(\vec{E} \times \vec{H}^{*}\right)/2$, which makes Equation 3.3 an upper limit. The background levels, i.e. those measured with the MLC not functioning, were subtracted from the measured power with the MLC moving as in Equation 3.4.

$$P = PF_E(f) \cdot PF_H(f)[M_E(f) \cdot M_H(f) - M_{Eb}(f) \cdot M_{Hb}(f)]/2 \tag{3.4}$$

The individual subscripts refer to the E or H fields, and Eb and Hb subscripts refer to the measured background fields. The variance of the E or H field is related to the variances in *M(f)* and *PF(f)*. The variance on the background subtracted power density, *P(f)*, increases with decreasing frequency as explained below. Due to the uncertainty of the performance factors, of approximately 1 dB, we assign an error of 10% to measured field values. Since 1000 averages were taken in estimating *M(f)*, the error in *M(f)* was determined to be negligible compared to the error in the performance factors. With the estimation of a 10% error associated with the field strengths due to the performance factors and neglecting errors in *M(f)*, and using error propagation rules it can be shown that the error in the power above background as a function of frequency is given by:

$$\delta P(f) = 0.07 PF_E(f) PF_H(f)[M_E(f) M_H(f) - M_{Eb}(f) M_{Hb}(f)]. \tag{3.5}$$

Both E and H field performance factors increase as frequency decreases (see

Figure A.3). Therefore the variance on the power increases at lower frequencies.

3.2.2 DC Motor Operation and RF Noise Model

Current Varian clinical machines use a brushed DC motor to drive the MLC leaves. Since this is the only usable MLC available for this investigation, a few comments regarding the brushed DC motor are in order. A brushed DC motor consists of a commutator, brushes, a stationary permanent magnet and a rotor (electromagnet with a winding). A simple schematic, with the major components, of a brushed DC motor is shown in Figure 3.2.

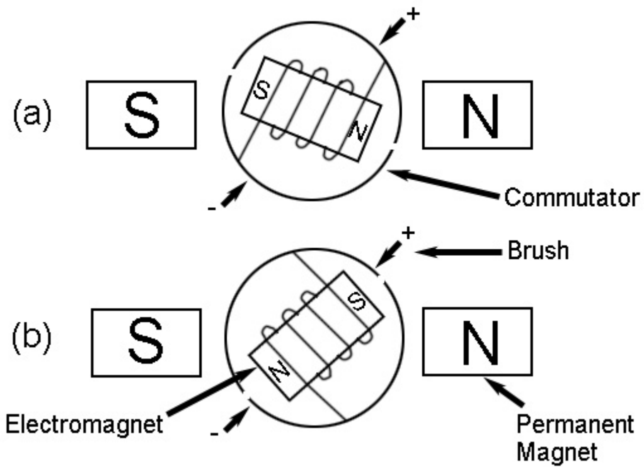

Figure 3.2: Simple schematic of the operation of a DC motor illustrating the relation between the major components.

The brushes make electrical contact with the commutator and provide the current through the electromagnet. The commutator consists of two semi-circular arcs which rotate along with the electromagnet. The windings of the electromagnet are connected to the commutator. When the electromagnet is in the position shown in Figure 3.2 (a) it feels a force from the permanent magnet, moving it in a clockwise orientation. Once the commutator has rotated sufficiently a gap is passed and the bias on the electromagnet is reversed. Now the electromagnet feels an attractive force which gives it a further push in the clockwise direction. In this way the motor can move in a clockwise fashion as long as bias is supplied to the electromagnet.

The RF noise from a brushless motor was also investigated. A simplified schematic for a brushless motor is shown in Figure 3.3. In this case the electromagnets are stationary and the permanent magnet rotates. Suriano [Suriano et al. 1998] states that the RF noise is a result of brush contact with the commutator. The RF noise from a brushless motor was investigated, since as shown in Figure 3.3, there is no commutator or brush for possible arcing. As described below, we expect that there will be a reduction in measured RF noise.

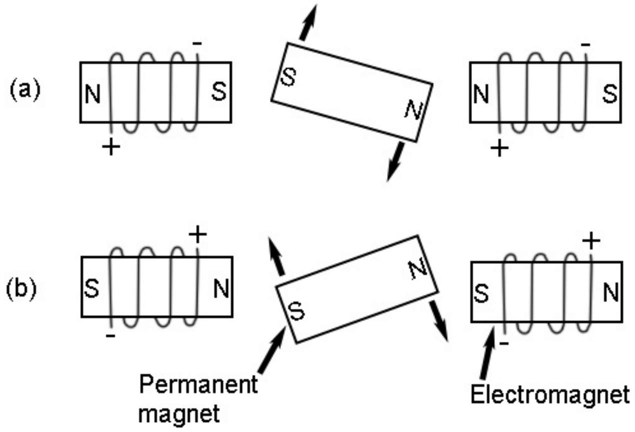

Figure 3.3: Simplified schematic of a brushless motor. The arrows signify the direction of the force on the permanent magnet.

Models of the emissions of RF noise from DC motors have been suggested. Suriano [Suriano et al. 1998] suggests a model which consists of a monopole antenna above a pseudo-ground plane. When interpreting our data this model was adopted. It is well known that arcing occurs between the brushes and commutator [Holm 1962, Padmanabhan et al. 1965 and Suriano 1989]. When the brush passes the commutator gap a new electrical connection is established and the old electrical connection is severed, thus arcing will occur. The model suggests that the arcing which occurs between the brushes and commutator acts as an input for the wiring into the DC motor, it is this wiring that acts as a monopole antenna.

The frequency range over which data was taken was up to 400 MHz; specifically the band near 9.3 MHz was of particular interest. The MRI in our prototype system has a field strength of 0.22 T, the Larmor frequency for this field strength is 9.3 MHz (see Appendix C for a discussion). Noise at the Larmor frequency will directly degrade the image quality. This necessitated measurements in the near field, see Appendix A section A.5. Near field measurements introduce complications such as antenna coupling and polarization effects. Consider the arrangement shown in Figure 3.4. The near-fields from a monopole antenna of height h above a ground plane of zero-extent and with a sinusoidal excitation can be derived. The magnetic vector potential for an electrically thin element (a << λ) is given by Balanis [Balanis 2005]:

$$\vec{A} = \hat{z}\mu_0 I(0)\int_0^h \frac{\sin[k(h-z')]e^{-jkr'}}{r'}dz' \tag{3.6}$$

Where μ_0 is the permittivity of free space, *I(0)* is the initial current, $k = 2\pi/\lambda$, r' is the distance ($[x-x')^2+(y-y')^2+(z-z')^2]^{1/2}$) from the measurement point, P, to the antenna and $\hat{z}$ is the radial unit vector in cylindrical coordinates.

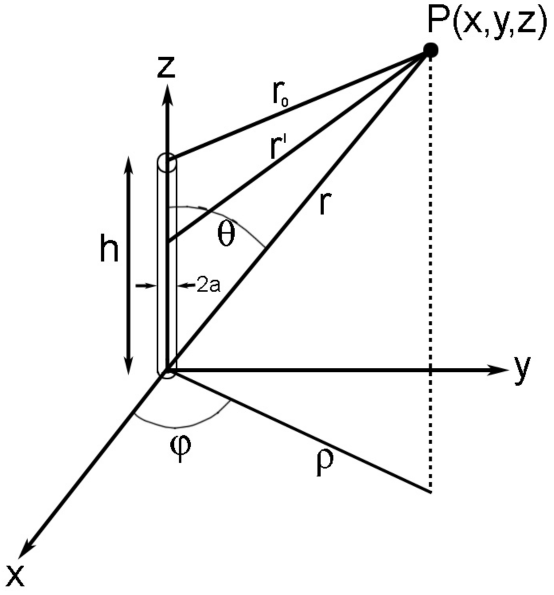

Figure 3.4: geometrical arrangement of a monopole antenna illustrating the specification of a measurement point, P, with respect to the antenna.

The magnetic and electric field intensities are given by:

$$\begin{aligned} H &= \frac{1}{\mu_0}(\nabla \times A) = -\hat{\varphi}\frac{1}{\mu_0}\frac{\partial A_z}{\partial \rho} \\ E &= \frac{1}{j\omega\varepsilon_0}(\nabla \times H) = -\hat{\rho}\frac{1}{j\omega\varepsilon_0}\frac{\partial H_\varphi}{\partial z} + \hat{z}\frac{1}{j\omega\varepsilon_0 \rho}\frac{\partial}{\partial \rho}(\rho H_\varphi) \end{aligned} \quad . \quad (3.7)$$

Closed form expressions for the *E* and *H* fields are given by Stratton [Stratton 2007].

$$\begin{aligned} H_\varphi &= \frac{jI(0)}{4\pi\rho\sin(kh)}[e^{-jkr_0} - \cos(kh)e^{-jkr} - \frac{jz}{r}\sin(kh)e^{-jkr}] \\ E_\rho &= \frac{jI(0)\eta}{4\pi\rho\sin(kh)}\left[\frac{(z-h)e^{-jkr_0}}{r_0} - \frac{z}{r}\cos(kh)e^{-jkr} + \sin(kh)e^{-jkr}\left(\frac{1}{kr} - \frac{z^2}{kr^3} - \frac{jz^2}{r^2}\right)\right] \quad (3.8) \\ E_z &= \frac{-jI(0)\eta}{4\pi\sin(kh)}\left[\frac{e^{-jkr_0}}{r_0} - \cos(kh)\frac{e^{-jkr}}{r} - z\sin(kh)e^{-jkr}\left(\frac{j}{r^2} + \frac{1}{kr^3}\right)\right] \end{aligned}$$

where η is the wave impedance of free space ~ 377 Ω. The Equations given by (3.8) are valid under the conditions: $b/\lambda < 10^{-4}$ and $h/\lambda < 0.25$ [Weiner 2003], where b is the radius of the antenna wire.

3.3 Materials

An EEV M4261 electromagnet (now e2v, Chelmsford, England) with a DCS 33-33 (Sorensen, Azusa, California, USA) power supply was used to produce a B field. The MLC motors were placed in the electromagnet poles thus subjecting the MLC motors to a B field. The size of the electromagnet was such that approximately 13 of the 26 motors from one jaw of a Varian 52 leaf MLC were in the field. The E and H fields from the operation of one MLC motor were measured using the near field HZ-11 probe set (Rohde and Schwarz, Munich, Germany). The E probe measures the total E field strength while the H probe was used to measure the three individual orthogonal components of the H field strength; these three components were added in quadrature to obtain the total H field strength. A 3M12-2-2-0.2T (Senis Gmbh, Zurich, Switzerland) Hall probe with a 3-axis type C-H3A-E3D-1%-0.2T magnetic field transducer was used to measure the applied B field on the MLC motors under test. The RF noise from three motors was investigated: 1) a 24 V DC brushed motor used in a Varian 52 leaf MLC (Part #: 886603-03, Micro MO Electronics, Clearwater, Flordia, USA), 2) a 24 V DC brushed motor used in a Varian 120 Millennium MLC (Part #: 344516, Maxon Motor, Sachseln, Switzerland) and 3) a 48 V brushless DC fan motor (Part # : 4712KL-07W-B30, NMB Technologies Corporation, Chatsworth, California, USA). One thousand DFT averages were taken for each of the Varian 52-leaf, Varian Millennium and brushless fan motors. The field probes were used to measure the power spectral densities in the following cases: 1) the background RF without motor movement, 2) the RF noise due to functioning motors without an applied *B* field, 3) the RF noise produced by functioning motors subjected to 50, 100 or 500 Gauss *B* field and 4) the RF noise produced from 13 functioning Varian 52-leaf motors driving 13 MLC leaves as a function of distance from the MLC with no applied *B* field.

The motor drive board contains 26 H-Bridge chips and were used to control all motors with a 400 W power supply (SMQ400PS24-C, XP Power, Haw Par Technocentre, Singapore). For real-time control of many motors (on/off, direction), a PCI-bus control module based on field programmable gate arrays was used (National Instruments, Austin, Texas). To program and implement motion patterns of the MLC, LabVIEW v.8.5 (National Instruments, Austin, Texas) was used.

In a separate investigation, MR images of a phantom were acquired with our 0.22 T linac-MRI system [Fallone et al. 2009]. One half of a Varian 52-leaf MLC was placed near the MRI magnet and phantom images were acquired while 13 MLC leaves were moved. In one case, the MLC and the associated cables were non-shielded while in the other case the MLC and cables were shielded. The phantom was an acrylic rectangular cuboid ($15.95 \times 15.95 \times 25.4$ mm^3) with three holes of diameters 2.52, 3.45 and 4.78 mm drilled into it, inserted into a 22.5 mm diameter tube and filled with a 10 mM solution of $CuSO_4$. The MRI console is as described by Fallone [Fallone et al. 2009]; a TMX NRC (National Research Council of Canada, Institute of Biodiagnostics, Winnipeg, MB, Canada). The console software is based on Python programming language (Python Software Foundation, www.python.org), version 2.3.4, to allow the user full control of development and modification of pulse sequences. Analogic (Analogic Corporation, Peabody, MA) AN8295 gradient coil amplifiers and AN8110 3 kW RF power amplifiers are used in the TMX NRC system.

3.4 Methods

3.4.1 Measurement of RF Noise from Motors

The *E* and *H* field strengths were measured at distances perpendicular to the movement of the MLC leaves. The setup used to measure the RF noise is shown in Figure 3.5. This orientation was chosen since the RF noise at the position of an MRI coil is the quantity of interest. A linac-MRI system will have an MLC which runs perpendicular to the direction of radiation. The RF noise perpendicular to the motion of the MLC will be the location of the patient and the MRI coil. The time domain signal from the field probes was first amplified using a Rhode and Schwarz broadband preamplifier (model 7405-907BNL), then transferred from the oscilloscope to a PC using a Keithley KUSB 488 GPIB interface (Keithley Instruments Inc, Cleveland, OH). The software program DADiSP (DSP Development Corporation, Newton, MA) was then used to calculate the *E* and *H* field spectral densities, as per Equation (3.1). The slight frequency response of the amplifier was known and taken into account for.

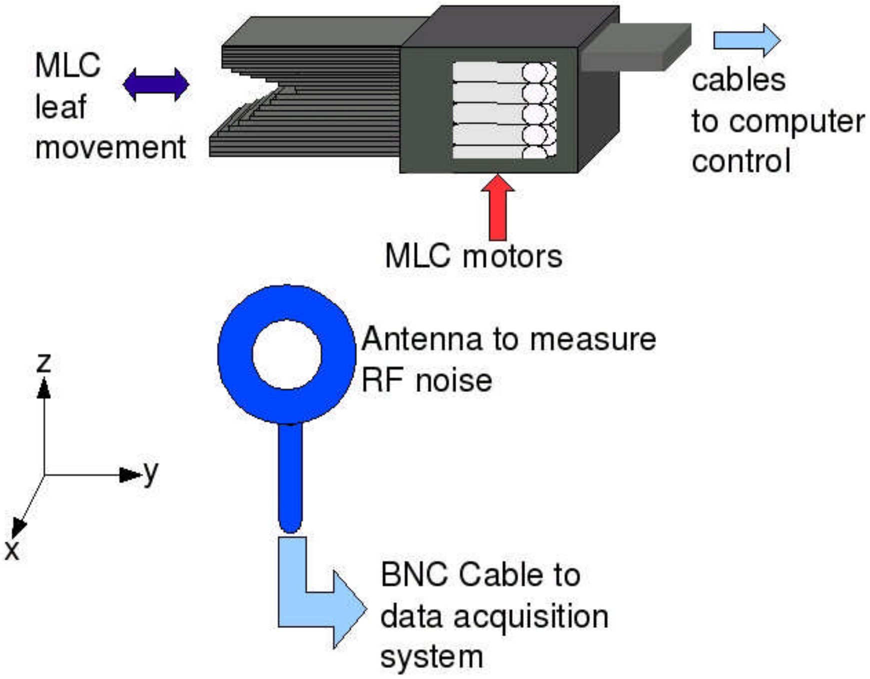

Figure 3.5: Setup used to measure the RF noise from a functioning MLC. A loop probe was used to measure the individual magnetic field strength components while a "ball" probe was used to measure the total electric field strength. Not shown is the electromagnet used when a *B* field was applied to the MLC motors.

The resulting DFTs had bin widths of 50 kHz in the frequency domain. The 50 kHz bins are a result of the total acquisition time used to acquire the data. A total acquisition time of 20 μs resulted in 50 kHz bins (1/20μs = 50 kHz). As mentioned previously, the signal averages in Equation (3.1) was 1000 for each of the three motors investigated. The approximate power spectral density of the RF noise was calculated using Equation (3.3), which provides an upper limit to the measured power. The measured background power spectral density was subtracted from the RF power spectral density produced by functioning motors in each case. Two distinct power spectral density measurements were taken: 1) the RF noise from a single continuously functioning motor as a function of applied *B* field (0, 100 and 500 Gauss for the brushed motors and 0, 50 and 100 Gauss for the brushless motor) at a distance of 50 cm and 2) the RF noise as a function of distance from one half of a Varian 52-leaf system with 13 motors continuously moving at distances of 50, 70 and 100 cm. For measurements near background, the standard deviation was estimated by measuring 20 background power spectrums, each of which was done with 1000 averages. The standard deviation of these background power spectra at each frequency was then used as our estimate of the error.

3.4.2 A Functioning MLC Near an MRI

The setup used during the imaging study is shown in Figure 3.6. An MR image was acquired with the MLC not present. Then an MR image was taken with the MLC at a specific distance from the center of the magnet, first with the MLC static and then with 13-leaves moving. Images were acquired with the MLC plus cables unshielded and shielded. The shielding consisted of a copper box enclosing the motors used to drive the MLC leaves. The ribbon cables used to control movement of the motors were wrapped in aluminum foil. Any small holes or seams were covered over with conductive copper tape or filled with copper wool. In this experiment 13 MLC leaves were moved at a time from a Varian 52-leaf system. The MLC was placed on a stand such that the approximate height of the leaves and motors was the same as that of the coil used to image in the 0.22 T MRI. Images with stationary MLC leaves investigated a possible magnetic effect from the presence of the MLC. The distances presented herein are those from the face of the MLC to the center of the MRI coil; which was located approximately at the center of the MRI magnet. Images were taken in four different orientations of the MLC and imaging coil: 1) the MLC and coil oriented as shown in Figure 3.6, 2) the coil as shown in Figure 3.6 and the MLC leaves oriented vertically, 3) the MLC leaves oriented vertically, and the coil and phantom rotated 90° toward the MLC and 4) the MLC as shown in Figure 3.6 and the coil and phantom rotated 90° toward the MLC.

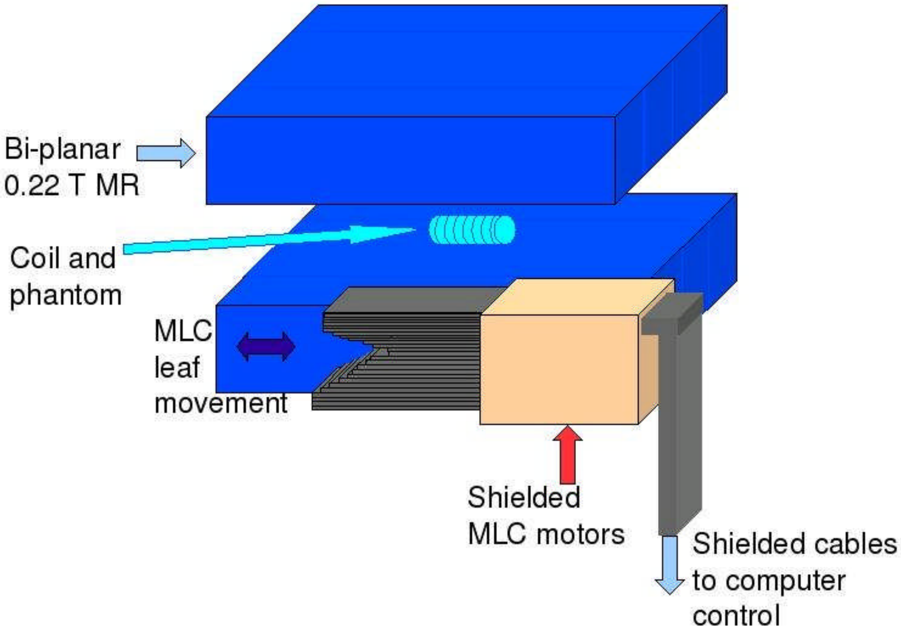

Figure 3.6: Setup used to acquire images of a phantom while 13 leaves of an MLC were moved continuously. Images were taken with the MLC leaves static and then moving as well as with the MLC motors and cables non-shielded and shielded.

The following settings were used in a gradient echo MR imaging sequence; flip angle: 60°, slice width: 5 mm, acquisition size: 128 (read), 128 (phase encode), FOV: 50×50 mm^2, TR: 300 ms, TE: 35 ms, 1 signal average. The resulting image quality or change in image quality was evaluated using the SNR and image subtraction (MLC leaves stationary to MLC leaves moving for the same orientation and distance). The SNR for each resulting image was calculated by taking the mean pixel intensity in a solution containing region inside the largest of the three holes in the phantom, divided by the standard deviation in a similar sized region of the noise near one of the corners of the image. The corners were used to avoid any possible artefact effects in the phase or read encode directions.

3.5 Results

Figure 3.7 shows the measured RF noise by the *E* field probe in the time domain from a Millennium DC motor. The “spike” shown is one of the larger spikes in both amplitude and duration. Figure’s 3.8, 3.9 and 3.10 show the results of the RF power spectral density above background as a function of applied *B* field, for each of the three motors investigated, at a measurement distance of 50 cm. Data has been shown in the frequency range 8 - 70 MHz. The data shown is then useful for all linac-MRI systems operating with an MRI between 0.2 and 1.5 T. Figure 3.11 shows the measured power spectral density from thirteen motors driving thirteen leaves from a Varian 52-leaf MLC at distances of 50, 70 and 100 cm with no applied *B* field.

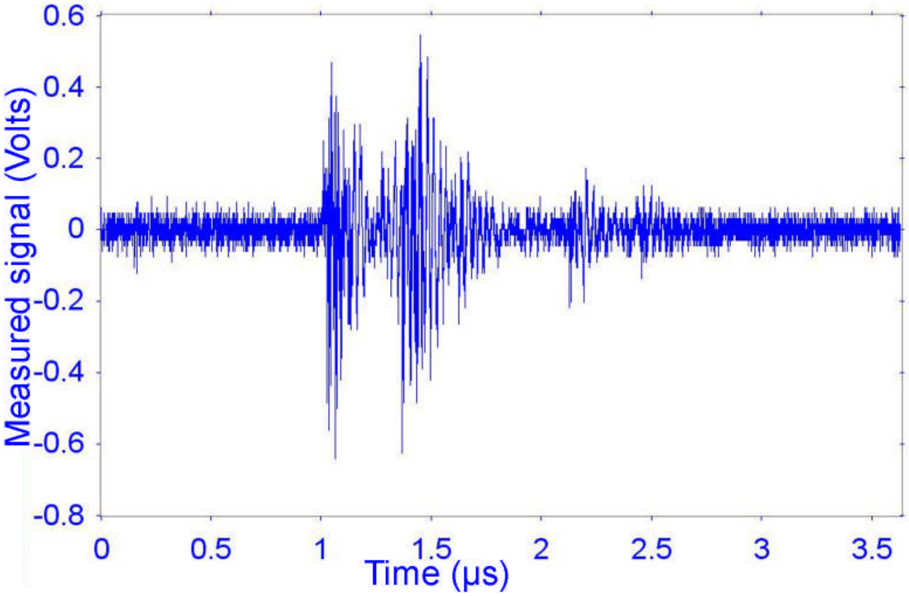

Figure 3.7: One of the larger RF “spikes” as measured by the *E* probe and broadband preamplifier from the Millennium MLC motor. These spikes were resolved by a time domain resolution of 0.5 nsec.

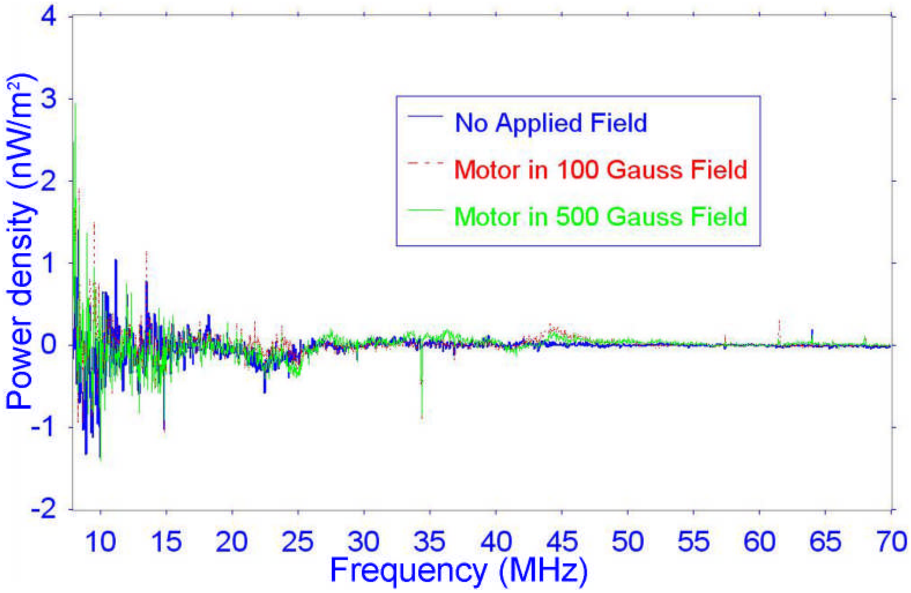

Figure 3.8: Background subtracted RF noise power spectral density measured from a Varian 52-leaf MLC motor as a function of applied magnetic field at 50 cm.

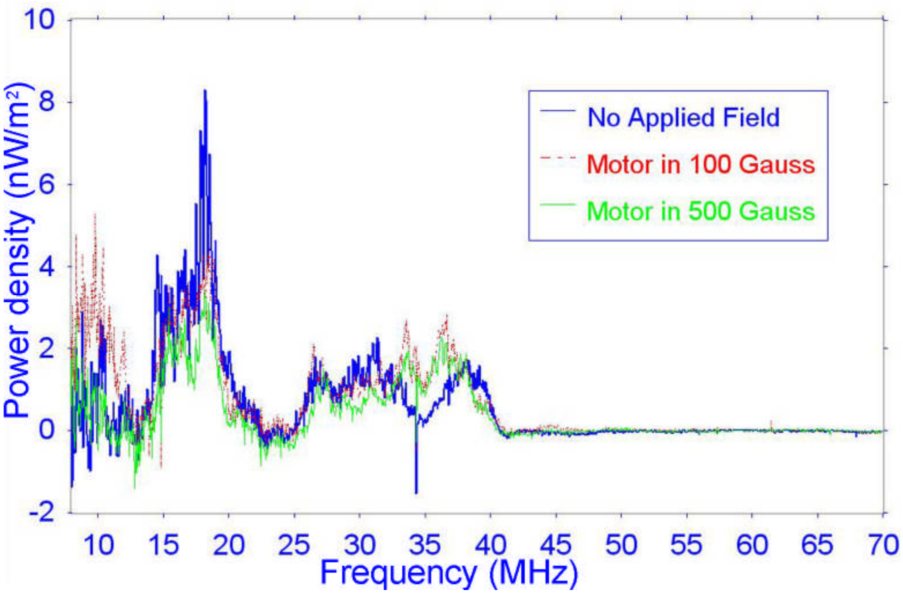

Figure 3.9: Background subtracted RF power spectral density measured from a Millennium MLC motor as a function of applied magnetic field at 50 cm.

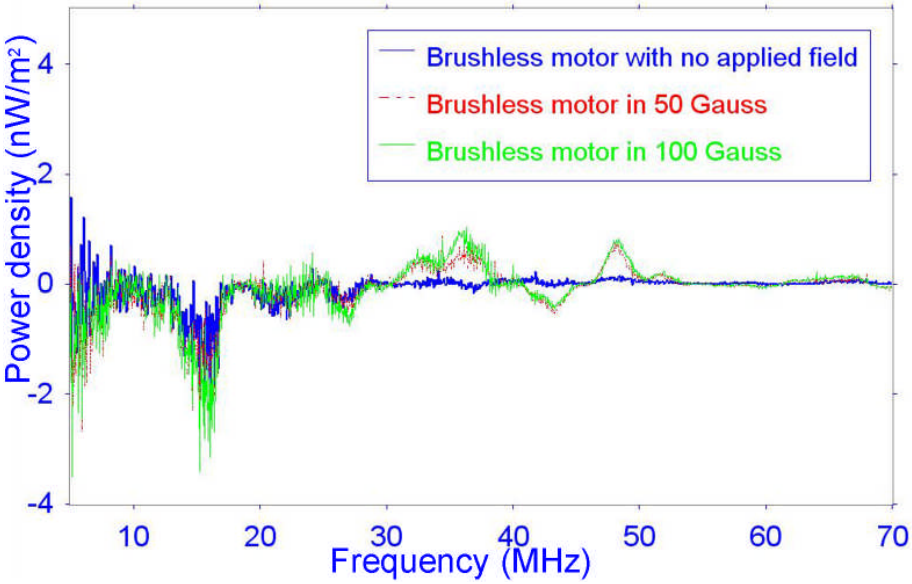

Figure 3.10: Background subtracted RF power spectral density as measured from a brushless fan motor as a function of applied magnetic field, 50 cm from the motor.

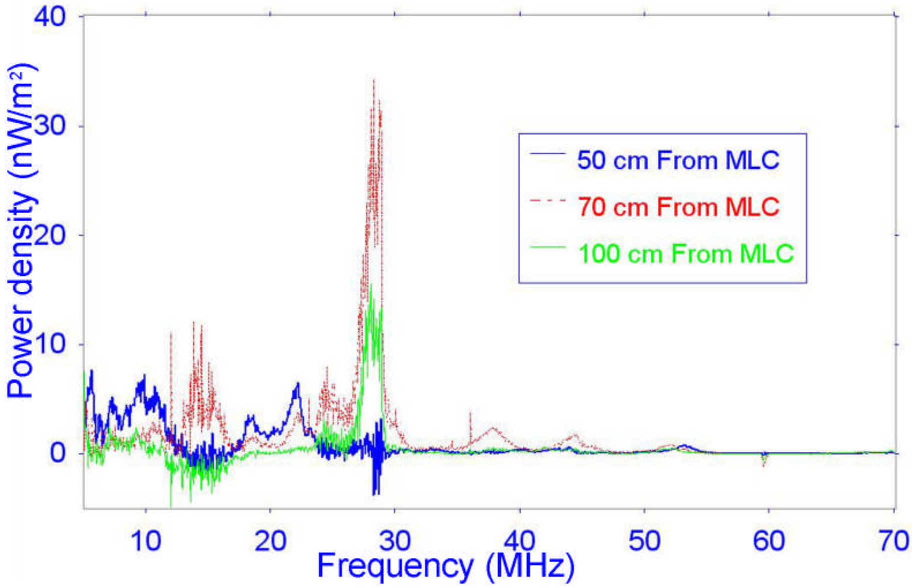

Figure 3.11: Background subtracted RF power spectral density as a function of distance from a Varian-52-leaf MLC with 13 leaves moving. No magnetic field was applied to the motors in this case.

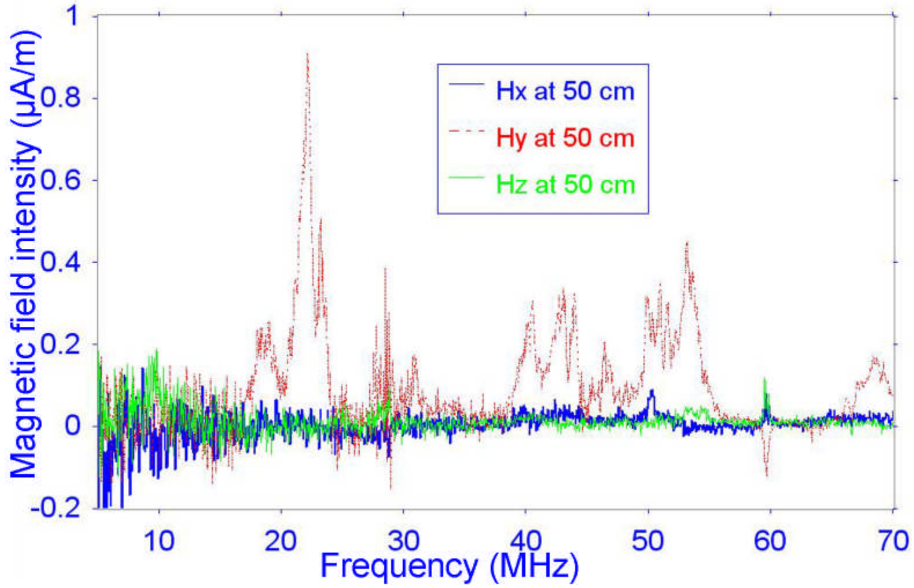

Figure 3.12: Background subtracted individual Cartesian components of the magnetic field strength from the MLC, with 13 leaves moving. The Cartesian orientations with respect to the MLC orientation are shown in Figure 3.6.

Figure 3.12 shows the three individually measured Cartesian magnetic field strength components in the range from 5 – 70 MHz; clearly showing that one component, H_y, of the measured field dominates. In this case, 13 motors from one half of the Varian 52-Leaf MLC were continuously moved. The Cartesian orientations with respect to the MLC are shown in Figure 3.5; specifically H_y is along the same direction as the MLC leaf movement or the motor axis.

The second part of the study involved imaging a phantom while thirteen leaves of a Varian MLC system were moved (Figure 3.6). Table 3.1 shows the results of the measured SNR for each of the previously described orientations used. For each orientation the SNR is shown with the MLC unshielded, leaves stationary and moving (columns two and three) and then with the MLC shielded, leaves stationary and moving (columns four and five). The acquired images with the MLC at 70 cm from the MR coil for each unshielded and shielded case in orientation two (i.e. coil as in Figure 3.6 but MLC leaves travel in vertical direction) are shown in Figure 3.13. Figure 3.14 shows the subtraction of Figures 3.13 (c) and 3.13 (d); this is the case where the MLC is shielded.

Table 3.1: SNRs of the image of a phantom with half of a Varian 52-leaf MLC was brought near the MR. SNRs shown are for the MLC stationary and thirteen MLC leaves moving both in the non-shielded and shielded cases.

1st Orientation	No shielding		With shielding	
Distance (cm)	SNR MLC stationary	SNR MLC moving	SNR MLC stationary	SNR MLC moving
70	48	29	49	51
100	46	46	52	49
2nd Orientation	No shielding		With shielding	
Distance (cm)	SNR MLC stationary	SNR MLC moving	SNR MLC stationary	SNR MLC moving
70	46	35	52	53
100	45	44	51	52
3rd Orientation	No shielding		With shielding	
Distance (cm)	SNR MLC stationary	SNR MLC moving	SNR MLC stationary	SNR MLC moving
70	57	48	57	58
100	58	56	58	58
4th Orientation	No shielding		With shielding	
Distance (cm)	SNR MLC stationary	SNR MLC moving	SNR MLC stationary	SNR MLC moving
70	56	51	58	56
100	59	57	56	55

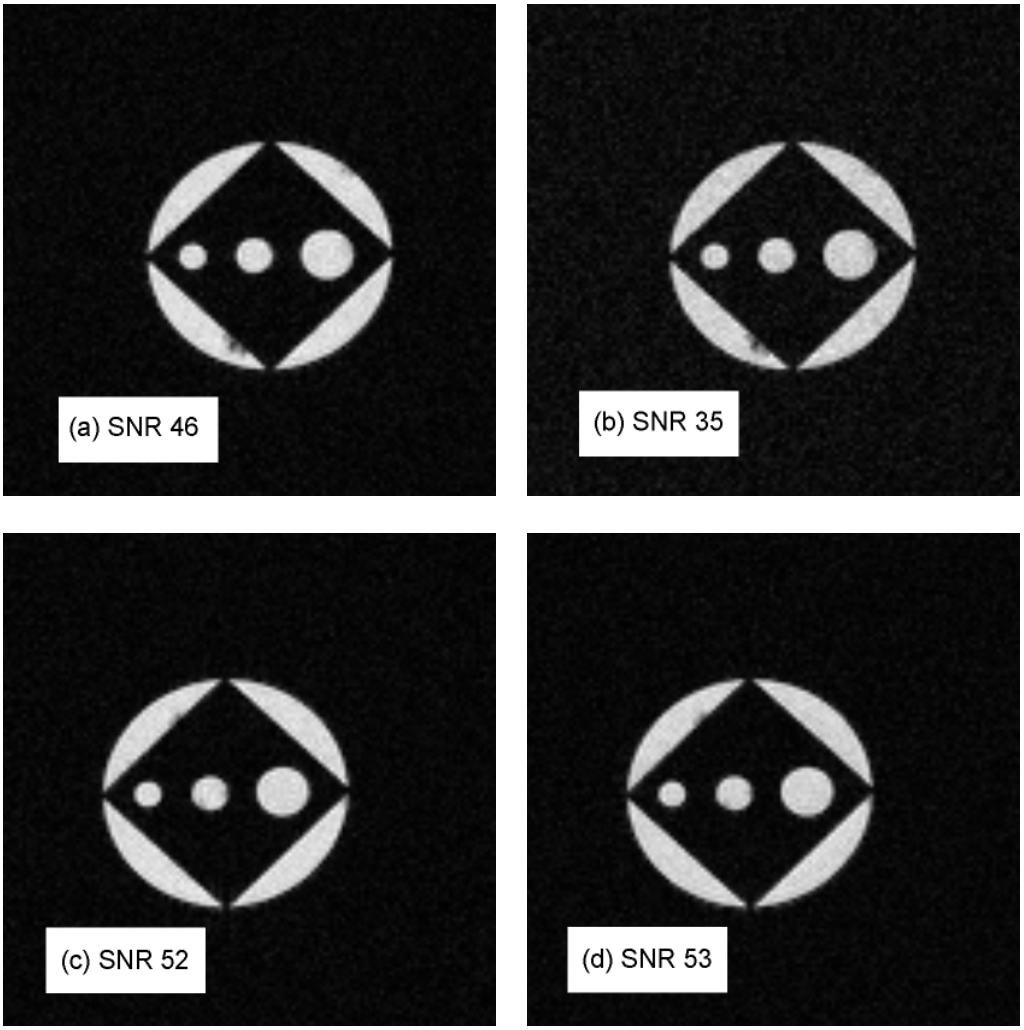

Figure 3.13: Images at 70 cm obtained with the 2nd orientation (a) MLC unshielded and stationary (b) MLC unshielded and 13 leaves moving (c) MLC shielded and stationary (d) MLC shielded and 13 leaves moving.

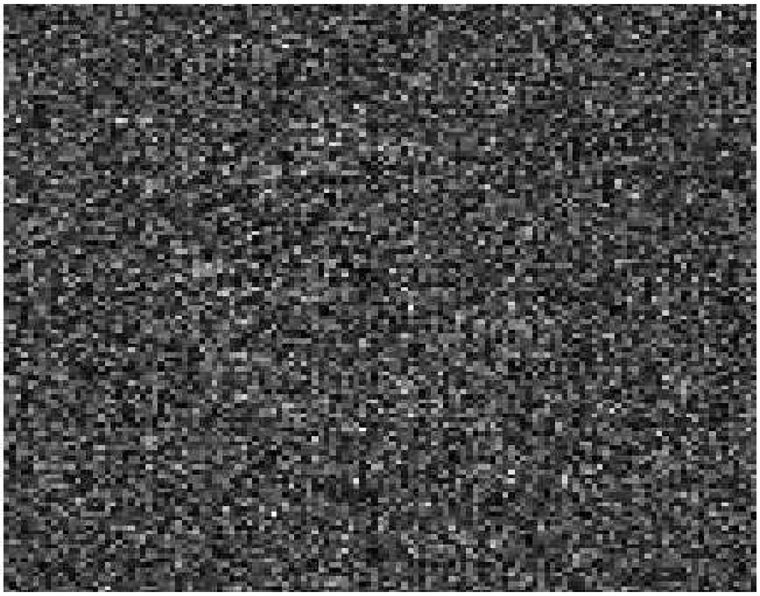

Figure 3.14: Subtracted image with the MLC and phantom in the second orientation. The MLC and cables were shielded; Figure 3.13(c) and Figure 3.13(d) were used for the subtraction.

The acquired k-space data for the cases of a stationary MLC and a functioning MLC are shown in Figure 3.15. It can be seen from the acquired data that noise is added to the acquired data. The noise seemed both random and to have some line dependence in k-space, as can be seen from the horizontal in the data.

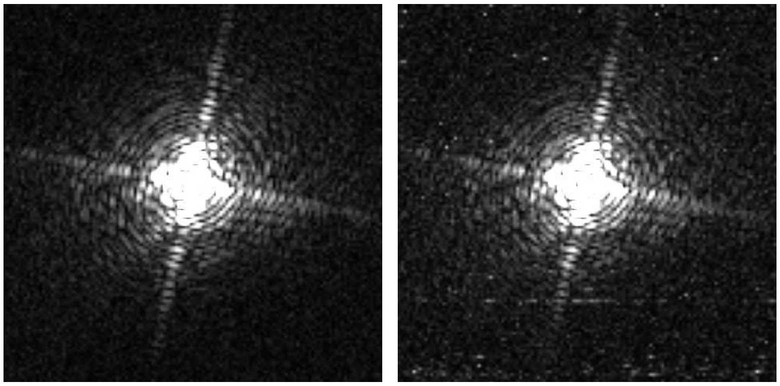

Figure 3.15: Acquired k-space data with the MLC stationary (left) and with the MLC functioning (right).

3.6 Discussion

The use of an MLC during the radiotherapy process will be important for linac-MRI systems, which can take advantage of real-time tumour imaging and tracking with dynamic MLC delivery. With the close proximity to an MRI unit, the MLC leaves and the motors used to drive them will be placed in a magnetic field. The motors will also produce RF noise which can degrade image quality. The RF power spectral density was measured from three motors as a function of applied magnetic field to the motors. In the time domain spikes of measured noise were observed when the MLC motors were running. These spikes were more prevalent for the Millennium MLC motors. The Millennium MLC motor runs faster thus contributing to the increase in visible RF noise. These small spikes seen in the time domain are a result of arcing between the brushes and commutator bars in the motors resulting in the production of broadband noise [Suriano et al. 1998]. The spike shown in Figure 3.7 lasts on the order of a few microseconds. Generally the length of these spikes was on the order of a hundredth to a few tenths of microseconds. No visible RF noise above background was seen in the time domain when the brushless fan motor was operating, although in the frequency domain a small amount is visible (Figure 3.10).

Although small infrequent spikes were seen in the time domain for the Varian 52 leaf motor no significant RF noise above background was seen in Figure 3.8. For the Millennium MLC motor, Figure 3.9, there is a small dependence on the applied *B* field. In the frequency range 15-20 MHz, the RF power reduces for higher applied *B* field. No other systematic dependence can be seen. Above 40 MHz there seems to be no measured RF noise, therefore our measurements indicate that little or no RF noise exists at the Larmor frequency for MRI systems around or above 1 T. The function and RF noise production by a brushless fan was investigated since brushless motors produce less RF noise [Valentine 1998]. Above an applied field of 100 G the brushless fan motor showed both audible and visible (slower revolutions per minute) strain, therefore no results above 100 G are shown for this motor. This noticeable strain was likely due to the reduced magnetic shielding around the fan motor as compared to that of the MLC motors used. Near 15, and between 30 - 55 MHz, there seemed to be a dependence on the applied *B* field. It is unclear as to why the measured power density seems to dip below that of background around 15 MHz, the effect requires further investigation. When the RF noise from 13 motors from a Varian 52-leaf MLC were studied as a function of distance, Figure 3.11, no clear dependence could be seen.

The increased noise in the measured RF noise power spectral density at lower frequencies in Figures 3.8, 3.10 and 3.12 are a result of the increasing performance factor of both the *E* and *H* probes (see Figure A.3 of Appendix A). The variance on the measured power spectral density is proportional to the product of the *E* and *H* probe factors (as shown above), these factors increase as frequency decreases, therefore leading to larger variance at lower frequencies. Near the lower frequencies shown in Figures 3.8 - 3.12 the background subtracted power spectral density dips below zero. This does not mean the actual power is negative, which would be unphysical, this occurred since we were trying to measure powers similar to that of the background power. Besides the small area near 15 MHz in Figure 3.10, the data illustrates that on average we could not differentiate between the measured background power and that of the power emitted by the motors. The background was subtracted in the frequency domain since, if subtracted in the time domain, would lead to misleading results near lower frequencies with all the data shown being positive. In such a case one would then presume an average power above zero existed, which is not the case.

As previously stated, to estimate the error in our background subtracted power spectral densities, the standard deviation at a particular frequency was determined from 20 background measurements. The errors at 8, 10, 15, 20 30 and 50 MHz are estimated as 0.8, 0.7, 0.3, 0.1, 0.07 and 0.07 nW/m^2. The data in Figures 3.8 - 3.12 become "noisy" near 10MHz and below, because the estimation of the error is similar to the variance in the data shown in these plots. The standard deviations at 1 and 2 MHz were 10 and 4 nW/m^2.

Suriano [Suriano et al. 1998] propose a model for the emission of RF noise from a DC motor. The model is a described earlier in section 3.2.2. The *E* and *H* fields were given in Equation 3.8. A monopole antenna preferentially emits power perpendicular to the axis of the dipole, while no power is emitted by the monopole along its axis. When measuring the RF noise perpendicular to the direction of MLC motion (as shown in Figure 3.5) the model predicts a single *H* field component. The data presented in Figure 3.12 agrees with this model and with the specific component expected to be present. When data is measured along the axis of motion of the MLC leaves the model predicts zero measured power. We measured the power along the MLC leaf movement axis and found that in the same frequency range shown (5 - 70 MHz) the power spectral density is below 1 nW/m^2. We might expect a small amount due to the fact that our cable system did not present a perfectly straight and rigid monopole. Thus, these measurements qualitatively support this prediction. It is not purported to say that the model by Suriano [Suriano et al. 1998] has been rigorously validated, but only that our measurements of the three Cartesian components of the H field both perpendicular and parallel to the movement of the MLC leaves support the model.

A further note to the antenna model is that Suriano [Suriano et al. 1998] suggest that the motor casing, although quite small to the size of the wiring, acts as a pseudo-ground. A monopole antenna above a true ground plane acts as a dipole antenna. A dipole antenna produces fields in the same directions as the monopole fields given in Equation 3.8. Our data qualitatively supports either model.

Images of the phantom were taken by placing the MLC at distances of 70 and 100 cm (Figure 3.13) from the MRI coil. In Table 3.1 we can see that when the MLC was unshielded the measured SNR was reduced in each of the MLC-coil orientations when the MLC was functioning. Also shown in Table 3.1 is the measured SNR when the MLC motors and cabling was shielded. In each of the shielded orientations there was neither visible difference between the images nor any experimentally significant difference in the measured SNR obtained with and without continuous MLC motion. These results illustrate that we can effectively shield the RF noise produced by an MLC to the extent that no degradation in image quality and SNR occurs. In each case several images were taken and no effects of the RF noise produced by the shielded MLC plus cables were noticeable. Below 70 cm magnetic effects from the MLC casing to the MRI started to become noticeable, therefore the RF noise could not be studied independently of these magnetic effects. When the MLC was placed at 60 cm from the center of the MRI, image artefacts were seen even when the MLC was stationary. For our linac-MRI system we plan to fabricate an MLC casing which will be constructed of non-magnetic materials to reduce magnetic effects. We note that an MLC positioned at 70 cm is further away from isocenter than current clinical systems, however, for a linac-MRI system the MLC may be placed around 70 cm from isocenter. In Table 3.1 there is also a slight difference between the measured SNR when the MLC was shielded as compared to when it was not shielded (for instance even when the MLC was held static). This difference was due to having to re-orient the phantom or reposition the MLC, thus the same image slice may not have been imaged. However from one static MLC image to the associated image with the MLC moving nothing was changed in the setup. The parameter of interest was the change in SNR (or image quality) from the static MLC case to the associated SNR for a functioning MLC.

Images of the phantom were subtracted from one MLC stationary case to the associated MLC leaves moving case. The results for the second orientation, Figure 3.14, showed that when the MLC motors and cables were shielded the images were nearly identical. When the MLC was shielded, no visible differences between the images acquired with the MLC leaves stationary and with the MLC leaves moving could be seen.

When the MRI image data was viewed in k-space, random noise was seen when the MLC was functioning and unshielded, as shown in Figure 3.15. This random noise in k-space leads to an overall increase in the noise of the image. The noise may have also had some dependence on the line in k-space read in. This may have been due to a change in direction of the motor when approaching the end of the MLC leaf movement. After the MLC was shielded however, this random noise was not seen in k-space.

3.7 Conclusions

It has been shown that the RF noise produced by a continuously functioning MLC can be effectively shielded. No difference can be seen in image quality when the shielded MLC was stationary and when the motors were used to drive the leaves. The currently used Varian 52-leaf MLC motors and Varian Millennium 120 leaf MLC motor did not show any trouble operating in up to a 500 gauss applied field. The Varian motors did not produce a significant change in radiated RF noise when they were placed in a magnetic field. If brushless motors are to be used in place of brushed motors for reduced RF noise production, magnetic shielding may be required. This study has shown that an MLC can be incorporated into a linac-MRI system.

3.8 References

Balanis C. “Antenna theory: analysis and design” John Wiley and Sons, New York 2005.

Bortfield T. “IMRT: a review and preview” Phys. Med. Biol. **51** R363-R379 2006.

Burke B., Lamey M., Rathee S., Murray B. and Fallone B.G. “Radio frequency noise from clinical linear accelerators” Phys. Med. Biol. **54** 2483-2492 2009.

Chen H., Wu A., Brandner E.D., Heron D.E., Huq M.S., Yue N.J. and Chen W-C. “Dosimetric evaluations of the interplay effect in respiratory-gated intensity modulated radiation therapy” Med. Phys. **36** 893-903 2009.

Dempsey J., Dionne B., Fitzsimmons J., Haghigat A., Li J., Low D., Mutic S., Palta J., Romeijn H., and Sjoden G. “A real-time MRI guided external beam radiotherapy delivery system” Med. Phys. **33** 2254 2006.

Fallone B.G., Murray B., Rathee S., Stanescu T., Steciw S., Vidokovic S., Blosser E. and Tymofichuk D. “First MR images obtained during megavoltage photon irradiation from a prototype linac-MR system” Med. Phys. **36** 2084-2088 2009.

Holm R. “Theory of sparking during commutation on dynamos” Conf. Record-AIEE IAS Annual Meeting pp 588-595 1962.

Jabbar M.A. “Radio frequency interference of electric motors and associated electronics” *IEEE trans. Ind. Appl.* **27** 27-31 1991.

Kirkby C., Stanescu T., Rathee S., Carlone M., Murray B. and Fallone B.G. “Patient dosimetry for hybrid MRI-radiotherapy systems” *Med. Phys.* **35(3)**

1019-1027 2007.

Lagendijk J.J.W., Raaymakers B.W., Raaijmakers A.J.E., Overweg J., Brown K.J., Kerkhof E.M., van der Put R.W., Hårdemark., van Vulpen M. and van der Heide U.A. “MRI/linac integration” Radiother. Oncol. **86** 25-29 2008.

Langden K. and Jones D. “Organ motion and its management” Int. J. Rad. Oncol. Biol. Phys. **50** 265-278 2001.

Nill S., Unkelbach J., Dietrich L. and Oelfke U. “Online correction for respiratory motion: evaluation of two different imaging geometries” Phys. Med. Biol. **50** 4087-4096 2005.

Padmanabhan A. and Srinivsan A. “Some important aspects in the phenomenon of commutator sparking” IEEE Trans. **PAS 84** 396-404 1965.

Rietzel E., Rosenthal S.J., Gierga D.P., Willet C.G., Chen G.T. “Moving Targets: Detection and Tracking of Internal Organ Motion for Treatment Planning and Patient Set-up” Radiother. Oncol. **73** S68-S72 2004.

Sawant A., Venkat R., Srivastava V., Carlson D., Povzner S., Cattell H. and Keall P. “Management of three-dimensional intrafraction motion through real-time DMLC tracking” Med. Phys. **35** (5) 2050-2061 2008.

Stratton J. A. “Electromagnetic theory” McGraw Hill, New York pp 457 2007.

Suriano C.R., Suriano J.R., Thiele G., Holmes T.W. “Prediction of radiated emissions from DC motors” *IEEE* Syp. Elec. Comp. **2** 790-795 1998.

Suriano J. R. “Modeling of electromechanical and electromagnetic disturbances in DC motors” IEEE Nat. Symp. Elect. Comp. Denver 258-262 1989.

Webb S. and Bortfeld T. “A new way of adapting IMRT delivery fraction-by-fraction to cater for variable intrafraction motion” Phys. Med. Biol. **53** 5177-5191 2008.

Webb S. “Quantification of the fluence error in the motion-compensated dynamic MLC (DMLC) technique for delivering intensity-modulated radiotherapy (IMRT)” Phys. Med. Biol. **51** L17-L21 2006a.

Webb S. “Motion effects in (intensity modulated) radiation therapy: a review” Phys. Med. Biol. **51** R403-R425 2006b.

Webb S. “The effect on IMRT conformality of elastic tissue movement and a practical suggestion for movement compensation via the modified dynamic multileaf collimator (dMLC) technique” Phys. Med. Biol. **50** 1163-1190 2005.

Weiner M. M. “Monopole Antennas” Marcel Dekker Inc., New York 2003.

Valentine R. “Motor Control Electronics Handbook” McGraw Hill, New York 1998.

van Herk M. “Errors and Margins in Radiotherapy” Sem. Rad. Oncol. **14** 52-64 2004.

Verellen D., De Ridder M. and Storme G. “A (short) history of image-guided radiotherapy” Radiother. Oncol. **86** 4-13 2008.

Chapter 4: Studies on the RF Noise Production from the Modulator of a Linac

A paper which is related to the work presented in this chapter has been published: B Burke, M Lamey, S Rathee, B Murray and B G Fallone "Radio frequency noise from clinical linear accelerators" Phys. Med. Biol. 54 No 8 (21 April 2009) 2483-2492.
A second paper which is based on the results presented herein has been submitted to the journal IEEE transactions on electromagnetic compatibility: M. Lamey, S Rathee, L. Johnson, M. Carlone, E Blosser and G. Fallone "Radio Frequency Noise from the Modulator of a Linac" Submitted to IEEE trans. Elect. Comp.

4.1 Introduction

This chapter focuses on the determination of the sources of broadband RF noise within the modulator of a linac. The modulator produces the pulsed high voltages that are required for the electron gun and the microwave power source of the linac. Two distinct software programs were used in the studies presented in this chapter. MultiSIM (National Instruments, Austin, Texas, USA) is based on SPICE (simulation program with integrated circuit emphasis) and was used to model the charge and discharge of the pulse forming network (PFN) within the modulator. The PFN circuit produces a high voltage pulse of desired shape and duration for the microwave source. COMSOL Multiphysics (COMSOL, Stockholm, Sweden) uses the finite element technique to solve physical problems; the program was used to determine the fields near the long PFN coil within the modulator. The ~ 3 GHz power source of the modulator studied was a magnetron, which is the typical microwave oscillator used for lower energy medical linacs.

4.2 Theory

4.2.1 SPICE Theory

SPICE is a software program which uses numerical techniques to simulate the response of electronic circuits at the device level. Specifically the program solves a network of equations for the voltages at nodes in the circuit. Analysis options are: non-linear DC, nonlinear transient and linear AC.

The DC analysis solver computes the so-called operating point of the circuit by treating inductors as shorts and capacitors as open circuits.

The AC analysis package uses a steady-state sinusoidal input to determine the complex values of the node voltages as a function of input frequency for a linear circuit.

The transient analysis routine determines the voltage at nodes in the circuit as a function of time. Numerical integration removes the time dependence of the response of certain components, such as capacitors and inductors (i.e. the voltage across an inductor $V = LdI / dt$ where I is the current and t the time). Iterative techniques are used to solve for non-linear components such as diodes. The transient analysis routine was used to solve the circuits of the modulator of a linac. The operating principles of the SPICE simulator are given in Appendix D.

SPICE can be described by a multistep process:

- Draw an equivalent circuit with each node numbered uniquely; this includes connections from one component to the next.
- Label each component and give it the appropriate value and initial condition (if any).

- Run the analysis type you wish to perform (DC, AC or transient).
- View the results using the graphics editors provided (for this work the MultiSIM GUI was used which includes graphics software).

A through introduction to SPICE is given in Appendix D.

4.2.2 Finite Element Method

The finite element method is a numerical technique which discretizes the solution of differential equations. The concept behind the method is that a continuous function can be approximated by a set of piecewise elements. The piecewise elements are defined at specific points along the continuous function. The process is as follows: a finite number of points (or nodes) in a specified domain are chosen, and the actual values of the continuous function at the nodal points are the variables that must be determined. The domain is broken into subdomains, termed elements, which are connected at nodal points. The continuous function is approximated by a polynomial which itself is determined by the values of the function at the nodal points. The mathematical process follows the procedure: discretize the domain, select the interpolation functions, formulate the system of equations and solve the system of equations. The theoretical approach described here closely follows Jin [Jin 2002] with an emphasis on the COMSOL package.

4.2.2.1 Discretization of the Domain

The domain for which the solution is desired is broken into a finite number of elements. Typical elements used in one, two and three dimensional systems are shown in Figure 4.1. Generally in two or three dimensions the geometry of the problem suggests which type of element to use. For example, rectangular elements are best suited for rectangular domains. An example of a meshed problem is shown in Figure 4.2. In Figure 4.2 the mesh near six of the PFN coil loops is displayed. Near curved or sharp surfaces a greater density of elements is required to faithfully reproduce the geometry and therefore the correct field distribution.

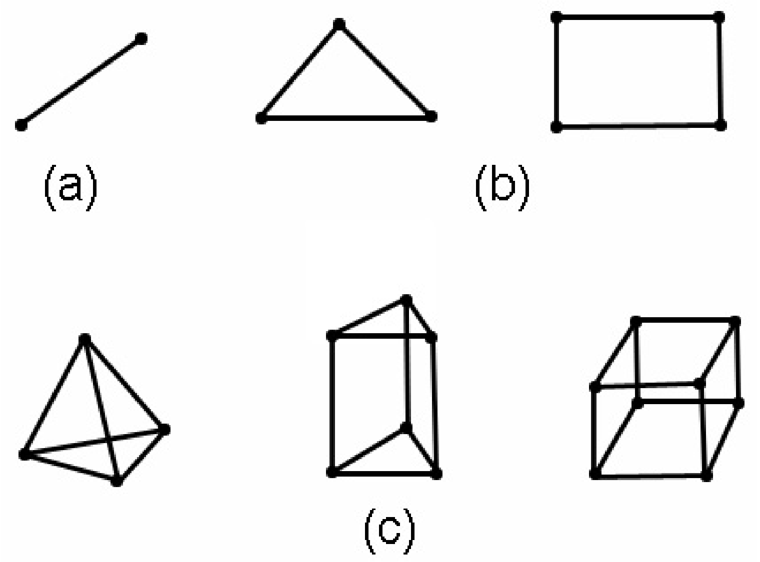

Figure 4.1: Basic finite elements in one-dimension (a), two-dimensions (b) and three-dimensions (c).

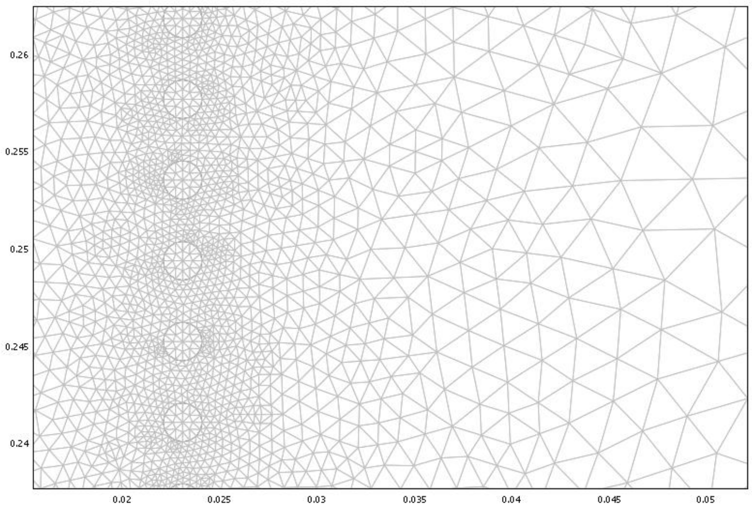

Figure 4.2: An example of a meshed problem showing six of the PFN coil loops and the triangular mesh near these loops.

As described previously the solution to a continuous function is defined at the nodes of an element. It is necessary to formulate a complete description of a node within the domain, this includes: the coordinate values, a local number and a global number. The local number specifies its position within the element and the global number specifies its position within the domain. Referring to Figure 4.2 the domain is the complete region of interest, the elements are the many triangular pieces dividing the domain and nodes occur at the ends of the triangular elements.

4.2.2.2 Selection of Interpolation Functions

Interpolation functions within an element are selected which approximate the solution at non-node positions. In two dimensions the interpolation function can be linear, quadratic, cubic, quartic or quintic.

In order to define curved spaces generally isoparametric elements are used. An isoparametric element is an element whose interpolation function is the same order as the mapping function. The mapping function is used to map from an original element to a deformed element, an example is shown in Figure 4.1. Isoparametric elements are based upon those shown in Figure 4.1, but the sides of which can be curved. An example isoparametric element is shown in Figure 4.3

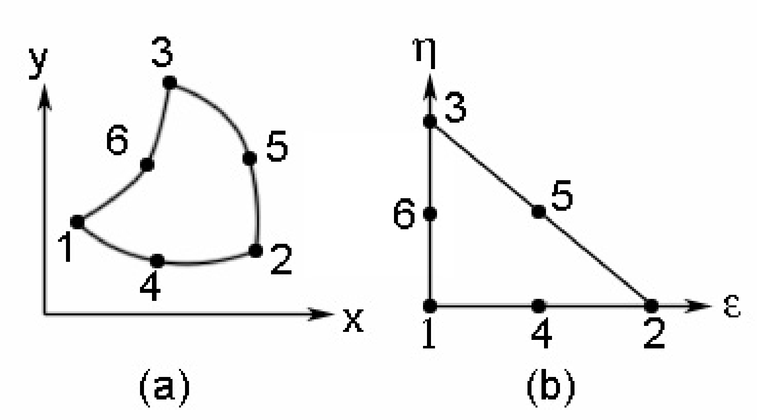

Figure 4.3: Introduction to the isoparametric element: the triangular element with curved sides (a) can be mapped to a simple triangular element (b).

The element in Figure 4.3(a) can be mapped from a simple triangular element using a quadratic transformation.

4.2.2.3 Formulation of the System of Equations

COMSOL uses a formulation based on Galerkin's method, which is a method of discretizing a continuous problem. A more detailed theoretical approach is given in [Sokolnikoff 1956, Brenner 2005 and Ciarlet 1978]. For a problem of the form:

$$D\varphi = f \qquad (4.1)$$

where D is a differential function, φ is the solution and f is an excitation or forcing function. Galerkin's method states that the substitution of an approximate solution, φ', into Equation (4.1) will in general lead to a non-zero residual *r*. The best estimate of the unknown φ is determined by minimizing the residual, e.g. by minimizing the square of $D\varphi - D\varphi'$.

4.2.2.4 Solution of the System of Equations

A finite element problem will have one of two forms, that of Equation (4.1) or:

$$[A]\{\varphi\}=\lambda[B]\{\varphi\} \tag{4.2}$$

where the notation [A] represents a matrix A. Problems resulting from either an inhomogeneous boundary condition or an inhomogeneous differential equation lead to an equation of the type shown in Equation (4.1). These types of systems are known as deterministic. Problems governed by either homogeneous boundary conditions or homogeneous differential equations lead to the type of equation shown in (4.2) and are known as eigenvalue equations. In electromagnetics systems which include a source or some type of excitation are deterministic; examples are problems with radiation or scattering. Source-free problems are associated with eigenvalue systems; examples include wave propagation in wave guides or resonance in cavities.

Solvers in COMSOL include both direct and indirect. The direct solver PARDISO was implemented in this work. The direct solver PARDISO [Schenk et al. 2000] is a sparse matrix solver suitable for parallel use on computers. Other solvers include UMFPACK [Davis 2004a, Davis 2004b, Davis 1999 and Davis 1997], SPOOLES [Ashcraft 1999], TAUCS [Toledo et al. 2009], GMRES [Saad

1986] and Conjugate gradients [Hestenes et al.1954].

Once an estimation to the solution is obtained COMSOL has post processing tools which enables the user to view the solution in a multitude of different plots.

4.2.3 Saturable Reactor

A saturable reactor (SR) is a non-linear magnetic control device. A ferromagnetic material has the property that the relationship between the B field and the magnetizing force (H) is not linear. When an H field is applied to a magnetic material and the resulting flux density is plotted, the shape takes the form of a hysteresis loop; as shown in Figure.4.4.

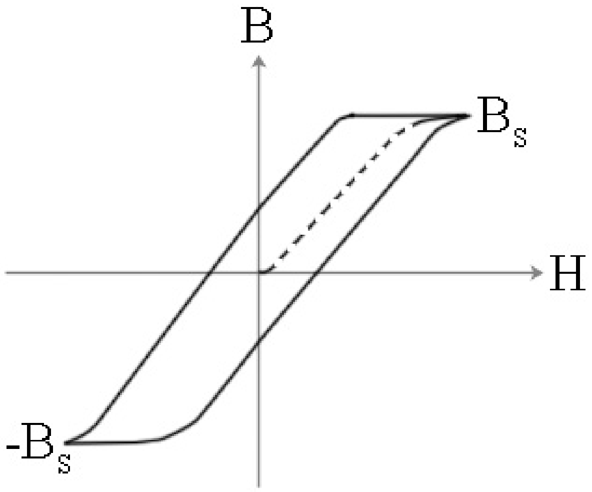

Figure 4.4: General hysteresis loop of a ferromagnetic sample.

The small-signal inductance of a winding around a ferromagnetic material changes as we move along the hysteresis loop. The inductance of a winding given a core cross sectional area A_{Fe} and magnetic path length l_{Fe} (the magnetic path length is the ratio of the product of the ampere-turns to the average magnetizing force) is given by Geyger [Geyger 1964]:

$$L = 4\pi \frac{A_{Fe}}{l_{Fe}} N^2 \left| \frac{dB}{dH} \right| \ (10^{-8}\, henrys). \tag{4.3}$$

From Equation 4.29 we can see that the inductance of a winding depends on the slope of the hysteresis loop.

A SR consists of three elements; a DC current source, a magnetic core with windings and an AC source. The operation of a SR is based upon the principle that the current through a winding, around a magnetic core, can be made to vary depending on the saturation of the core. In essence a SR is a device whose inductance can be made to vary by the application of a DC bias. A simple saturable reactor is shown in Figure 4.5.

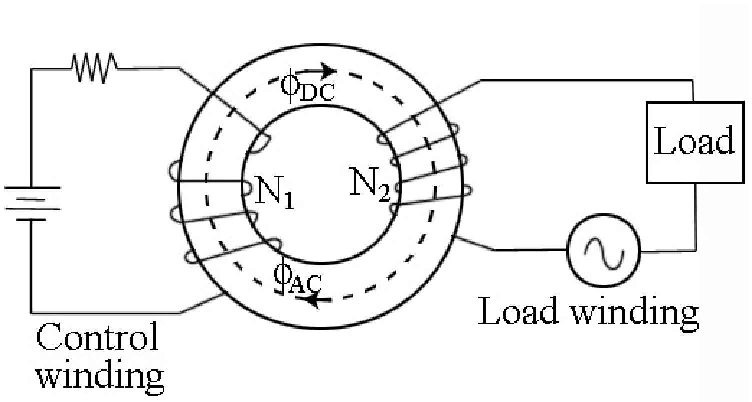

Figure 4.5: Basic saturable reactor consisting of a DC current source a magnetic core and an AC source.

The DC bias results in a magnetic flux in the magnetic core; as shown in Figure 4.5 (ϕ_{DC}). The AC source will produce a flux within the core which will constantly change in magnitude and direction. The AC source will continuously change the impedance of the core by driving the core near, into or out of saturation. Consider the ideal hysteresis loop of Figure 4.6. If the DC bias is set so that the flux through the core is at point x, the AC source will either drive the core further into saturation or out of saturation. When the core is saturated the windings will act as a small inductance to an external circuit (the same which would be seen for an air core), however, when the core is not saturated the windings will act as a much larger inductance. In this work the SR's were biased at point x, shown in Figure 4.6.

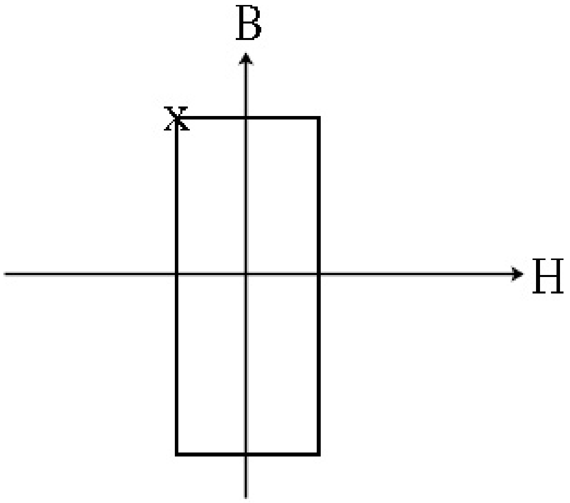

Figure 4.6: Ideal B-H hysteresis loop. Starting from the position labeled "x", if we proceed to the right we will see a small inductance, however, if we move down we see a large inductance.

4.2.4 Mechanism of Magnetron RF Noise Production

A cross sectional view of a magnetron is shown in Figure 4.7. A magnetron is a crossed *E* and *B* field device. A magnetron consists of a central cathode concentric to an outer anode. During operation a *B* field will be applied perpendicular to the *E* field between the cathode and anode (E_E). A heated filament located at the cathode structure provides a source of electrons. In these crossed fields the electron trajectories will be curved as shown in Figure 4.7. The

B field is static while the *E* field is applied in a pulsed manner (at least for the magnetrons used to produce radiation in clinical environments). The pulse has associated rise and fall times and is applied to the cathode. As the negative voltage on the cathode is increased in magnitude, the electron trajectories curl closer to the anode. The velocities of the electrons also increase as the magnitude of the negative cathode voltage increases. The electrons induce charge on the anode as they pass by; the frequency of the induced currents is related to the velocity of the electrons. The charge on the anode results in an induced microwave field (E_m) at and within the cavities. Approximately 60 % of the electrons kinetic energy is converted into microwave energy.

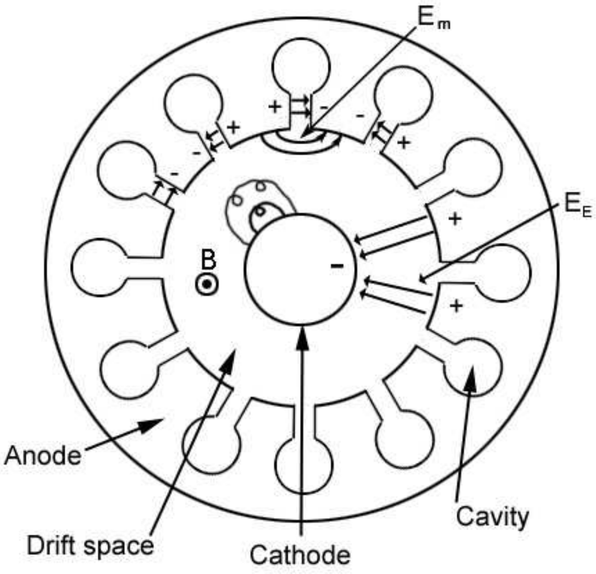

Figure 4.7: Cross sectional view of a magnetron illustration the geometrical arrangement of the cathode and anode.

A magnetron is known to be a source of broadband RF noise [Okress 1961, Collins 1948 and Little 1958]. Neculaes [Neculaes et al. 2003] states "…noise generation mechanisms in crossed-field devices are not presently understood and predictive computational calculations do not exist. Methods of noise suppression in crossed-field devices have not presently been practically realized".

Numerical simulations of magnetrons have been performed, Yu [Yu et al. 1965] states that "The operation of these devices is on the border line between order and disorder, and is also completely non-linear, so that a computer is likely to remain the only instrument for a reliable description". More recent studies by Monossov [Monossov 1999] illustrates that further work is required to reproduce a complete 3D model of the electron interaction process in these devices.

4.2.5 Charging Circuit of the Modulator

Consider the circuit shown in Figure 4.8; a DC voltage is used to charge a network of capacitors, which are represented by the capacitance C_N, while L_C and R_C represent the inductance and resistance in the charging circuit.

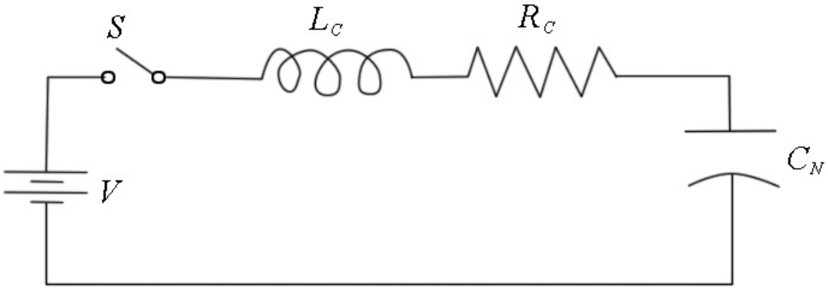

Figure 4.8 Simplified charging circuit in the modulator of a linac.

The modulator of a linac uses a power supply to charge the network of capacitors to a voltage between V and $2V$. Assuming that the energy stored in the inductor is completely transferred to the capacitor, that there is some initial voltage, $v_N(0)$, on the capacitance C_N and that R_C is very small or approximately zero, then to satisfy the law of conservation of energy we have:

$$q_N V = \frac{C_N}{2}\left(v_N(t)^2 - v_N(0)^2\right) \tag{4.4}$$

where q_N is the charge transferred to the capacitance at time t. We have assumed that an energy $q_N V/2$ has been stored and then transferred from the inductor to the capacitor. This energy adds to the energy $q_N V/2$ from the battery to the capacitor to get the left hand side of Equation 4.4. But the electric charge must satisfy:

$$q_N = C_N\left[v_N(T) - v_N(0)\right]. \tag{4.5}$$

Where T is the instant in time at which the inductor has transferred all of its energy to the capacitor. Therefore, by substituting C_N from Equation 4.5 into Equation 4.4,

$$q_N V = \frac{q_N}{2}\left[v_N(T) + v_N(0)\right] \tag{4.6}$$

or:

$$v_N(T) = 2V - v_N(0). \tag{4.7}$$

If there is no initial voltage on the capacitance then the capacitors will smoothly charge up to, and momentarily be, twice the voltage of the DC power supply.

Consider the application of the addition of a diode D, and a DeQ'ing network (S2 and R1) as shown in Figure 4.9.

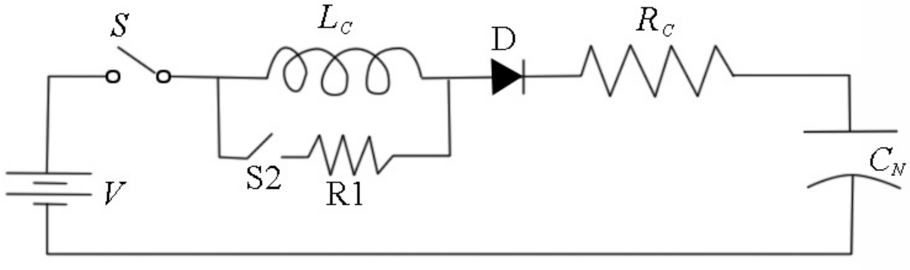

Figure 4.9: Charging circuit with the addition of a deQ'ing network and a diode.

If the capacitor network starts with zero initial charge, then once the switch *S* is closed the capacitor network will charge up to the voltage *V*. During this process the inductor will also store energy. As the rate of current through the inductor slows, due to an accumulated charge on the capacitor bank, the field in the inductor will begin to collapse and this energy will be transferred to the capacitor network. The capacitors begin to sinusoidally charge from *V* up toward 2*V*. During this energy transfer consider the act of closing the switch S2, this act dissipates the stored energy in the inductor into the resistor R1. The act of closing the switch S2 cuts the flow of stored energy from the inductor to the capacitor. The switch S2 can be used to select the voltage, between *V* and 2*V*, to charge the capacitor network. The Diode, D, blocks the stored charge on the capacitor network from reversing back to the supply.

4.2.6 The Modulator and Magnetron

Figure 4.10 illustrates the relationship between the major components in the modulator of a linac including the magnetron. The power supply charges the capacitors C1 - C6 to a voltage set by the De-Q circuit. When the thyratron, which acts as a switch in the circuit, is triggered the stored charge in the PFN is transferred to the load through a transformer. The transformer is used for impedance matching and to step-up the voltage on the load. The load (either a magnetron or klystron) is used to generate or magnify microwave power.

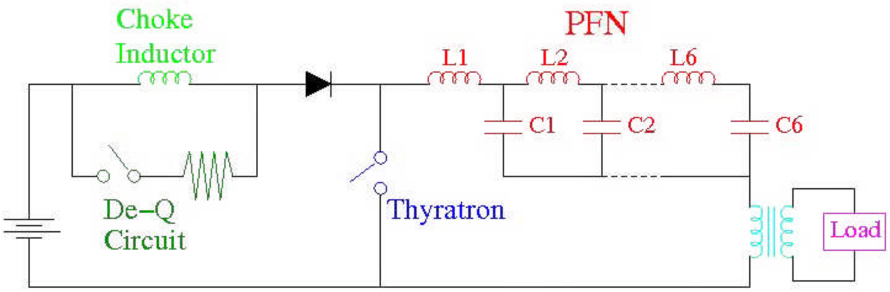

Figure 4.10: The major components in the modulator of a linac including the load (a magnetron was used in this work).

4.2.7 Pulse Forming Network Model

A modulator produces voltage pulses of about 5 μs duration using the PFN. A PFN consists of a bank of capacitors and a large helical coil tapped at regular intervals. The purpose of the PFN is to store the amount of energy needed in a single pulse and to discharge this energy into a load in the form of a pulse of usable shape. When modeling the PFN, the coil is treated as a discrete set of coupled inductances as shown in Figure 4.11 [Torok 1994 and Glasoe et al. 1964].

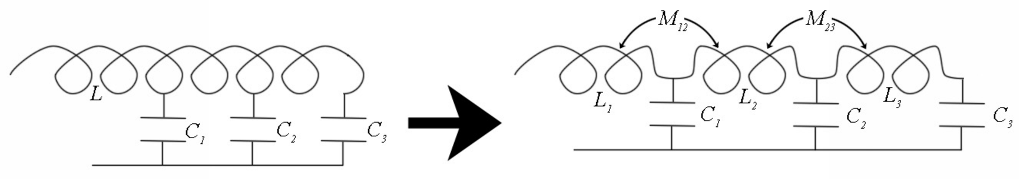

Figure 4.11: The representation of a PFN in an electronic circuit. On the left is the actual PFN setup, on the right is the electrical model illustrating that the coil consists of multiple inductors with mutual coupling.

The inductance of each section of the PFN coil was calculated by measuring the radius of the coil (a), the axial length (c) and the number of turns (N) and using the equation for the inductance of a coil given by Miller [Miller 1987] (Lorenz [Lorentz 1879] was the first to derive the exact expression, the expression given by Miller is conveniently in SI units).

$$L = \left(\frac{\mu N^2 \pi a^2}{c} \right) K \tag{4.8}$$

where:

$$K = \frac{1}{3\pi} \left[\left(\frac{dc}{a^2} \right) \left(F(k) - E(k) \right) + \frac{4d}{c} E(k) - \frac{8a}{c} \right] \tag{4.9}$$

F(k) and *E(k)* are the complete elliptic integrals of the first and second kind respectively, μ is the permeability of vacuum and $d = (4a^2 + c^2)^{1/2}$. The mutual inductance (M_{12}) between adjacent coils was calculated using a formula given in Rosa [Rosa et al. 1912]. For two separate coils of the same radius, number of turns per unit length and in contact the mutual inductance between the two can be calculated using:

$$2M_{12} = L_{12} - \left(L_1 + L_2 \right) \tag{4.10}$$

where L_{12} is the inductance if coils 1 and 2 were considered one and L_1 and L_2 are the inductances of coils 1 and 2 respectively.

4.2.8 Thyratron Model

A thyratron consists of a gas filled tube with a control grid between an anode and cathode. When the potential of the control grid has sufficient positive bias, compared to the cathode, gas is ionized and current can flow. The thyratron was modeled as a unidirectional switch (a diode and switch combination) with a small resistance and turn-on potential. Goldberg [Goldberg 1962] states that a hydrogen thyratron has a turn-on potential of approximately 50 V. After equilibrium is reached and the thyratron is conducting current, it has an equivalent impedance of approximately 1 Ω [Glasoe et al. 1964]. During turn-on the impedance is much higher; however this larger impedance only lasts up to 0.1 µsec [Glasoe et al. 1964] and therefore was not modeled. While the thyratron was not conducting the impedance in its model was infinite.

4.2.9 Transformer Model

The transformer model followed those used in the literature [Hill 1962, Brown et al. 1992 and Jang et al. 2004]. The equivalent circuit of a 1:1 transformer is shown in Figure 4.12.

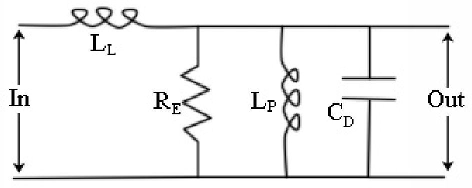

Figure 4.12: Equivalent circuit model of a 1:1 transformer including the leakage inductance (L_L), a core resistance (R_E), a primary inductance (L_P) and a distributed capacitance (C_D).

In the simulation an ideal 4:1 step up transformer was added to the model shown in Figure 4.12. For the transformer used in this work the distributed capacitance, leakage inductance and primary inductance approximate values were taken from the Varian transformer specification sheet [Varian Transformer spec.]. The values used in the work were 33 mH, 14 µH and 16 pF for the primary inductance, leakage inductance and distributed capacitance respectively.

4.2.10 Magnetron Model

An equivalent circuit for a magnetron is given in [Varian course book 1989] and is shown in Figure 4.13. The model consists of a series combination of an equivalent resistance (400 Ω), a diode and a DC bias with an equivalent capacitance in parallel.

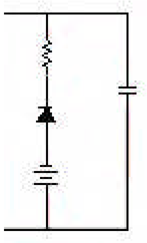

Figure 4.13: Equivalent circuit of a magnetron used in this work.

The diode is necessary to mimic the unidirectional behavior of the magnetron, the electrons only flow from the cathode to the anode. The DC bias emulates the turn-on potential; a certain voltage across the magnetron is required before it will start to conduct. The capacitance was determined by measuring the values of the capacitors placed across the magnetron. The DC bias was set using the knowledge that no conduction occurs until the applied voltage nearly reaches the DC voltage (the flattop of the high voltage pulse from the PFN) [Varian course book 1989].

4.2.11 De-spiking Network

A de-spiking RC series network is placed across the primary of the transformer for impedance matching. The magnetron will not conduct until a bias of several kV is applied across the anode and cathode. A large input impedance is therefore presented at the start of discharge to the PFN through the transformer by the magnetron load. The instantaneous input impedance, z_T, which the transformer presents to a unit voltage before the magnetron starts to oscillate, can be approximated as [Glasoe et al. 1964]:

$$z_T = \sqrt{\frac{L_L}{C_D}} \csc\left(\frac{t}{\sqrt{L_L C_D}} \right) \tag{4.11}$$

where L_L and C_D are the leakage inductance and distributed capacitance of the transformer respectively. If a unit voltage is applied to a series RC network the instantaneous impedance presented as a function of time is:

$$z_{RC} = \mathrm{R}e^{t/RC}\,. \tag{4.12}$$

Consider the application of connecting an RC de-spiking network in parallel with the approximated transformer load, the equivalent impedance, z_{eq}, seen is:

$$\frac{1}{z_{eq}} = \frac{1}{z_{RC}} + \frac{1}{z_T}\,. \tag{4.13}$$

A plot of equations 4.11, 4.12 and 4.13 clearly illustrates the need for the de-spiking network. The impedances can be normalized to the PFN impedance, Z_N, for which we assume $Z_N = \sqrt{L_L / C_D} = R$ and $\sqrt{L_L C_D} = \pi/(4RC)$. A plot of the normalized impedances of the transformer, RC network and a parallel combination of the transformer and network is shown in Figure 4.14.

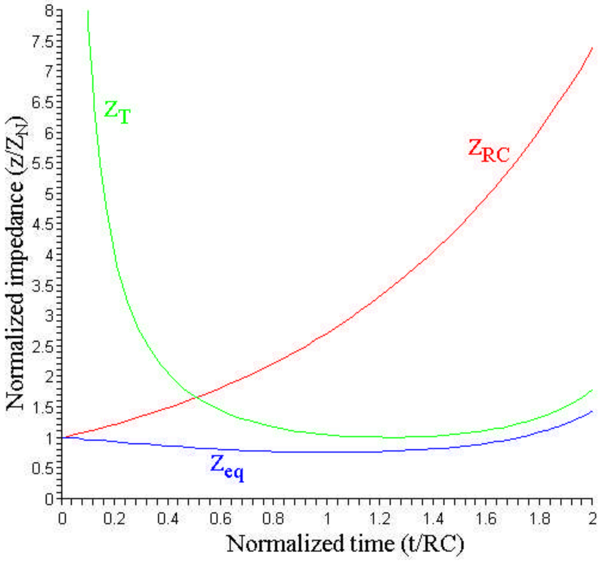

Figure 4.14: Normalized instantaneous impedance of a transformer, RC network and parallel combination of a transformer and RC network. Z_N is the impedance of the PFN.

Figure 4.14 illustrates the input impedance of the transformer on the primary side. The Figure illustrates the necessity of an RC network across the transformer. Without the RC network the input impedance at small times, with respect to the time it takes the magnetron to build up to oscillation, of the transformer is very large. This large impedance leads to a voltage spike due to a mismatch in impedances between the PFN and transformer. The addition of an RC network closely matches the equivalent impedance (i.e. $z/Z_N=1$) seen by the PFN before the magnetron starts to conduct. Without the RC-network the input impedance is large (green curve, Z_T in Figure 4.14). With the addition of the RC-network the input impedance closely matches that of the PFN (blue curve, Z_{eq} in Figure 4.14).

4.3 Materials

4.3.1 RF Measurements

The RF noise inside clinical vaults and near the modulator was measured using the Rohde and Schwarz near field probe set which are described in Appendix A, section A.2.

4.3.2 Linac Subsystems

A medical linac is comprised of several subsystems which are shown in Figure 4.15. The work herein is focused on the modulator, which is the source of the pulsed power used to drive the linac. The following is a brief description of the subsystems shown in Figure 4.15.

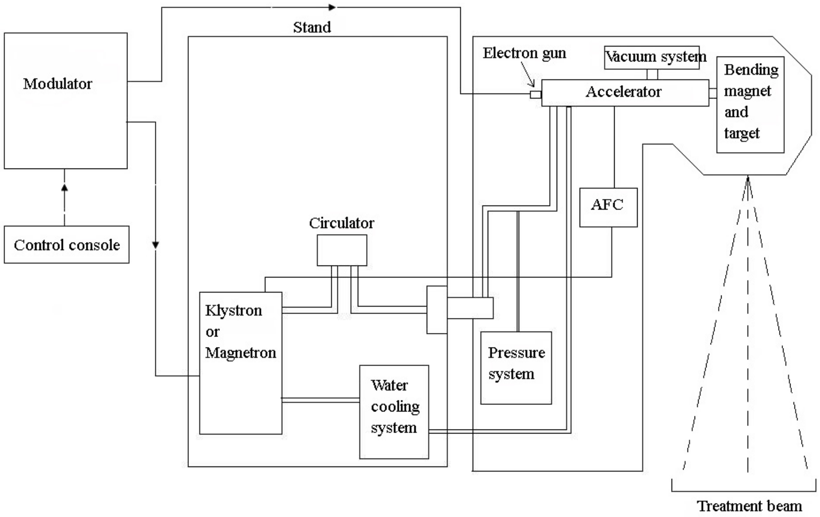

Figure 4.15: Block diagram of the major subsystems in a general medical linac illustrating the interplay between these elements. The linac in our system does not include a bending magnet.

4.3.2.1 Accelerating Structure

The accelerating structure, or accelerating waveguide, is a structure which consists of a series of cylindrical shaped cavities that resonate in a TM_{01} mode such that the electric field is parallel to the axis of the cavity. When microwaves are injected into the structure at its resonant frequency, an accelerating voltage is created along the waveguide's axis which can accelerate electrons to megavoltage energies. The electron's energy is converted to photon energy when the electrons impinge on a high Z target, and are stopped by the Bremsstrahlung process. To achieve a sufficiently large accelerating gradient, high power microwaves are necessary. This microwave power is produced by a klystron amplifier or a magnetron oscillator, which operate by converting a high voltage pulsed input into high power microwaves.

4.3.2.2 Klystron

The klystron is a two element device consisting of a cathode and an anode. The short pulse from the modulator is used to accelerate electrons away from the cathode of the klystron. The electrons enter a buncher resonance cavity which is energized by low power microwaves. These low power microwaves setup electric fields which alternate in time. Electrons which arrive early in the microwave cycle are slowed, electrons arriving in phase with the microwave cycle are unaffected and electrons which arrive late are accelerated, this process bunches the electrons. The electron bunch formations traverse further resonant cavities (which improve the electron bunching) and drift tubes before entering a catcher cavity. The electrons induce charge at the end of the catcher cavity thereby producing retarding electric fields. During this process much of the kinetic energy of the electrons is converted into the creation of intense electric fields. These fields are used to power the accelerator structure. The high power generation is also based upon the large shunt impedance associated with the catcher cavity which results in the induction of large voltages. Each of the cavities of a klystron have tuning adjustments, these adjustments are necessary so that the RF power generated is matched to the accelerator structures optimum operating frequency. The frequency adjustments are made by slightly modifying the cavity dimensions. A klystron is an amplifier, and amplifies a small (~ 50 W) microwave input with a gain of 10^5 to produce mega watt microwaves.

4.3.2.3 Magnetron

Unlike a klystron which is an amplifier of microwave power, a magnetron produces microwaves by self-oscillation. As shown in Figure 4.7 a magnetron consists of a cylindrically shaped cathode surrounded concentrically by a cylindrically shaped anode. Typically the anode consists of twelve cavities which open up into the evacuated space between the anode and cathode.

A magnetic field is applied along the axis of the cylindrical geometry (into the page in Figure 4.7 and perpendicular to the electric field between the cathode and anode). The pulse from the PFN is sent to the cathode and accelerates electrons toward the anode. Due to the crossed electric and magnetic fields the electrons follow a path which brings them close to the anode thereby inducing charge on the anode. This induced charge sets up electric fields between adjacent cavity segments of the anode. By generating these electric fields kinetic energy from the electrons is converted into microwave energy which is used to power the accelerator structure.

4.3.2.4 Modulator Cabinet

The modulator cabinet converts the energy from a DC power supply to provide a negative pulse of voltage to the cathode of either the klystron or magnetron, and a negative voltage pulse to the cathode of the electron gun attached to the accelerating waveguide. The pulse is approximately 5 μs long and repeated approximately every 1.5 ms (duty factor of 0.003). The modulator cabinet and the components within it are the focus of this chapter.

The modulator consists of a charging circuit which is responsible for charging the capacitors in the PFN, the PFN which consists of a bank of capacitors connected in parallel through a large coil, a thyratron which consists of a gas filled tube with control grids between the anode and cathode and a de-spiking network which is designed to minimize the voltage spike at the start of energy transfer from the PFN into the magnetron. More details on these components were given in Sections 4.2.5 to 4.2.11.

4.3.2.5 Other Components and Systems

The circulator is a device which is used to isolate the klystron, or magnetron, from microwave power reflected back from the accelerator structure. It also is used to detect the reflected RF power which is used by the automatic frequency control (AFC) system.

The cooling water system is used to stabilize the temperature of the accelerator structure and to cool any components which dissipate energy as heat.

If a bending magnet is utilized, its purpose is to deflect the electron beam in a loop and focus the beam onto a target to produce x-rays or onto scattering foils to produce a broad electron beam. In our linac-MRI system there is no bending magnet.

The treatment head contains beam shaping components such as a flattening filter, field defining "jaws" and a multileaf collimator. The treatment head also houses the beam monitoring devices such as the ion chambers which are used to ensure the prescribed dose is delivered to the patient.

An AFC system is used to measure the optimum operating frequency of the accelerator structure in order to maximize the radiation output. The klystron or magnetron is then tuned to this optimum frequency.

4.4 Methods

4.4.1 RF Noise Measurements from Clinical Linear Accelerators

The RF noise was measured inside several vaults while the linac produced radiation. The setup used for the measurements is shown in Figure 4.16. The E and H fields produced by the modulator were measured using a near field HZ-11 probe set (Rohde and Schwarz, Munich, Germany). The E probe measures the total E field strength while the H probe was used to measure the three individual orthogonal components of the H field strength; these three orthogonal Cartesian components were added in quadrature to obtain the total H field strength (The probes are described in detail in Appendix A). The measured data from E and H

probes was transferred from the oscilloscope to a PC using a Keithley KUSB 488 GPIB interface (Keithley Instruments Inc, Cleveland, OH). The software program DADiSP (DSP Development Corporation, Newton, MA) was used for offline data analysis. DADiSP was used to calculate the discrete Fourier transforms (DFT) of the measured waveforms. The resulting DFTs had bin widths of 50 kHz in the frequency domain. The final frequency spectra, *S(f)*, of the *E* and *H* fields were separately calculated as in Equation 3.1. The frequency spectrum was estimated from 1000 time domain measurements. The approximate power spectral density of the RF noise was then calculated using Equation 3.3.

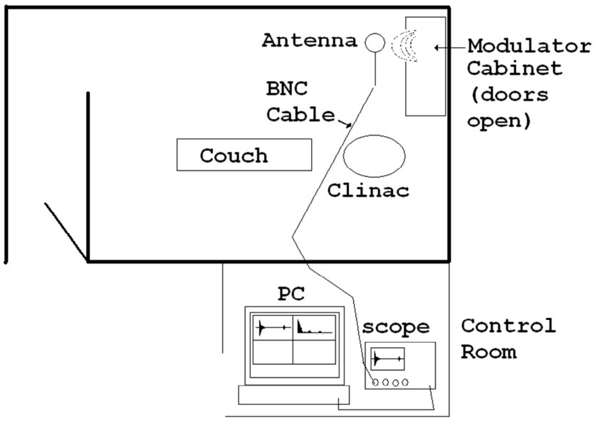

Figure 4.16: Simplified setup used to measure the RF noise from a clinical linac.

4.4.2 Modulator Simulation

A refurbished modulator of a 6 MV linac was used to study the sources of RF noise. A schematic of the modulator simulation is shown in Figure 4.17. The simulation was complete up to, and included the magnetron; on the physical unit the microwave power produced by the magnetron was dissipated into an EM designed water load (EM design, Medford Oregon, model R284B-3). The main components of the modulator consisted of a three phase power supply a large choke inductor and de-Q circuit, a PFN with a Hipotronics (Hipotronics Inc., Brewester New York, MASF-1357-A314) capacitor bank of 10 nF capacitors, an E2V (E2V technologies, Chelmsford, England) CX 1140L thyratron and an E2V MG5193 magnetron.

After the capacitors (C1 - C6) have been discharged through the thyratron and pulse transformer into the magnetron, charge from the approximately 13 kV power supply flows through the large inductor L8 and begins to charge the capacitors. Initially the reactance of L8 will limit the current flow resulting in a voltage drop nearly equal to that of the battery appearing across L8 (some appear across small resistances). As time passes current begins to flow resulting in the storage of energy in the core of L8. As the potential across the capacitors builds up, the current flow begins to decrease as the difference between the battery and the capacitors decreases. As the charging current from the power supply begins to diminish the magnetic field in L8 begins to collapse. By Faradays law of induction the collapsing field induces an EMF in the coil which acts as a source in series with the power supply. This additional source produces a continuation of current flow in L8, which can charge the capacitors up to or near twice the voltage of the battery.

Consider now the circuit R8 and J1 (a voltage controlled switch). If the switch, J1, is closed sometime after the current in L8 has reached a maximum (same time the capacitors reach the battery potential) the stored energy in L8 will be routed through J1 and dissipated in the resistance R8. Depending on when the switch J1 is closed, the potential across the capacitors (C1-C6) can be set anywhere from the supply voltage to twice the supply voltage.

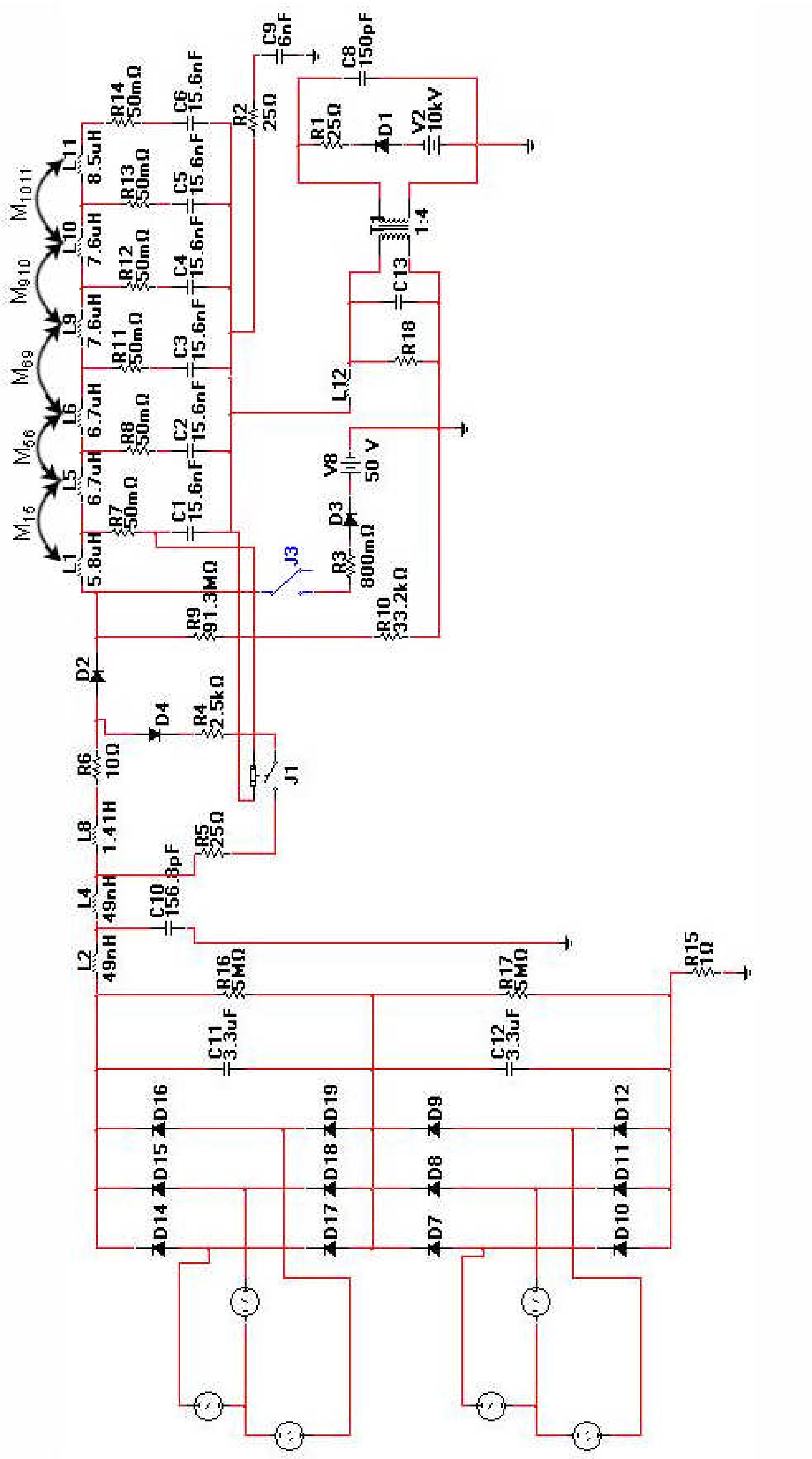

Figure 4.17: Simulation layout of the modulator and magnetron of a linac.

As described previously the PFN consists of a bank of capacitors connected in parallel through a large coil, represented by the lumped inductors. In Figure 4.17 the capacitors are labeled C1 - C6 and the PFN coil is represented by lumped inductors L1, L5, L6, L9, L10 and L11. Mutual coupling was implemented between the inductor sections that represent the single coil. When the switch J3 is closed C1 begins to discharge through L1 and into the load seen through the transformer T1. Once the voltage across the load reaches half the original bias across C1, C1 will stop discharging and C2 will start to discharge, this occurs along the line of capacitors until C6 which fully discharges, C5 then fully discharges as so on until the energy stored in the capacitors is transferred to the load. If the load impedance is matched to the PFN impedance the pulse shape is of rectangular width and length twice the transit time along the PFN (the time to discharge each capacitor down the line and back).

The thyratron was simulated as a diode in series with a small resistance. In Figure 4.17, the thyratron model consists of the elements J3, R3, D3 and V8.

The de-spiking network (R2 and C9) appears across the transformer, T1, to deal with the non-linear impedance of the magnetron or klystron.

The magnetron was represented as a biased (V2) ideal diode (D1) in series with a load resistance (R1), all of which were in parallel with a capacity (C8).

4.4.3 Resistive Load Studies

The broadband RF noise generated by the magnetron was isolated from other possible RF sources (such as the thyratron). A high power resistive load replaced the magnetron and microwave water load in one set of measurements.

The high power resistive load consisted of a total of thirty two 50 Ω resistors, the resistors were wired such that there were two parallel banks of sixteen resistors connected in series giving an equivalent 400 Ω load and is shown in Figure 4.18.

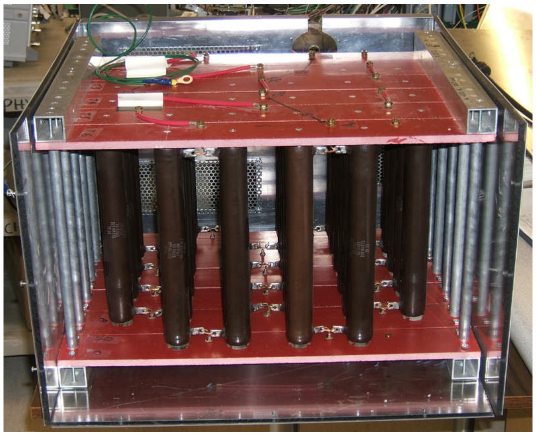

Figure 4.18: High power resistive load used to replace the magnetron and dissipate the energy stored in the PFN.

An RF cage constructed in house was placed around the resistive load to minimize any direct RF emissions from the load. The RF cage consisted of 0.25 inch PMMA sheets placed around the resistive load to prevent arcing (by presenting a path to ground with a large breakdown potential) and an aluminum enclosure built around the PMMA sheets for an RF shield.

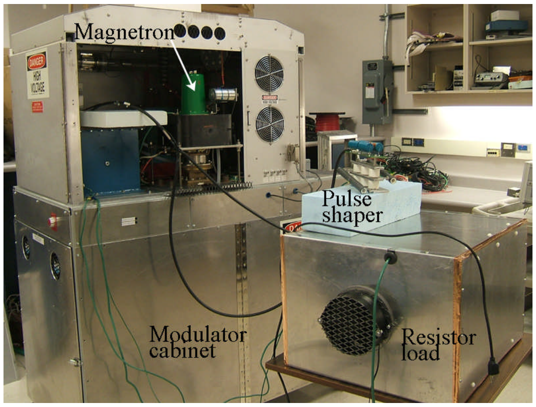

Figure 4.19: Setup used to transfer the high voltage pulse from the transformer to the resistive load.

An estimate of the RF noise produced by the magnetron was determined by measuring the RF noise with the magnetron as a load, replacing the magnetron with a 400 Ω resistive load and re-measuring the RF noise while holding all other variables constant. The difference in the measured RF noise power between the magnetron and resistive load can then be attributed to the magnetron. To investigate any loading effects (that is the possibility of different reflections occurring from the resistor load as compared to that of the magnetron load or any filtering effects due to capacitive differences) a pulse shaper was placed in parallel with the 400 Ω load. The pulse shaper consisted of a 0.5 mF capacitance in series with 30 kΩ resistance.

4.4.4 PFN Coil Simulations and Measurements

When unwound the PFN coil is approximately 20 m in total length, at this length it could act as a good radiator in the tens of MHz range. A separate investigation was undertaken to determine the RF fields produced by the PFN coil during discharge. The MultiSIM (National Instruments, Austin, Texas) software package was used to simulate the complete circuit of the modulator shown in Figure 4.17 and to calculate the voltages and currents at specific points in the circuit of the modulator. Specifically the simulation included: a power supply; a large choke inductor and De-Q circuit; the PFN coil, the thyratron and the magnetron. The simulation also included the de-spiking network, a voltage divider circuit to measure the PFN voltage, a circuit to measure the high voltage power supply current, a transformer between the thyratron and the magnetron. A simple current probe was used to measure the current through the magnetron. The modulator simulation was validated by comparing the measured voltages or currents at the same locations in the modulator as those calculated by the simulation. The simulated currents through the PFN coil were used as inputs into a second software program, COMSOL Multiphysics (COMSOL Inc., Los Angeles, California), which was used to determine the E and H field strengths from the PFN coil as a function of time during the discharge of the PFN. Due to the approximate axial symmetry of the problem, the simulation of the fields produced around the PFN coil during discharge was performed using a 2D geometry. The coil consisted of quarter-circumference rings of the dimensions and spacing of the PFN coil itself. The axis of the coil was set to axial symmetry at zero radius. All other boundaries were set to magnetic insulation ($A_\varphi = 0$, where A is the vector potential and cylindrical coordinates are used). The setup illustrating the locations of the boundaries is shown in Figure 4.20.

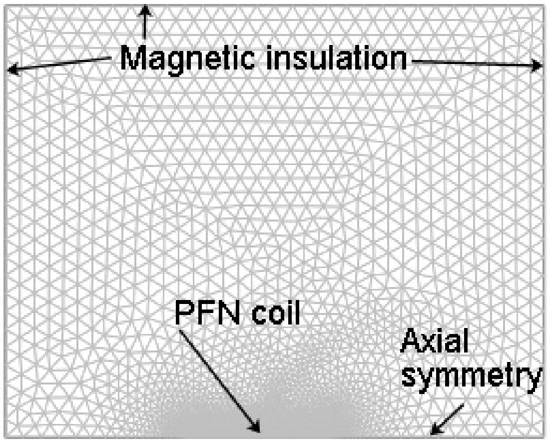

Figure 4.20: Layout of the simulation of the discharge of the PFN. A closer view of the PFN coil is illustrated in Figure 4.2.

The currents on the rings (the PFN coil) were set by defining functions which contained the previously determined coil currents as a function of time. The *E* and *H* field HZ-11 probe set was used for the measurements of the field strengths produced by the modulator. The low frequency *B* field strength was measured using a Senis (Senis GmbH, Zurich, Switzerland) 3M12-2-2-0.2T Hall probe together with a 3-axis type (C-H3A-E3D-1%-0.2T) magnetic field transducer. Since the HZ-11 probes only have a known calibrated response down to 100 kHz, a Hall probe was needed to capture the lower frequency response in both the time and frequency domains.

4.4.5 Saturable Reactor Studies

During thyratron trigger large spikes appear on its grids. We investigated the possibility of these spikes entering the grid trigger circuit and being radiated as RF noise. Two similar saturable reactors (SR) were constructed as described by Richardson [Richardson et al. 2007]. Our SR consisted of six Magnetec M-074 Nanoperm cores (Magnetec GmbH, Lagenselbold, Germany). Nanoperm is a ferromagnetic alloy of composition 73.5% Fe, 1% Cu, 3% Nb, 15.5% Si and 7% B. It is distributed in the form of a thin tape with a thickness of approximately 20 μm wound hundreds of times [Feryster 2009]. The SR was wound with two by five turns (two separate wires each wound five times in opposite directions) of Belden (Belden Inc., Richmond, Indiana, USA) 8869 high voltage cable. A single turn from standard bench-top wire was used for the control winding. The setup used to operate the SRs is shown in Figure 4.21. Two power supplies were used to bias the reactors to the desired operating point. Resistors R1 and R2 were used to set the current through the SRs and the inductors L1 and L2 operated as bias hold off chokes.

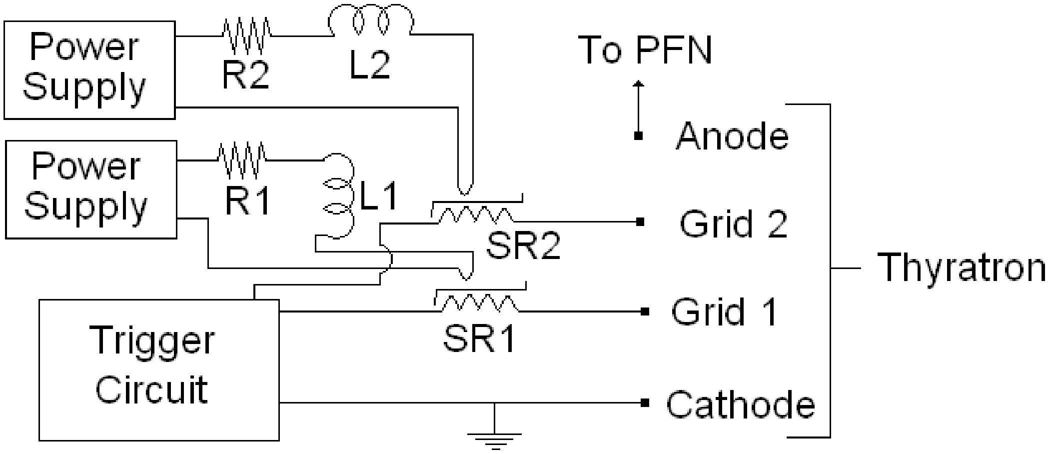

Figure 4.21: Setup used to suppress the voltage spikes seen on the thyratron grids at the instant of firing.

The operating point of the DC bias supply of the SR was determined by measuring the inductance as a function of applied DC current. The basic setup is shown in Figure 4.22.

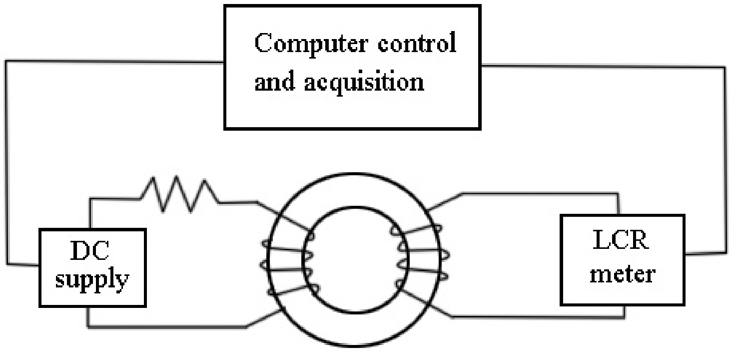

Figure 4.22: Setup used to measure the inductance of the saturable reactor as a function of applied DC current.

A Stanford Research Systems (Stanford Research Systems Inc., Sunnyvale, California, USA) LCR meter (model SR715) was used to measure the inductance of the SR. A Kepco (Kepco Inc., Flushing, New York, USA) power supply/amplifier (model BDP-100-2M) was used for the DC bias. The output of the Kepco supply was controlled using the National Instruments (National Instruments Coorporation, Austin, Texas, USA) hardware control package. A DAQ card (National instruments USB-6221) was used to read the data from the LCR meter and set the voltage on the power supply. The output of the power supply was stepped in 0.03 A intervals while the LCR meter measured the inductance, a table of the applied current and the measured inductance was recorded. The data was analyzed offline to determine the proper operating point for the SR.

The RF noise from the spikes on the thyratron grids was investigated by measuring the RF noise during normal operation and measuring the RF noise after installing the two SRs described above. As shown in Figure 4.21 the SRs were connected directly to the thyratron grid contacts such that the trigger pulses had to pass through the SR. The *E* and *H* field probe set was used to measure the power spectral density. The same hardware and software techniques as previously described were followed. A direct comparison between the RF noise with and without the use of the SRs was used to deduce the RF noise generated by the spikes entering the trigger circuit.

4.5 Results

4.5.1 Motivation: RF Noise Measurements on Clinical Linacs

The measurement of the RF noise, with the *E* field probe, inside a clinical vault in the time domain is shown in Figures 4.23. Figure 4.24 shows this data in the frequency domain. The data illustrates the time and frequency coincidences between the *E* probe signal and the high voltage power supply current.

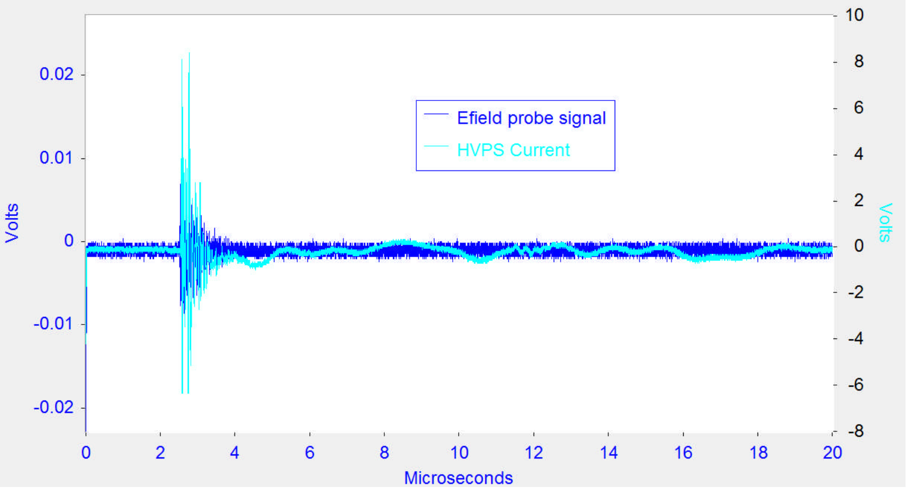

Figure 4.23: Time coincidence measurement with the electric field probe signal and the high voltage power supply current. (The signal shown is that of the oscilloscope trace)

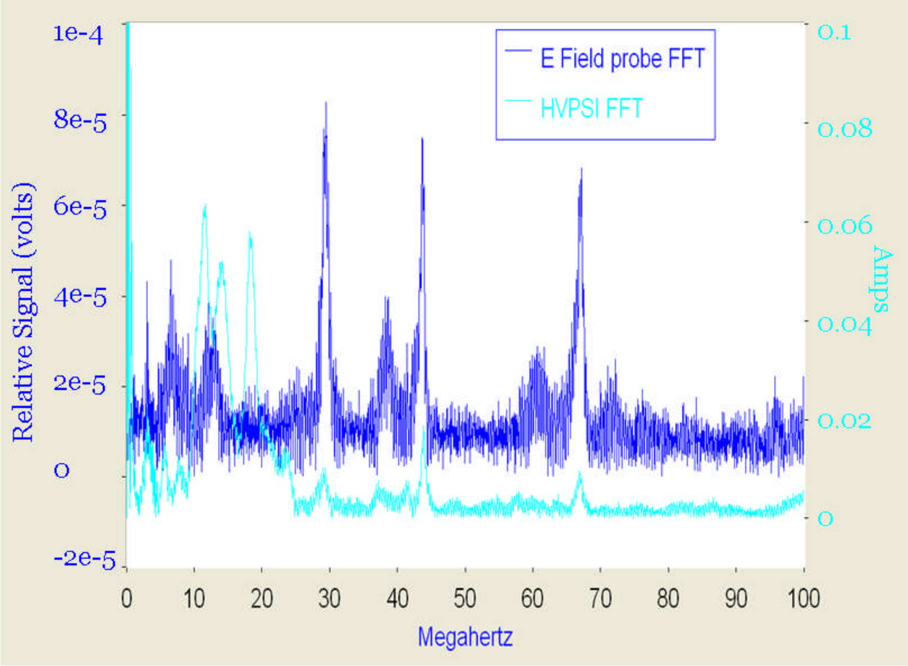

Figure 4.24: The measured relative electric field signal and high voltage power supply current in the frequency domain.

4.5.2 Simulations and Measurements

Figure 4.25 shows the measured and simulated magnetron current in both the time and frequency domains. Figure 4.26 shows the measured and simulated power supply current in the time and frequency domains. These measurements were used to validate the simulation.

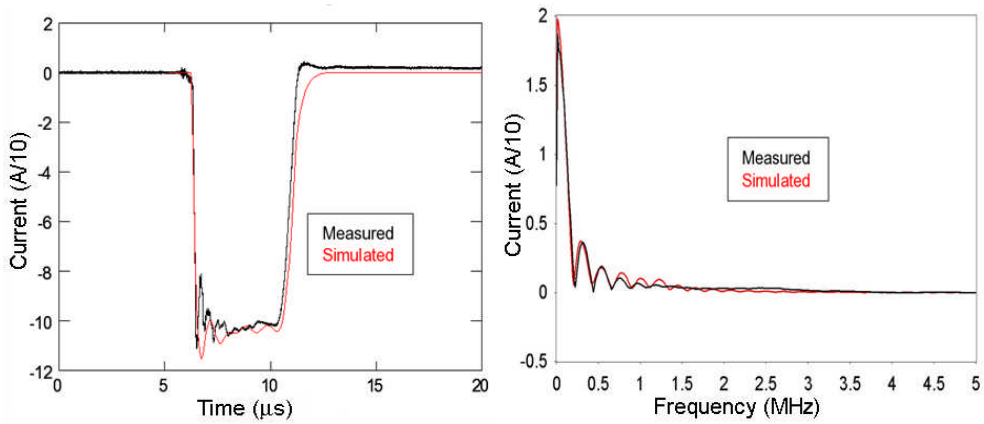

Figure 4.25: (left) Measured and simulated magnetron current in the time domain. (Right) Measured and simulated magnetron current in the frequency domain.

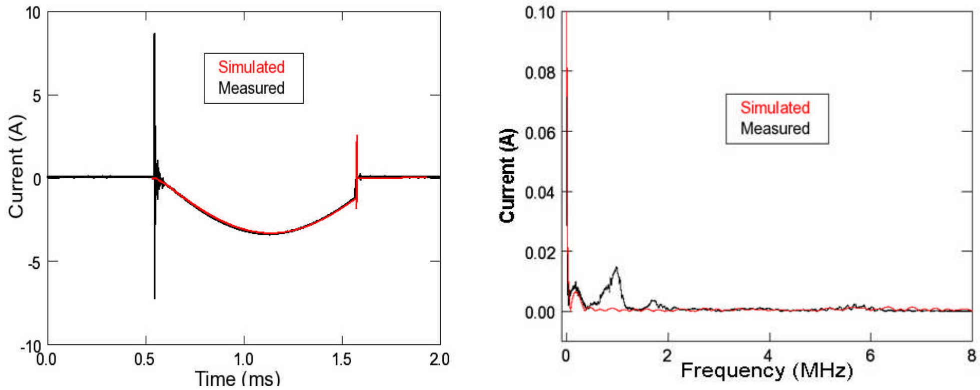

Figure 4.26: (left) Measured and simulated high voltage power supply current in the time domain. (Right) Measured and simulated high voltage power supply current in the frequency domain.

4.5.3 Magnetron and Resistive Load RF Studies

The measured RF power spectral density with the magnetron and resistive loads are shown in Figures 4.27 and 4.28. Figure 4.27 shows the data in the frequency range 20-400 MHz while Figure 4.28 shows the data in the frequency range 2-20 MHz. Three curves of the measured RF power spectral densities are shown in each plot; the magnetron load, the resistive load and the resistive load with pulse shaper (modified resistive load). The data is shown in two plots due to the different scales for the two regions. On a linear scale the structure in Figure 4.27 cannot be seen on the scale used in Figure 4.28.

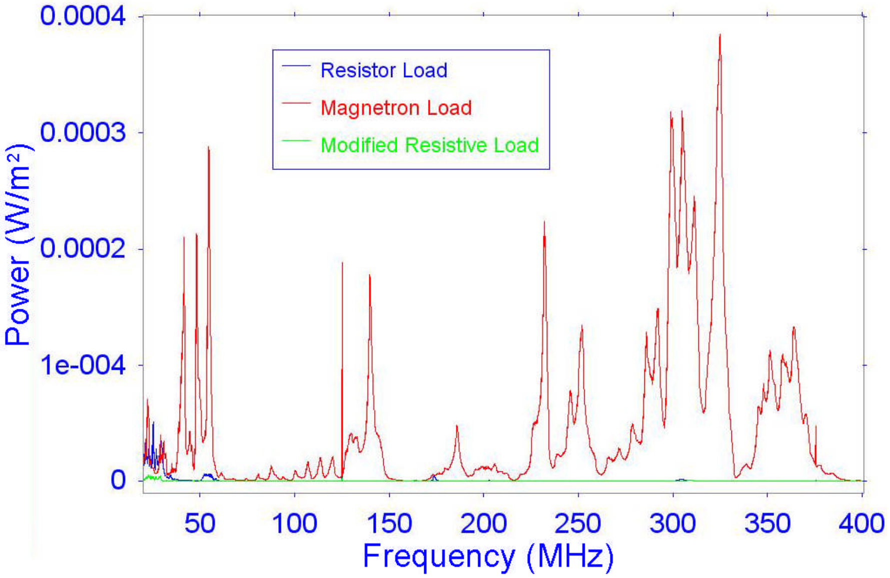

Figure 4.27: Measured RF power spectral density when a modulator was loaded with a magnetron a resistive load and with a modified resistive load, in the frequency range 20-400 MHz.

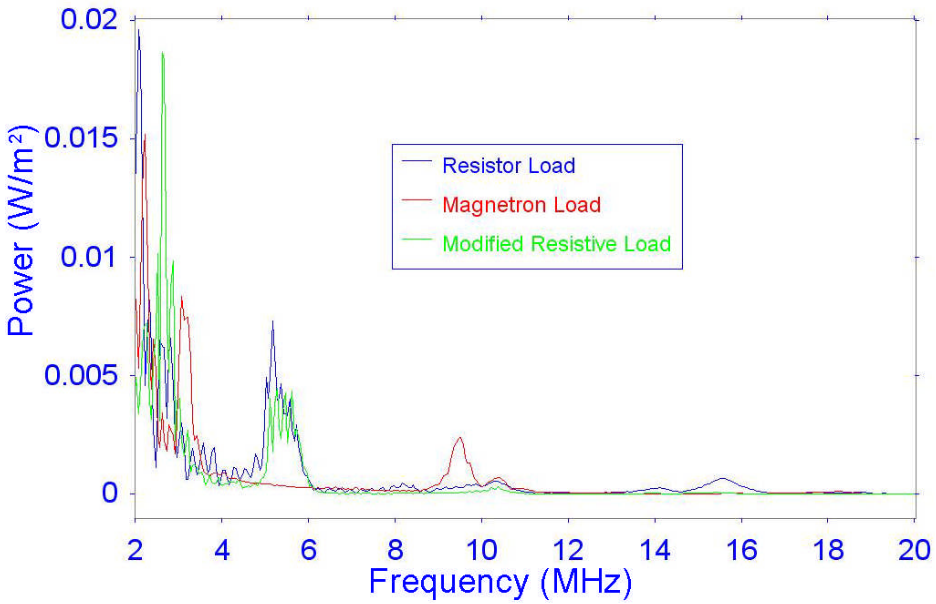

Figure 4.28: Measured RF power spectral density when a modulator was loaded with a magnetron a resistive load and with a modified resistive load, in the frequency range 2-20 MHz.

4.5.4 PFN Coil Simulations and Measurements

Figure 4.29 shows the resulting individual PFN capacitor voltages as a function of time during discharge. The voltages are shown here since they provide a clearer illustration of the PFN discharge. The individual currents were used as inputs into COMSOL to determine the fields around the coil during discharge.

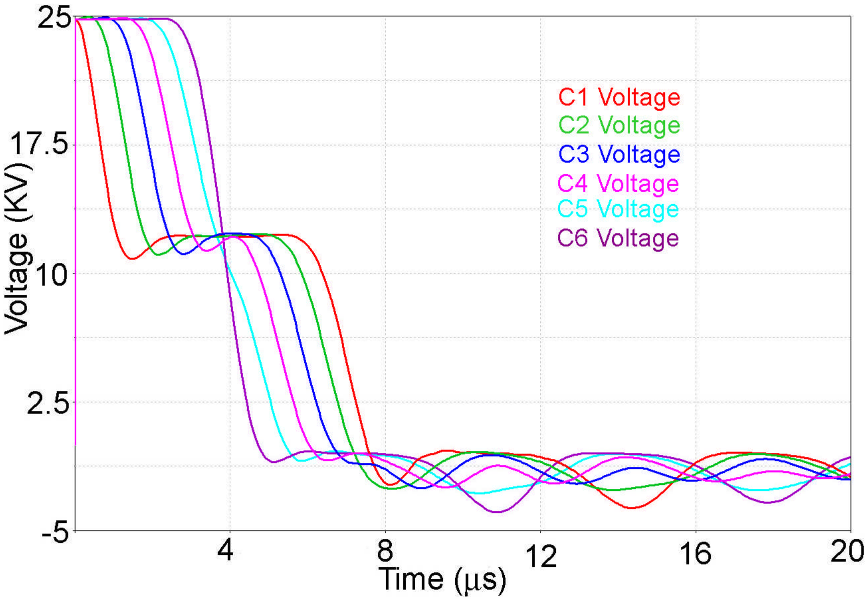

Figure 4.29: Capacitor voltages during the discharge of the PFN into an equivalent magnetron load. The capacitor numbers correspond to those in Figure 4.17.

The simulated and measured magnetic field at 0.8 m from the center and perpendicular to the axis of the PFN coil is shown in Figure 4.30. Figure 4.31 shows the power spectral density of the simulated data illustrating that the majority of the power is contained at lower frequencies.

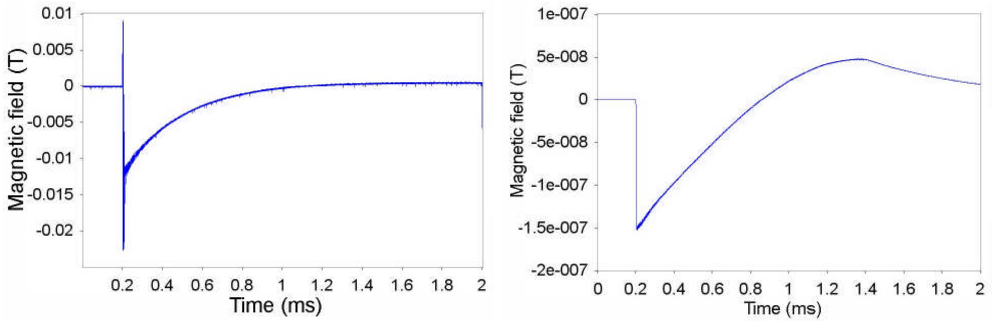

Figure 4.30: (left) Measured magnetic field at 0.8 m from the PFN coil and (Right) simulated magnetic field from the PFN coil at the same position as the measurement.

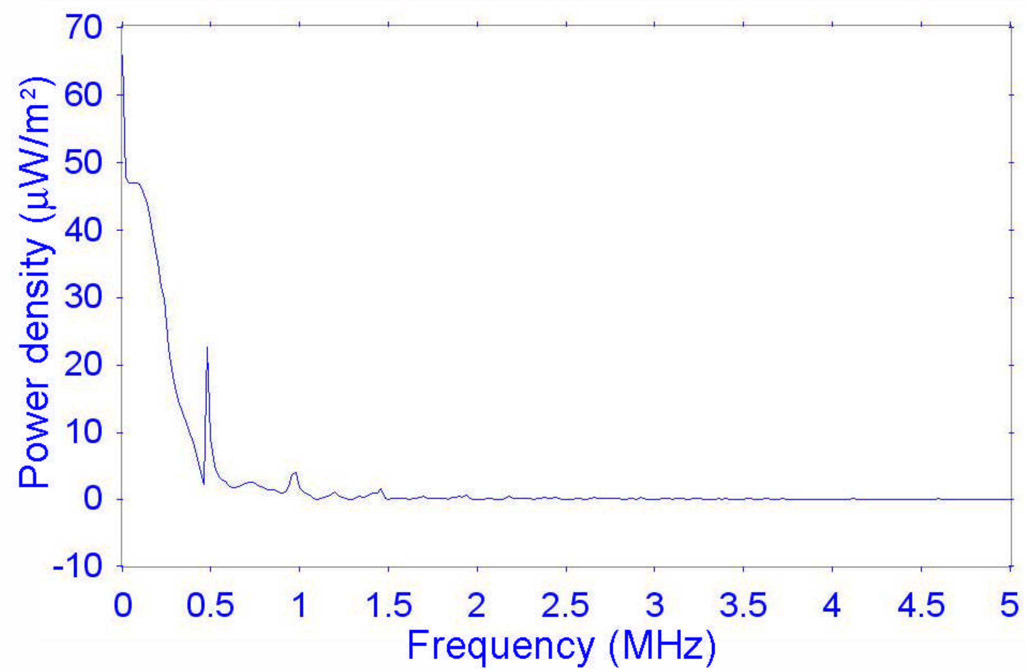

Figure 4.31: RF power spectral density of the simulated PFN discharge currents at 0.8 m from the PFN coil. The data is shown in bin widths of 20 kHz.

4.5.5 Saturable Reactor Studies on the Thyratron Grid Spike

Figure 4.32 shows our measured grid 2 voltage with and without the use of an SR. The data shows that the SR greatly reduced the magnitude of the spike. Also shown in Figure 4.32 is the spectrum of the grid spike. The spectrum illustrates that broadband frequencies exist up to approximately 95 MHz in the spike and that the use of an SR reduced the higher frequencies making up the spike. Above 95 MHz the data drops by a factor of 10 to the noise floor. No de-rating curve was applied to the data; the data illustrates a relative change in the spectrum and a response up to 95 MHz. The magnitude of the grid spike is smaller than that reported in the literature [Richardson et al. 2007] due to the de-rating curve of the probe used.

Figure 4.33 shows the measured inductance of the SR as a function of applied current. The Figure illustrates the current at which the SR saturates. This information was used to bias the SR. Figure 4.34 shows the measured RF power spectral densities during normal operation and when our SRs were used to block the grid spikes from entering the trigger circuit. This data is shown in the frequency range 5 – 70 MHz. This range is shown since the Larmor frequencies for 0.2 – 1.5 T MRI systems are contained therein.

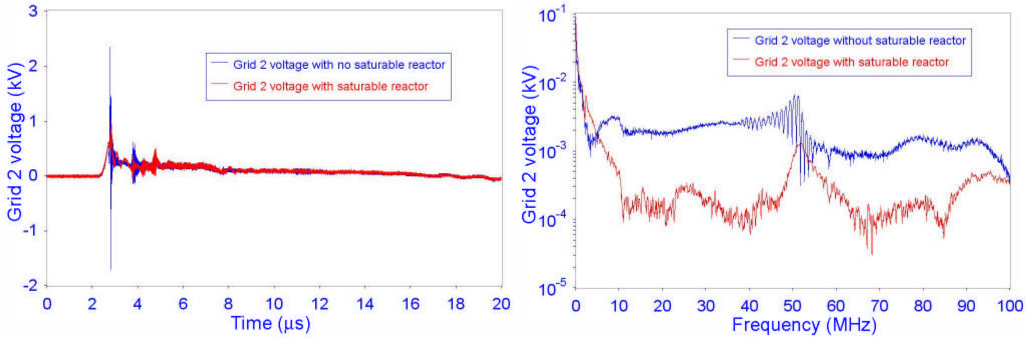

Figure 4.32 (Left) measured grid 2 voltage spike with and without a saturable reactor. The illustrated spike voltage is smaller than the actual spike due to the probe de-rating curve. (Right) Spectrum of the grid 2 voltage spike illustrating a response near 50 MHz. No de-rating curve was applied to the data.

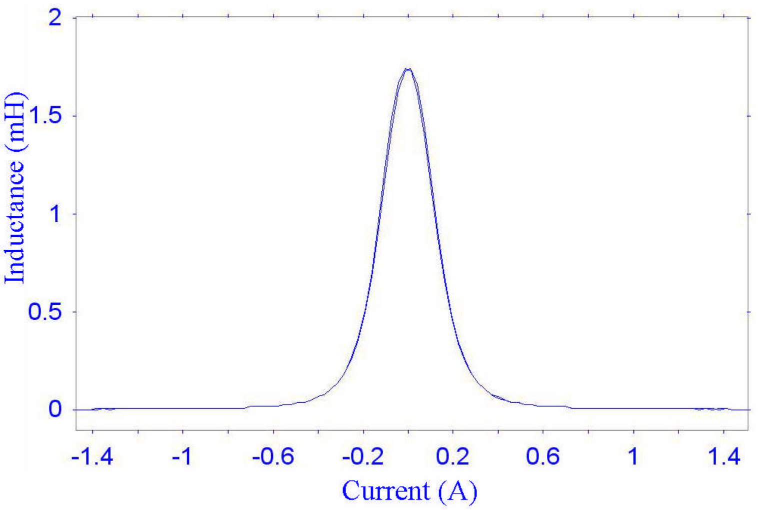

Figure 4.33: Measured inductance of the saturable reactor as a function of applied current through the DC winding around the reactor. A bias value of -0.15 A was used in this work.

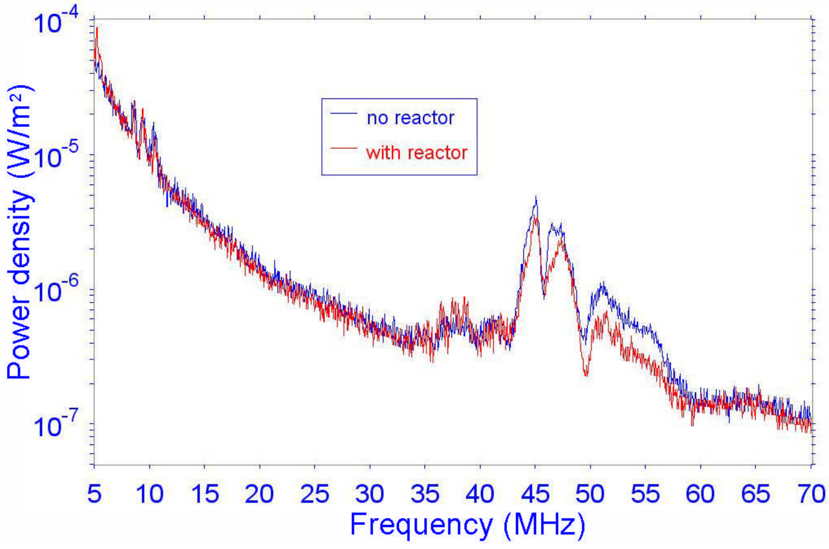

Figure 4.34: Measured RF power spectral density from the modulator with and without saturable reactors placed along the two grid lines of the thyratron.

4.6 Discussion

A linac produces radiation in brief pulses during which the modulator and magnetron produce RF noise [Burke et al. 2009]. For Integrated linac-MRI systems it is desirable to understand the process and production of RF noise from the modulator of a linac. The RF noise produced by the modulator of a linac can be picked up by the coils used in MRI and result in deleterious effects on image quality. An understanding of the sources of RF noise will aid in the design of linac-MRI systems.

Safety considerations were observed by following safety code 6 which is governed by Health Canada. The results of this work are given in Appendix E. The RF noise from a clinical linac was measured with the results shown in Figures 4.23 and 4.24. The data illustrated both time and frequency dependence of the signals measured in the modulator, and that of the RF noise measured with a near field probe set. The results illustrated both time coincidence and frequency overlap between the measured signals in the modulator cabinet and the measured RF noise. The results of these measurements provided motivation to study the signals in the modulator.

A model of the modulator was constructed and verified using the measured signals in the modulator (Figures 4.25 and 4.26). Beyond the electronics schematics, upon which the model was formulated, an extraneous inductance was required to match the measured current waveform on the primary side of the transformer, T1. This extraneous inductance was placed at the same location as the transformer leakage inductance. The simulation of the magnetron current did not require this extraneous inductance. The need for this inductance may have arisen from stray inductances which would not be given in a lumped-element electronics schematic.

A magnetron is known to be a source of RF noise [Okress 1961, Collins

1948, Yamamoto 1987, Little 1958 and Groshkov 1978]. However it is important to determine the contribution to the overall RF noise due to magnetron operation. For this purpose, the generated RF noise from the modulator of a linac was measured when loaded with a magnetron, and then with a purely resistive load. From figures 4.27 and 4.28 we can see that above 35 MHz the majority of the noise produced by the modulator can be attributed to the magnetron. Below 35 MHz other processes also contribute to the production of RF noise. The resistive load may not represent the frequency response of the magnetron's equivalent circuit model. Thus, the reflected signal to the primary side of the transformer may not be the same in the two cases. Loading effects were investigated by using a pulse shaper on the resistive load. When the pulse shaper was added to the resistive load its effects were prevalent in the frequency ranges 20-55 MHz and below 4 MHz (as seen in Figure 4.27). The change in the behavior of the resistive load with the pulse shaper may indirectly suggest that, in these frequency ranges, other mechanisms of RF production may exist beyond those that can be attributed directly to the magnetron operation.

When the thyratron starts to conduct, the PFN capacitors at first discharge half their energy stored sequentially starting with the closest to the thyratron and then discharging the remaining energy in the reverse order (this process is shown in Figure 4.29). During this discharge frequencies in the MHz range exist on the PFN coil. An attempt was made to quantify the production of RF noise from the PFN coil using measurements and simulations. Figure 4.30 illustrates that the measurement and simulations of the magnetic field show similar shapes; this can be expected from the fact that this is the shape of the PFN charging voltage. However the magnitudes of the measured and simulated magnetic fields are significantly different. The data shown in Figure 4.31 illustrates that the PFN coil may produce some RF noise, but only at lower frequencies (below 1 MHz). When comparing Figure 4.27 and 4.28 to Figure 4.31, we can see that the mechanisms of RF noise production are significantly larger than the simulated power emanating from the PFN coil. We also note that the data shown in Figure 4.31 is in a direction perpendicular to the PFN coil. The fields along the PFN coil axis are slightly larger but are still insignificant to those shown in Figures 4.27 and 4.28 (this data is not shown). Therefore, it is unlikely that the direct radiation of RF noise from the PFN coil is a significant issue.

A thyratron is also known to produce RF noise up to 20 MHz [Landahl et al. 1998]. Large spikes are seen on the grids of the thyratron at the instant of firing just before the discharge of the PFN. The magnitude of these spikes can reach a substantial fraction of the anode voltage [Richardson et al. 2007], which is typically 24 kV for low energy linacs. A Fourier analysis of these spikes shows that frequencies up to approximately 90 MHz exist; specifically frequencies in the range 45 to 60 are present. Two SRs were constructed and placed on the grids of our thyratron as illustrated in Figure 4.21. The RF noise was measured with and without these SRs connected. The measured data, in the frequency range 5 - 70 MHz, is shown in Figure 4.34. The RF noise is reduced in the frequency range 42 – 60 MHz; albeit by a small amount. Further work is required to determine if the RF noise in this region can be attributed to the grid spikes. We might expect a slightly different power spectrum here as compared to Figures 4.27 and 4.28; this is because different panels of the modulator cage were open during these two separate and independent investigations.

If the SR is not operated at the correct point along the BH curve the RF noise is generally increased. The results in Figure 4.34 indicate that the voltage spike directly entering the trigger circuit is not a major mechanism of RF noise production. However, we speculate that other mechanisms such as capacitive or inductive coupling into other parts of the modulator could potentially lead to RF noise generation. For example Goldberg [Goldberg 1953] suggests that the grid spikes occur as a result of inductive coupling effects.

Possible further sources of RF noise generation include an antenna effect from short unshielded wires which transfer the high voltages from one element to another. Some examples of this include signal transfer from the PFN coil to thyratron, from thyratron to transformer and from the transformer to the magnetron.

The RF noise power levels presented in this work are higher than those presented by Burke [Burke et al. 2009]. This is due to the fact that parts of the modulator RF cage had to be removed to acquire the results presented herein. The lack of a complete RF cage leads to measurements of much higher RF power levels which are readily reduced simply by re-establishing the integrity of the shielding.

4.7 Conclusions

This work has shown that the magnetron is a major contributor to the RF noise produced by the modulator of a linac. Above 60 MHz essentially all the noise produced can be attributed to the magnetron. Below 60 MHz other mechanisms can also contribute to the production of RF noise. The PFN coil has been shown not to be a major contributor of RF noise, especially above 1 MHz. It was also shown that blocking the large voltage spikes on the thyratron grids from entering the trigger circuit did not have a major effect on the RF noise generated in the frequency range 5 – 70 MHz. The RF noise generated by a magnetron is a result of the electrons travelling in crossed electric and magnetic fields and then building up to the microwave oscillation. This noise cannot be reduced but can be shielded. Since the majority of RF noise produced by a modulator emanates from a magnetron, this work suggested that the best way to integrate a linac and MRI, would be to place the modulator in an RF shield and to maximize distance to the MRI system by possibly placing the modulator externally to the MRI room. A klystron could also be used as a substitute for the magnetron.

4.8 References

Ashcraft C. and Grimes R. “SPOOLES: An object-oriented sparse matrix library” *Proceedings of the Ninth SIAM Conference on Parallel Processing.* SIAM, Philadelphia, 1999. Software available at http://www.netlib.org/linalg/spooles.

Brenner S., Scott R. L. “The Mathematical Theory of Finite Element Methods”

Springer 2005.

Brown P., Treado T., Aiguier D. and Hansen T. “Upgrade of Varian’s high power microwave magnetron test facility” Power modulator symposium, Conference record of IEEE 61-64 1992.

Chua L. and Lin P. “Computer Aided Analysis of Electronic Circuits: Algorithms and Computational Techniques” Prentice Hall, New Jersey 1975.

Ciarlet P. G. “The Finite Element Method for Elliptic Problems” North-Holland 1978.

Collins G.B. “Microwave Magnetrons” McGraw Hill Book Company Inc. New York Radiation Laboratory series no. 6 1948.

Davis T. A. “A column pre-ordering strategy for the unsymmetric-pattern multifrontal method” ACM Transactions on Mathematical Software, **30**, no. 2, pp. 165-195 2004a.

Davis T. A. “Algorithm 832: UMFPACK, an unsymmetric-pattern multifrontal method” ACM Transactions on Mathematical Software, **30**, no. 2, pp. 196-199 2004b.

Davis T. A. and Duff I. S. “A combined unifrontal/multifrontal method for unsymmetric sparse matrices” ACM Transactions on Mathematical Software, **25**, no. 1, pp. 1-19 1999.

Davis T. A. and Duff I. S. “An unsymmetric-pattern multifrontal method for sparse LU factorization” SIAM Journal on Matrix Analysis and Applications, **18**, no. 1, pp. 140-158 1997.

Feryster Inductive components manufacturer http://www.feryster.pl/polski/nanoperm.php?lang=en Visited July 2009.

Geyger W. A. “Nonlinear-magnetic control devices: basic principles, characteristics, and applications” McGraw Hill book Company, New York 1964.

Glasoe G. N. and J. Lebacqz V. “Pulse Generators” MIT Radiation Laboratory Series, Boston Technical Publishers Inc. Lexington 1964.

Hestenes M. R. and Stiefel E. “Methods of conjugate gradients for solving linear systems” J. Res. Nat. Bur. Standards, **49** 409-436 1954.

Hill R. A. “Analysis of modulator design problems by simulation” Proc. 7th symp. On Hydrogen thyratrons IEEE 165-176 1962.

Jang S. D., Son Y. G., Oh J. S., Lee H. G., Bae Y. S., Cho M. H. and Namkung W. http://psl.postech.ac.kr/publication/dom_poster_phy/kapra_kpsdpp_2004_july_sdjang.pdf KAPRA 2004 presentation.

Jin J. “The finite element method in electromagnetics” John Wiley and Sons, New York 2002.

Little R.P., Ruppel H. M. and Smith S. T. “Beam Noise in Crossed Electric and Magnetic Fields” J. Appl. Phys. **29** iss. 9, 1376-1377 1958.

Lorenz L. “Ueber die fortpflanzung der Electricitat” Wied. Ann. Vol. 7 161-193 1879.

Miller H. C. “Inductance formula for a single-layer circular coil” Proc. IEEE. **75**

256-257 1987.

Monossov H. G. “The two-dimensional mathematical model of electron interaction with UHF field in a magnetron and high-voltage UHF oscillations breakdown” Elec. And Radiophys. of ultra high freq. Int. Univ. Conf. 97-100 1999.

Neculaes V. B. Gilgenbach R. M. and Lau Y. Y. “Low-Noise microwave magnetrons by azmuthally varying axial magnetic field” Appl. Phys. Lett. **83** no. 10 1938-1940 2003.

Okress E. “Crossed-Field Microwave Devices” Academic Press New York 1961.

Richardson B., Sheldrake R and Pirrie C. “Thyratron Grid Protection and Monitor System” 16th IEEE Pulsed Power Conference **1** 438-441 2007.

Rosa E. B. and Grover F. W. “Formulas and tables for the calculation of mutual and self-inductance” Bulletin of the Bureau of standards, **6** 1 1912.

Saad Y. and Schultz M. H. “GMRES: A generalized minimal residual algorithm for solving nonsymmetric linear systems” SIAM J. Sci. Statist. Comput. **7** 856-869 1986.

Schenk O., Gärtner K. and Fichtner W. “Efficient sparse LU factorization with left-right looking strategy on shared memory multiprocessors” BIT, **40** no. 1158-176 2000.

Sivan L. “Microwave tube transmitters” Chapman and Hall, London 1994.

Sokonikoff I. S. “Mathematical theory of elasticity” McGraw Hill, New York 1956.

Toledo S., Chen D. and Rotkin V. “TAUCS a library of sparse library solvers” http://www.tau.ac.il/~stoledo/taucs/ visited August 2009.

Torok L. “Precision inductance modeling is the basis for accurate PFN simulation” Conf. record of the 21st international power modulator symposium 1994.

Varian Modulator System Schematic Diagram, drawing number 872537 1976.

Varian Transformer specification, drawing number 829003 1972.

Varian Schematic, PFN diagram, drawing number 883656 1989.

Varian course book “Varian generic accelerator course book” 2nd ed. Medical and industrial Products service, Education Dept. 1989.

Varian Transformer Spec. (HV Pulse), drawing number 855953 1981.

Vlach J. and Singhal K. “Computer Methods for Circuit Analysis and Design” Nostrand and Reinhold, New York 1994.

Vladimirescu A. “The SPICE book” John Wiley and Sons Inc., New York 1994.

Yu S. P. Kooyers G. P. and Buneman O. “Time-dependent computer analysis of electron-wave interaction in crossed fields” J. Appl. Phys. **36** 2550-2559 1965.

Chapter 5: Radio Frequency Shielding for a Linac-MRI System

A portion of this chapter is in press in the journal physics in medicine and biology: M. Lamey, B. Burke, E. Blosser, S. Rathee, N. De Zanche and B.G. Fallone"Radio frequency shielding for a linac-MRI system" Phys. Med. Biol.

5.1 Introduction

Several groups are currently working on integrating magnetic resonance imaging (MRI) with a megavoltage teletherapy unit [Fallone et al. 2009, Lagendijk et al. 2008 and Dempsey et al. 2006]. A specific problem with the fractionated radiotherapy process is the day-to-day patient setup error and internal organ movement during treatment [van Herk 2004, Webb 2006, Rietzel et al. 2004 and Langden et al. 2001]. Furthermore, the tumour volume can change shape and shrink during the fractionated radiotherapy process [Erridge et al. 2003, Hansen et al. 2006 and Kuo et al. 2006]. Image guided radiotherapy (IGRT) aims to reduce dose to the normal tissue surrounding tumors by reducing the margins needed to account for organ motion, thereby minimizing potential side effects of radiotherapy. Considerable work has been and is currently being pursued to develop imaging systems to guide radiotherapy [Bucci et al. 2005, Meyer et al. 2007, Verellin et al. 2008 and Verellin et al. 2007]. The rationale for image guidance can be seen from the improvements in tumor control and the reductions in normal tissue complication [Eisbruch et al. 1999, Brabbins et al. 2005, Ghilezan et al. 2004 and Pollack et al 2002]. The next significant step toward improving tumor-normal tissue delineation involves the use of real time imaging during radiotherapy treatment. The use of MR images with exquisite soft tissue contrast will enable reductions in the irradiated normal tissue volume around the cancerous tissue by tracking and/or adapting to the current position, shape and size of the tumour. A functional linac-MRI system will enable patient image acquisition during linac irradiation. One of the possible problems associated with linac-MRI integration is the radio frequency (RF) interference between the linac and MRI. RF noise produced by the linac pulsing mechanism could be received by the RF coil used in the MRI and this could have deleterious effects on image quality.

The purpose of the work included in this chapter is to determine the efficacy of shielding RF noise generated by the linac during irradiation. This investigation reports on the results of studying the RF interference mentioned above. Using commercially available electric (E) and magnetic (H) field probes; the frequency spectrum of the RF noise was measured with the linac pulsing. We present the shielding effectiveness of an in house constructed RF cage as well as present images of two phantoms, taken while a 6 MV linac was producing pulsed radiation.

5.2 Theory

The shielding effectiveness (SE) of an RF cage can be measured using transmit and receive antennas. The SE is defined as the difference, in dB, between the received signal with no RF cage present to that with the RF cage present and everything else (such as distance between antennas and the surrounding environment) being held constant [IEEE 2006].

$$\mathrm{SE(dB)} = \mathrm{M}_{\text{no cage}}\mathrm{(dB)} - \mathrm{M}_{\text{with cage}}\mathrm{(dB)} \qquad (5.1)$$

Where $\mathrm{M}_{\text{no cage}}$(dB) is the measurement in dB for either the E or H fields with no cage between the antennas and $M_{\text{with cage}}$(dB) is the measurement in dB for either the *E* or *H* fields with the RF cage between the antennas and all other parameters being held constant. The dB measurements herein are all referenced to 1 mW.

The RF noise inside and outside the RF cage was measured in the time domain using a set of near field electromagnetic probes (Rhode and Schwarz, Munich, Germany). These time domain signals from the *E* and *H* field probes were used to obtain measured spectral density, *M(f)*, in each case as follows.

$$M(f) = \sqrt{\frac{\sum_{i=1}^{N} \left| DFT_i \right|^2}{N}} \tag{5.2}$$

Where $DFT_i(f)$ is the discrete Fourier transform of one time domain acquisition, and *N* is the number of averages used in the estimation of *M(f)*.

The actual field strength values are then related to the measured values, *M(f)*, by applying a known performance factor *PF(f)*. For example, the *E* field is related to the measurement as follows.

$$E = M(f) \cdot PF(f) \tag{5.3}$$

Substitute *H* for *E* in Equation (5.3) for the *H* field. A thorough analysis of the performance factors for the near field probes can be found in Appendix A. The approximate power spectral density (*P*) of the RF noise was then calculated using the following formula:

$$P_{Upper} = \frac{E \cdot H}{2} \tag{5.4}$$

The use of this equation provides an upper limit to the measured power. The data presented herein is shown as an RF power spectral density.

5.3 Materials and Methods

The Linac-MRI setup is shown in Figure 5.1 and is also described by Fallone [Fallone et al. 2009]. The present prototype system consists of a bi-planar 0.22 T MRI from MRI Tech Co. (Winnipeg, MB, Canada) and a 6 MV linac is mounted to direct radiation in between the magnet poles. The linac and MRI are located within an RF cage constructed in-house ($123 \times 93 \times 245$ cm^3). The modulator of the linac however, is located externally to the RF cage in an adjacent room to prevent interference with the MRI operation (as shown in Figure 5.1). The RF cage is constructed of approximately 1.6 mm thick copper, three doors provide easy access to the linac, MRI and associated cables. Reliable electrically conducting contacts are made between these doors and the RF cage using specialized RF door fingers (Laird Technologies, Chesterfield, Missouri, USA) along the four sides of each door. RF fingers (Laird Technologies, Chesterfield, Missouri, USA) are used as contacts along the seams of the copper sheets. Several feed-through points on the RF cage are required for both the MRI and linac. The MRI requires feed through points at the RF cage for six gradient coil cables (±X, ±Y, ±Z), one sample RF excitation pulse cable, one sample RF receive signal and one transmit-receive switch bias for the MRI coil. The linac also required feed through points at the RF cage for the waveguide, the high voltage pulse for the electron gun, an ion pump cable and eight BNC lines to the ion chambers used for dose monitoring.

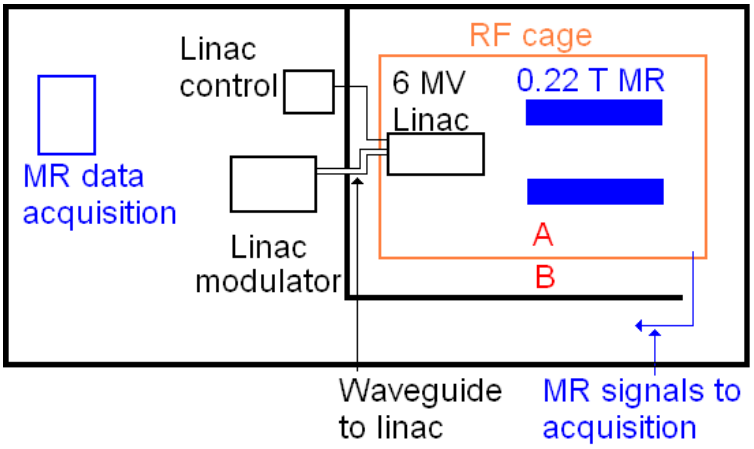

Figure 5.1: Plan view of the prototype linac-MRI system at the Cross Cancer Institute illustrating the layout of the RF cage, MRI, linac, modulator cabinet, waveguide and MRI hardware.

The electron gun voltage pulse produced by the linac modulator is fed into the RF cage using two high voltage wires inside a copper pipe. Inside the RF cage, at the interface of the end of the copper pipe and the linac, copper wool was wrapped around the wires and conductive copper tape was used to ensure continuous RF contact. The ion pump bias line is transferred to the cage using a Belden RG 59/U coaxial cable and is filtered at the cage. Within the cage the ion pump and ion pump cable were shielded using copper tape. Eight cables used to bias and read the signals from the ion chambers are carried along eight RG 174/U cables and are filtered with TESCH feed through filters (part # 02000200, TESCH, Wuppertal, Germany). The waveguide transferring the 3 GHz power was fed through the RF cage and contact to the cage was made through RF fingers clamped down between the waveguide and the RF cage to provide the necessary RF contact. It should also be mentioned that the 3 GHz power, needed for electron acceleration, is well contained within the waveguide, the guide is also connected to the RF cage to shield extraneous RF noise from the modulator.

External to the cage the MRI gradient currents are transferred using an 8 AWG MTW cable (part number 41109, Coleman cable, Waukegan, Illinois, USA) and then filtered using standard feed through filters (part # 02000263, TESCH, Wuppertal, Germany). The transmit-receive switch bias is carried along a Belden 9502 cable (Belden, Richmond, Indiana, USA); it is then also filtered using feed through filters (part # 02000203, TESCH, Wuppertal, Germany). The excitation pulse for the MRI coil is carried by an LMR-400 coaxial cable, no filter was necessary for this line.

The MRI preamplifier was placed within the RF cage in a low radiation field zone. External to the RF cage the signals from the MRI coil are transferred to the data acquisition system using LMR-195 coaxial cables which provide excellent shielding against RF noise external to the RF cage.

Within the RF cage the linac accelerating structure is encased within a 1″ thick cylindrical steel tube with end caps. The steel structure has holes for the waveguide, two sets of water cooling lines and electron gun cables to pass through and for useful radiation to exit. Any seams in the steel structure are RF sealed using conductive copper tape, thus the steel structure provides RF as well as magnetic shielding. Further RF shielding around the steel structure is provided by the lead radiation shield whose joints are also sealed with copper tape.

Measurements of the E and H fields were taken both outside and inside the RF cage while the linac was operating. Inside the RF cage the time domain signal from the field probes was first amplified using a Rhode and Schwarz broadband preamplifier (model 7405-907BNL), displayed and acquired by an Agilent DSO6104A (Agilent Technologies, Santa Clara, California, USA) oscilloscope, then transferred to a PC using a Keithley KUSB 488 GPIB interface (Keithley Instruments Inc, Cleveland, OH). The software program DADiSP (DSP Development Corporation, Newton, MA) was then used for calculating the *E* and *H* field spectral density, as per Equation (5.2). Measurements outside the RF cage did not require the use of a preamp, the signals from the field probes were directly fed into an Oscilloscope.

No standard method exists to measure the SE of an RF cage whose dimensions are smaller than $2 \times 2 \times 2\ \mathrm{m}^3$ [IEEE 2006]. However, the same method and techniques described in the document on the use of balanced antennas and antenna setup was applied. The IEEE 2006 document also suggests frequencies at which measurements should be taken; the measurements presented herein were at these recommended frequencies. The setup used to measure the SE is shown in Figure 5.2.

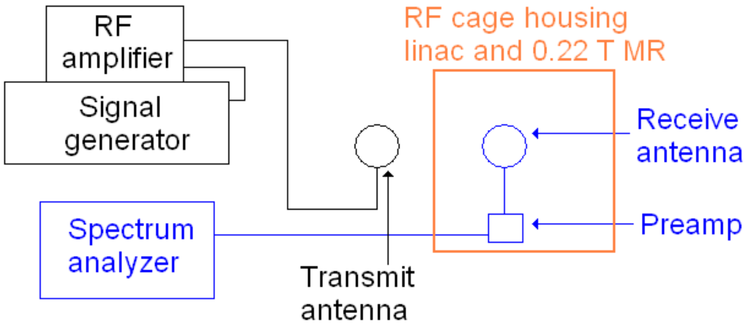

Figure 5.2: Setup used to measure the shielding effectiveness of the RF cage housing the linac-MRI system. Loop antennas were used to measure the *H* field SE while rod antennas were used to measure the *E* field SE.

To measure the *H* field SE of the RF, a 30 cm diameter loop transmit antenna was made of coaxial cable with a notch cut out of the shield, as described by King [King 1945]. The receive antenna for the H field was a 6 cm loop antenna from the near field HZ-11 probe set (Rohde and Schwarz, Munich, Germany). This small 6 cm loop antenna is also balanced with a notch cut out of the shield. To measure the *E* field two 30 cm rod antennas were used. The IEEE 2006 standard suggests using biconical antennas in the frequency range above 20 MHz. However the MRI, linac, linac shielding and a block of steel for magnetic field symmetry (opposite the linac) are all located within the RF cage. Only smaller antennas could be placed within the cage for measurements, furthermore, there is less than 1 meter separation between the RF cage and the walls of the room. Because of this we were limited in the size of the antennas that could be used. Despite using rod antennas rather than biconical antennas a dynamic range > 100 dB was achieved in the frequency range 1- 50 MHz which is the quantity of importance while measuring the SE.

Ferrites were used for both the *E* and *H* field SE setups along the cables feeding the antennas; this was done to reduce any common mode currents resulting from an unbalanced antenna. The ferrites were made of ferrite mixture #31 which is designed to specifically work in the 1- 300 MHz frequency range [Brown 2008]. The feed lines to the transmit antennas were arranged to run perpendicular to the antennas. An Agilent E4400B ESG series signal generator (Agilent Technologies Inc. Santa Clara, California, USA) with an OPHIR$_{\text{RF}}$ 4035 RF power amplifier (OPHIR RF, Los Angles, California, USA) was used to send signals to the transmit antenna. An Agilent 4396B Network/Spectrum/Impedance analyzer (Agilent Technologies Inc. Santa Clara, California, USA) was used in spectrum mode for acquisition from the receive antenna.

After the RF shielding was complete, images of two phantoms were used to verify the shielding efficacy. The specific phantoms were chosen so that the RF noise effects from the linac could be studied and quantified. The first phantom was an acrylic right rectangular prism ($15.95 \times 15.95 \times 25.4$ mm^3) with three holes of diameters 2.52, 3.45 and 4.78 mm drilled into it, inserted into a 22.5 mm diameter tube and filled with a 10 mM solution of $CuSO_4$. The second phantom consisted of four tubes of 2.7 cm diameter filled with gelling powder (20 g/L) and a solution of KCl (18 g/L), $CuSO_4$ (1 g/L) and sugar (600 g/L). Two separate coils were used in the study; a small ~ 3 cm diameter solenoidal (~ 14 turns with a 0.5 cm pitch) coil was used to image the first phantom. A larger ~ 11 cm diameter solenoidal (6 turns with a 2.5 cm pitch) coil was used to image the second phantom.

The MRI console is as described by Fallone [Fallone et al. 2009], a TMX NRC (National Research Council of Canada, Institute of Biodiagnostics, Winnipeg, MB, Canada). The console software is based on Python programming language (Python Software Foundation, www.python.org), version 2.3.4, to allow the user full control of development and modification of pulse sequences. Analogic (Analogic Corporation, Peabody, MA) AN8295 gradient coil amplifiers and AN8110 3 kW RF power amplifiers are used in the TMX NRC system. The following settings were used in a gradient echo MR imaging sequence; flip angle:

90^{o}, slice width: 20 mm, acquisition size: 256 (read), 128 (phase encode), FOV: 100×50 mm^2, TR: 300 ms, TE: 20 ms, 1 signal average. For the second phantom the acquisition size was increased to 256×256 and the FOV was increased to 100×100 mm^2. The phantoms were imaged in three scenarios; (1) the linac power on but not producing radiation, (2) the linac producing radiation but with lead blocking the radiation just before the MRI coil and (3) the linac producing radiation with the radiation hitting the MRI coil.

Two methods were used to quantify the image quality. The signal to noise ratio (SNR) was determined by taking the mean in a signal region divided by the standard deviation of the background in a region near the corner of the image. For the first phantom the signal containing region was taken in a ~ 6×6 pixel^2 region, and for the second phantom a larger ~ 10×10 pixel^2 region was used. The standard deviation of the background in both cases was taken in an ~ 12×12 pixel^2 region (a larger region was taken to get a better estimate of the standard deviation). The second image quality measure involved displaying the k-space data with an appropriate window and level. The background intensity was increased allowing any RF noise to be easily visualized (see Figure 5.9 for clarification). We also note that the linac pulsing and MRI pulse sequences operate completely independently and asynchronously.

5.4 Results

The RF noise power spectral density noise generated by the linac operation as measured externally and internally to our RF cage and is shown in

Figure 5.3. The power levels in a 50 kHz bin approach 0.1 mW/m^2 external to the cage while internal to the cage the levels are near or well below 10 nW/m^2 (in the frequency range shown; 5-100 MHz).

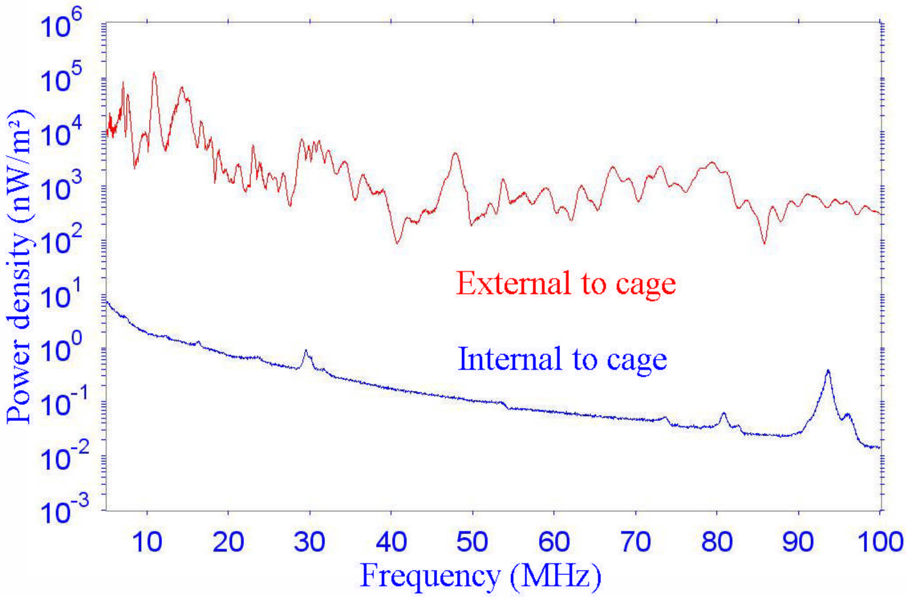

Figure 5.3: Measured power spectral density externally and internally to our RF cage while the linac produced radiation. The data shown is in 50 kHz bin widths.

The shielding effectiveness of the RF cage for the *E* and *H* fields is shown in Figure 5.4. Above 10 MHz the SE is larger than 100 dB in both cases while from 1 to 10 MHz the SE is well above 90 dB. The SE measurements were taken twice and at all measurement frequencies were determined to be reproducible within 2 dB.

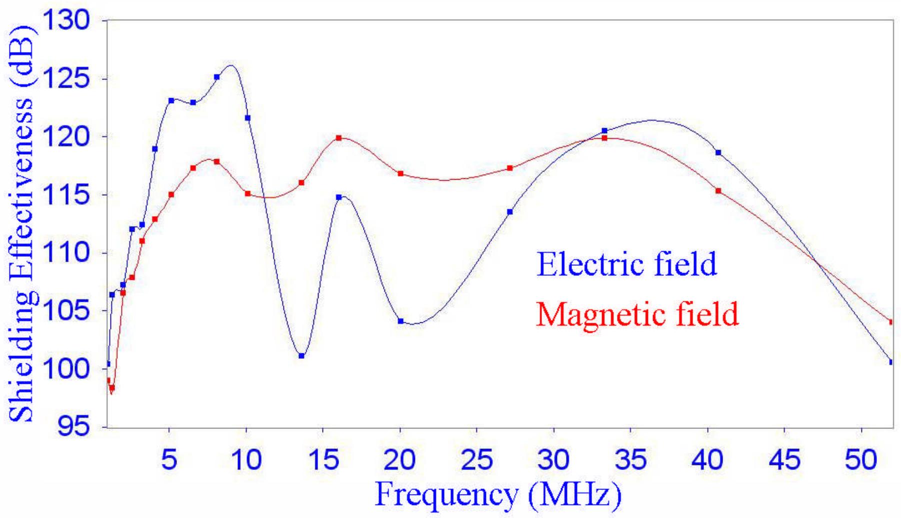

Figure 5.4: Measured shielding effectiveness of the RF cage housing our linac-MRI prototype system. The shielding effectiveness was measured using a set of loop antennas for the *H* field and a set of rod antennas for the *E* field.

Images of the first (rectangular cuboid) phantom are shown in Figure 5.5. Phantom images, on the left and right in Figure 5.5, were obtained without and with the linac producing pulsed radiation respectively. The MRI coil was shielded from the x-ray radiation during the linac operation. No degradation in SNR was observed when the linac was pulsing. In Figure 5.6 shows the associated k-space data, on the left is the data with the linac not pulsing and on the right is the data with the linac pulsing. Small signal voids are likely due to gas bubbles in the solution.

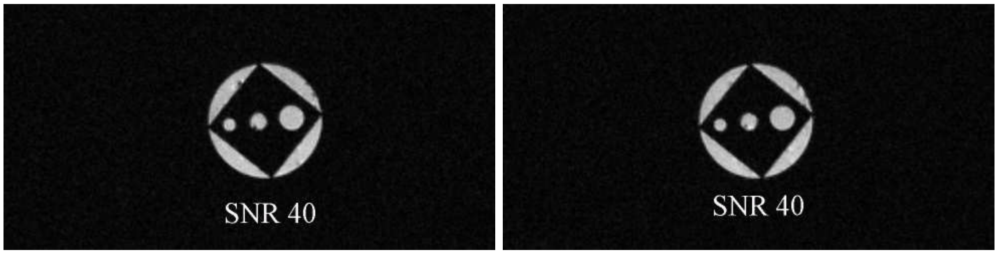

Figure 5.5: MRI images of a right rectangular prism phantom, (left) linac not producing radiation (right) linac producing radiation with lead blocking the coil from the x-ray radiation.

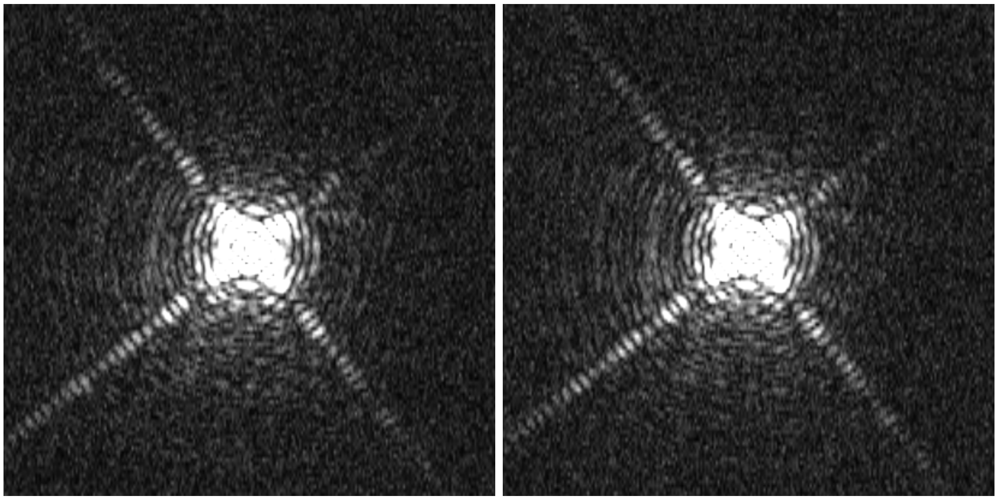

Figure 5.6: MRI k-space data of the images shown in Figure 5.5, (left) linac not producing radiation (right) linac producing radiation with proper RF shielding.

Images of the second (gel) phantom are shown in Figure 5.7. As above the image on the left in Figure 5.7 is taken with the linac not pulsing while the image on the right is taken with the linac pulsing. No degradation in SNR was measurable while the linac was pulsing. Figure 5.8 shows the associated k-space data to Figure 5.7, on the left is the data with the linac not pulsing, while on the right is the data with the linac pulsing.

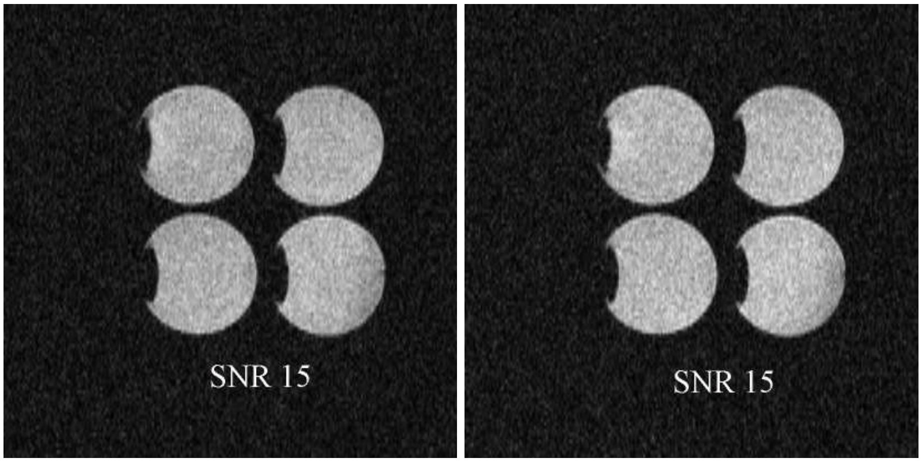

Figure 5.7: MRI images of a gel phantom, (left) linac not producing radiation (right) linac producing radiation with lead blocking the coil from the x-ray radiation.

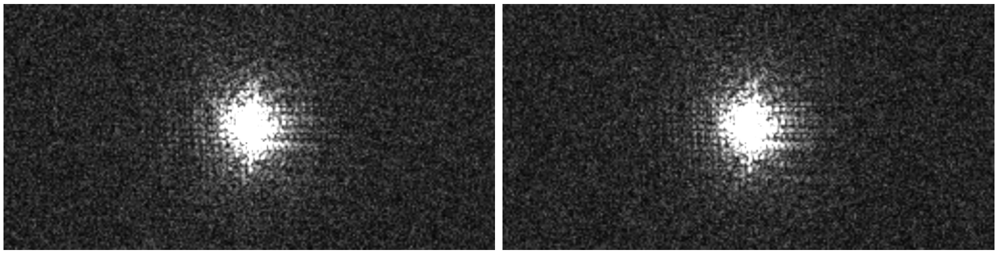

Figure 5.8: k-space data of the images shown in Figure 5.7, (left) linac not producing radiation (right) linac producing radiation with proper RF shielding.

The reproducibility of the measured SNR and k-space effect was tested by acquiring ten images with the linac off, ten images with the linac pulsing and the x-ray radiation being blocked. In each of these sets of data (two phantoms) no experimentally significant degradation in SNR or line in k-space was seen. Images were acquired with the coil axis both parallel and perpendicular to the radiation for both phantoms and in each case no degradation in SNR or line in k-space could be seen. The results of the SNR measurements are shown in Table 5.1 (rectangular cuboid phantom), and in Table 5.2 (gel phantom) for the orientation in which the coil axis is along the radiation axis. Similar numbers were obtained for the case where the coils were oriented perpendicular to the incident radiation.

Table 5.1 Measured SNR values of MRI images of a rectangular cuboid phantom for three scenarios of linac operation.

Linac off	Linac on, lead blocking radiation	Linac on, radiation hitting coil
40	40	39
40	39	39
42	39	40
39	40	40
39	38	41
40	41	38
39	40	39
38	40	41
39	40	38
39	39	39

Table 5.2 Measured SNR values of MRI images of a gel phantom for three scenarios of linac operation.

Linac off	Linac on, lead blocking radiation	Linac on, radiation hitting coil
15	15	15
14	15	15
15	15	15
15	15	14
15	15	15
15	14	15
15	16	15
15	15	15
15	15	15
15	15	15

Finally images of the two phantoms were taken with insufficient RF shielding (images acquired before our RF shielding was complete) in order to illustrate how the RF manifests itself in the MRI data. The k-space data of these images is shown in Figure 5.9. On the left is the data with the right rectangular prism phantom and on the right is the data with the gel phantom.

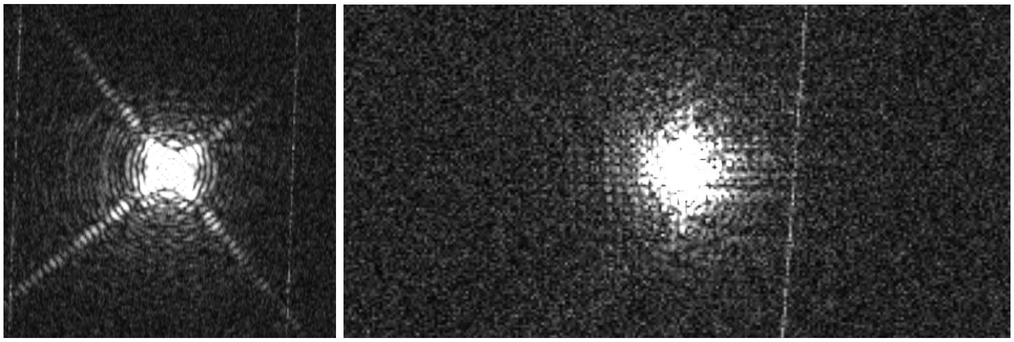

Figure 5.9: k-space data of the first (left) and second (right) phantoms taken during linac pulsing while the RF shielding was insufficient. The data illustrates a “line” in k-space from the RF picked up by the MRI coil.

5.5 Discussion

A linac-MRI prototype system has been constructed with the appropriate RF filters, RF cage and shielding which enables the acquisition of MR images while a 6 MV linac produces radiation; an overview of the system setup is shown in Figure 5.1. With the exception of the size of the RF cage the prototype system is setup as it would be in a clinical setting, thus allowing all possible problems to be investigated. One of the possible problems associated with the integration of a linac with an MRI is RF interference. A linac produces broadband RF noise [Burke et al. 2009] which is potentially problematic for the acquisition of MR images. A linac produces pulse trains that result in a “line” of interference in the k-space data when incomplete or improper RF shielding exists. The two plots shown in Figure 5.9 illustrate this line in k-space. The slope of this line will depend on the relationship between the radiation pulse rate and the time between adjacent read lines in k-space (TR). A 10 kHz acquisition bandwidth and 256 points in the read direction were chosen in order to ensure that the linac was pulsing at least once during MRI data acquisition interval (25.6 ms). To allow full independence between MRI acquisition timings and radiation delivery no synchronization was performed between the linac and MRI resulting in random positioning of linac pulses in the k-space data. The SNR of acquired images with the MRI can be strongly affected when the RF shielding is insufficient as was seen in Fallone [Fallone et al. 2009].

When the linac is pulsing measured levels of RF power density external to the RF cage approach a 0.1 mW/m^2 while internal to the cage the measured RF power levels are much lower, as is shown in Figure 5.3.

Specific requirements govern the installation of an MRI in a clinical environment [Wlad 1992 and AAPM 1986]. Prior to MRI installation, typical specifications of SE for MRI are 90 dB (10 MHz) and 100 dB (> 10 MHz) for the magnetic field and 100 dB for the Electric field [Sobol 1992]. Pavlicek [Pavlicek et al. 1984] states that the SE is usually specified to be between 80 and 100 dB. Furthermore Sobol [Sobol 1992] also states that after complete MRI installation the shielding effectiveness may be reduced to about 50-60 dB. Figure 5.4 shows our SE with all cables for the linac and MRI attached. Our data illustrates that excellent SE can be achieved regardless of the increased number of feed through points needed for the linac (for example ion chamber and ion pump cables). Any apparent difference in SE, when comparing Figures 5.3 and 5.4, can be accounted for by the fact that when the linac is operating RF “sources” exist within the cage (for example the electron gun pulse cables) and the operation of the linac does not produce enough signal amplitude, and therefore dynamic range, to properly test the SE. It should be noted that the data obtained in Figures 5.3 and 5.4 use different measurement techniques, as described above.

The main objective of this section of the thesis is to illustrate that MR images can be taken while a linac produced radiation without deleterious effects of RF interference. The images shown in Figures 5.5 and 5.7 illustrate that no degradation in SNR of the image could be seen while a 6 MV linac produced radiation. During the acquisition of these images the radiation was blocked before reaching the imaging volume with a lead brick. This was done in order to separate two effects; the RF effect and a radiation induced conductivity effect [Burke et al. 2009b]. This radiation induced conductivity is the topic of a separate PhD thesis and will be reported upon elsewhere.

5.6 Conclusions

The work presented herein has illustrated that through appropriate shielding of the linac-MRI system no degradation in the SNR of acquired MR images could be seen during linac operation. Images of two separate phantoms showed no degradation in measured SNR when comparing images taken with and without the linac pulsing and all other variables being held constant. Furthermore no artefacts could be seen in the acquired k-space data. Thus, MR images can be acquired during linac irradiation without synchronization provided appropriate RF shielding measures have been taken.

5.7 References

AAPM report 20. “Site planning for magnetic resonance imaging systems” NMR task group no. 2 1986.

Brabbins D., Martinez A., Yan D. et al. “A Dose Escalation Trial with the Adaptive Radiotherapy Process as a Delivery System in Localized Prostate Cancer: Analysis of Chronic Toxicity” Int. J. Radiat. Oncol. Biol. Phys. **61** 400-408 2005.

Brown J. “A Ham’s guide to RFI, Ferrites, Baluns and Audio interfacing” Revision 3, Audio Systems Group Inc. http://audiosystemsgroup.com 2008.

Bucci M. K., Bevan A. ans Roach M. “Advances in Radiation Therapy: Conventional to 3D, to IMRT, to 4D and Beyond” A. Cancer. J. Clin. **55** 117-134 2005.

Burke B., Lamey M., Rathee S., Murray B. and Fallone B.G. “Radio frequency noise from clinical linear accelerators” Phys. Med. Biol. **54** 2483-2492 2009.

Burke B., Rathee S. and Fallone B. G. “Radiation induced effects in an 8.5 MHz magnetic resonance imaging coil” Med. Phys. **36** 2495 2009b.

Dempsey J., Dionne B., Fitzsimmons J., Haghigat A., Li J., Low D., Mutic S., Palta J., Romeijn H., and Sjoden G. “A real-time MRI guided external beam radiotherapy delivery system” Med. Phys. **33** 2254 2006.

Eisbruch A., Dawson L. A., Kim H. M. et al. “Conformal and Intensity Modulated Irradiation of Head and Neck Cancer: the Potential for Improved Target Irradiation, Salvary Gland Function and Quality of Life” Acta.

Otorhinolaryngol Belg. 53 271-275 1999.

Erridge S.C, Seppenwoolde Y., Muller S.H., van Herk M., De Jaeger K., Belderbos J.S.A., Boersma L.J., Lebesque J.V. “Portal imaging to assess set-up errors, tumor motion and tumor shrinkage during conformal radiotherapy of non-small cell lung cancer” Radiother. Oncol. **66** 75-85 2003.

Fallone B.G., Murray B., Rathee S., Stanescu T., Steciw S., Vidokovic S., Blosser E. and Tymofichuk D. “First MR images obtained during megavoltage photon irradiation from a prototype linac-MR system” Med. Phys. **36** 2084-2088 2009.

Ghilezan M., Yan D., Liand J. et al. “Online Image-Guided Intensity-modulated Radiotherapy for Prostate Cancer: How Much Improvement can we Expect? A Theoretical Assessment of Clinical Benefits and Potential Dose Escalation by Improving Precision and Accuracy of Radiation Delivery” Int. J. Radiat. Oncol. Biol. Phys. 60 1602-1610 2004.

Hansen E.K., Bucci M.K., Quivey J.M, Weinberg V. and Xia P. Repeat CT imaging and replanning during the course of IMRT for head-and-neck cancer” Int. J. Radiat. Oncol. Biol. Phys. **64** 355-362 2006.

IEEE Electromagnetic compatibility committee “IEEE Standard Method for Measuring the Effectiveness of Electromagnetic Shielding Enclosures” IEEE std. 299. IEEE 3 Park Avenue New York 2006.

King R. W. P. “Transmission lines, antennas and waveguides” McGraw Hill Company Inc., New York 1945.

Kuo YC., Wu TH., Chung TS., Huang KW., Chao K.S.C., Su WC., Chiou JF.

"Effect of regression of enlarged neck lymph nodes on radiation doses received by parotid glands during intensity-modulated radiotherapy for head and neck cancer" Am. J. Clin. Oncol. **29** 600-605 2006.

Lagendijk J.J.W., Raaymakers B.W., Raaijmakers A.J.E., Overweg J., Brown K.J., Kerkhof E.M., van der Put R.W., Hårdemark., van Vulpen M. and van der Heide U.A. "MRI/linac integration" Radiother. Oncol. **86** 25-29 2008.

Langden K. and Jones D. "Organ motion and its management" Int. J. Rad. Oncol. Biol. Phys. **50** 265-278 2001.

Meyer J. L., Verhey L., Xia P. and Wong J. "New Technologies in the Radiotherapy Clinic" pages 1-17 from "IMRT-IGRT-SBRT Advances in the Treatment Planning and Delivery of Radiotherapy" Front. Radiat. Ther. Oncol. **40** 2007.

Pavlicek W. and Meaney T. F. "The special environmental needs of magnetic resonance" Appl. Radio. **13** 23-33 1984.

Pollack A., Zagars G. K., Starkschall G. et al. "Prostate Cancer Radiation Dose Response: Results of the MD Anderson Phase III Randomized Trial" Int. J. Radiat. Oncol. Biol. Phys. **53** 1097-1105 2002.

Rietzel E., Rosenthal S.J., Gierga D.P., Willet C.G., Chen G.T. "Moving Targets: Detection and Tracking of Internal Organ Motion for Treatment Planning and Patient Set-up" Radiother. Oncol. **73** S68-S72 2004.

Sobol W. "General site requirements including RF and magnetic shielding" from "The physics of magnetic resonance imaging" AAPM summer school Banff, Alberta 1992.

Webb S. “Motion effects in (intensity modulated) radiation therapy: a review” Phys. Med. Biol. **51** R403-R425 2006.

van Herk M. “Errors and Margins in Radiotherapy” Sem. Rad. Oncol. **14** 52-64 2004.

Verellen D., De Ridder M. and Storme G. “A (short) history of image-guided radiotherapy” Radiother. Oncol. **86** 4-13 2008.

Verellen D., De Ridder M., Linthout N., Tournel K., Soete G. and Storme G. “Innovations in Image-Guided Radiotherapy” Nature Rev. Cancer **7** 949-960 2007.

Wlad T. Sobol “General Site Requirements Including RF and Magnetic Shielding” from “The Physics of Magnetic Resonance Imaging” 1992 AAPM summer school, Banff, Alberta, conference proceedings 1992.

Chapter 6: Conclusions, Summary and Future Work

A prototype system which has integrated a linac with an MRI for real time image guided radiotherapy treatment has been successfully undertaken. Several possible problems associated with the integration were identified. The work presented in this thesis was concerned with the RF noise interference from the modulator of a linac to an MRI. The modulator of a linac is known to produce broadband RF noise and an MRI operates by transmitting and receiving signals in a particular RF band. Four distinct investigations were undertaken and presented as separate chapters.

In chapter 2 the effects on the field distribution of an elementary dipole antenna was simulated in a measurement room and in free space. The simulations were then compared to measurements taken by a fellow student as a part of a Masters thesis. The simulations and measurements we designed to determine the magnitude of the effect that an enclosed environment would have on the electric and magnetic field distribution of an RF source within a room. The linac and MRI will be housed together within an enclosed environment; the effect of the enclosed environment on the noise generated by the linac was studied. At higher frequencies, 400 and 500 MHz, our simulations and measurements showed that the strength of the H field was approximately doubled. While the simulations of the E field did not match the measurements very well the magnitude of the effect, an increase in field strength, was simulated. The E field was also found to also increase by up to a factor of 2.

The work presented in Chapter 3 focused on the RF noise generated by the

DC motors used to drive the MLCs used for IMRT or conformal radiotherapy. Measurements of the RF noise generated by two clinically currently used DC motors and one brushless fan motor were presented. The brushless fan motor was found to produce less noise; however, its performance suffered while being subjected to magnetic fields up to ~ 100 Gauss.

In the second part of the study one half of a Varian 52 leaf MLC was brought within the fringe field of the MRI in our linac-MRI system. While the linac was off images were taken with the MLC functioning and stationary. At 70 cm from the MRI center (coil location) there was a noticeable difference in the measured SNR when the MLC was functioning. However, the MLC and its associated cabling were shielded using a copper box, copper tape and aluminum foil. After shielding, images with the MLC near the MRI were repeated with the MLC stationary and functioning. This time no image degradation could be seen in the four possible MRI coil/MLC orientations. The study illustrated that when unshielded the RF noise produced by the MLC motors was sufficient to affect image quality, however, the MLC was successfully shielded such that no image degradation could be seen.

The work presented in Chapter 4 focused on the sources of RF noise from the modulator of a linac. It was known that the magnetron within the modulator produced RF noise. However, it was not known how much of the RF noise produced by the modulator of a linac could be attributed to the magnetron. A resistive load was used in place of the magnetron to determine production of RF from a magnetron. The RF noise generated by the modulator while it was pulsing was measured with the magnetron as a load. Then the magnetron was replaced by the resistive load and the RF noise was measured again. The difference in measured RF noise could be attributed to the magnetron. It was found that above ~ 65 MHz all of the noise generated by the modulator could be attributed to the magnetron. Some of the RF noise measured below 65 MHz could be attributed to the magnetron, however, at some frequencies below 65 MHz the source could not be identified with confidence.

Large currents exist on the PFN during discharge, since the coil could act as an antenna radiating RF, its operation was simulated. First the discharge of the PFN was modeled using an equivalent electrical circuit of the modulator of a linac using MultiSIM. The simulations were validated by measuring signal waveforms within the modulator. The simulated current along the PFN coil was then used as an input into a second simulation, COMSOL, which was used to determine the field strengths near the coil during discharge. It was shown that compared to the measurements, the simulated fields from the PFN coil were orders of magnitude smaller and could only possibly contribute at frequencies below 1 MHz.

The thyratron in the modulator produces large grid spikes, the possibility of these spikes being radiated as RF was investigated. A saturable reactor was used to block the grid spikes from directly entering the trigger and heater circuits. The RF noise was measured with the saturable reactors (one for each grid) in place and then again with normal operation (no SRs). The measurements showed that only a small gain in the measured RF noise in the frequency range 5 - 70 MHz was attained. The work illustrated that the grid spikes directly entering the trigger circuit and producing RF noise is unlikely. However, the work does not preclude other mechanisms, such as capacitive coupling, into other parts of the circuit where the spike could be radiated as RF.

The work presented in Chapter 5 focused on the shielding measurements and techniques used to successfully integrate a linac with an MRI, such that images could be acquired by the MRI while the linac operated. An RF cage is used to house the accelerator structure of the linac and the MRI. Measurements of the RF noise generated while the linac pulsed were taken inside and outside the RF cage. The shielding effectiveness of the RF cage was measured using loop antennas for the H field and rod antennas for the E field. In the frequency range 1 – 50 MHz the measured SE for both the E and H fields was above the suggested values in the literature.

Images of two phantoms used to ascertain the shielding effectiveness of the RF cage were acquired with the linac functioning and quiescent. It was illustrated that there was no SNR image degradation while the linac operated. Furthermore, no effects in the k-space data could be seen.

In Chapter 3 we presented measurements of the RF noise production from DC motors. At lower frequencies the background subtracted noise power density spectrum showed an increase in error at lower frequencies, see Figure 3.8. This was a result of the dependence of the error on the performance factor, as illustrated by Equation 3.5. The measured signal from the loop probe could be improved by performing measurements with an antenna with increased number of turns. However, this would require a calibration of the performance factor. Other motors could be used to drive the leaves of an MLC. Piezoelectric motors are used in robotic surgery with MRI. The feasibility of the use of other motors could be investigated. To the author's knowledge no study has been performed on the longer term time dependence of a magnetic field on performance of DC motors. A study which included the long term RF noise, effects on leaf speed and power consumption could be performed. The work presented herein focused on the use of a magnetron as a source of the production of microwave power. The RF noise from a klystron could also be investigated and compared to the measurements presented in this work.

In chapter one motivation which discussed the need for improved soft tissue image guidance was presented. MRI provides images of exquisite soft tissue contrast. Improvements in the localization of the clinical target volume and organs at risk enable reductions in the irradiated target volume. These reductions will enable dose escalation to the cancerous target volume thereby improving the treatment outcome probability and/or reductions of dose to healthy tissue, thereby improving patient quality of life. This work has illustrated that one of the problems, RF noise interference, associated with the integration of a linac with an MRI has been resolved such that MR images can be acquired with no signal degradation while a 6 MV linac produced radiation. Furthermore the work herein has illustrated that any RF problems associated with the use of an MLC near an MRI can be resolved.

Appendix A: Antenna Theory

A.1 Introduction

An antenna is defined as a device which converts RF input power into electromagnetic radiation, or conversely, intercepts electromagnetic radiation and converts it into an RF voltage across feed points. In general any conductor which can either intercept an RF field or allow an RF current to flow in it can be an antenna. The field of electromagnetics is governed by Maxwell's Equations (A.1 - A.4) and the Lorentz force law (A.5).

$$\vec{\nabla} \times \vec{E} = -\frac{\partial \vec{B}}{\partial t} \qquad \text{(A.1)}$$

$$\vec{\nabla} \times \vec{H} = \frac{\partial}{\partial t}\vec{D} + \vec{J} \qquad \text{(A.2)}$$

$$\vec{\nabla} \cdot \vec{D} = \rho \qquad \text{(A.3)}$$

$$\vec{\nabla} \cdot \vec{H} = 0 \qquad \text{(A.4)}$$

The solution to Maxwell's equations for radiation from antennas consists of solving for the fields that are created by a current distribution $\vec{J}$. Equations (A.4) and (A.1) enable the introduction of the vector, $\vec{A}$, and scalar, Φ, potentials [Jackson 1999], which are related to the E and B fields by:

$$\vec{H} = \vec{\nabla} \times \vec{A} \qquad \text{(A.5)}$$

$$\vec{E} = -j\omega\mu\vec{A} - \vec{\nabla}\Phi \qquad \text{(A.6)}$$

After expressing the $\vec{E}$ and $\vec{H}$ fields in terms of these scalar fields and upon imposing the Lorentz gauge ($\nabla \cdot A = -j\omega\varepsilon'\Phi$) one arrives at the vector wave equation:

$$\nabla^2 \vec{A} + \omega^2 \mu\varepsilon' \vec{A} = -\vec{J} \qquad \text{(A.7)}$$

Where $\varepsilon' = \varepsilon - j(\sigma/\omega)$, ε is the permittivity, σ is the conductivity and ω is the radian frequency. Equation (A.7) can be solved for the vector potential $\vec{A}$ once the current $\vec{J}$ has been specified. The $\vec{E}$ field can also be related to the vector potential:

$$\vec{E} = -j\omega\mu\vec{A} + \frac{\vec{\nabla}(\vec{\nabla}\cdot\vec{A})}{j\omega\varepsilon'} \qquad \text{(A.8)}$$

for the arbitrary current distribution shown in Figure A.1.

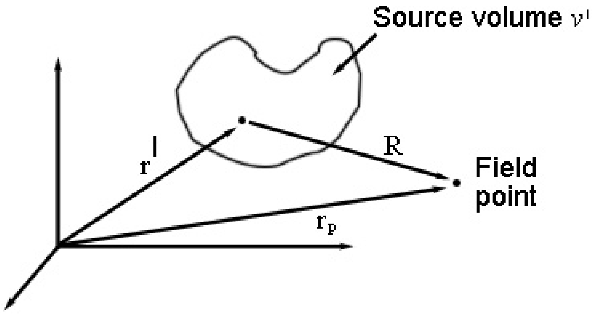

Figure A.1: General definition of the setup of a arbitrary current distribution.

Stutzman [Stutzman 1981] gives the solution to Equation (A.7) for the vector potential as:

$$\vec{A} = \iiint_{v'} \vec{J}\,\frac{e^{-j\beta R}}{4\pi R}\,dv' \qquad \text{(A.9)}$$

The fields from an antenna are then determined as follows: determine or assume a current distribution $\vec{J}$ on an antenna, solve for the vector potential given in (A.9), use Equation (A.5) to solve for the $\vec{H}$ field, then use Equation (A.8) to solve for the $\vec{E}$ field.

A.2 Near Field Probes

Antennas come in many shapes and sizes, the discussion herein will be limited to those of interest to our research, the interested reader is directed to a few of the plethora of books devoted to antenna theory [Balanis 2005, Collin 1985, Kraus 1950 and Stutzman 1981]. These probes include an electric field “ball” probe and a loop probe. Schematic diagrams of the two probes are shown in Figure A.2.

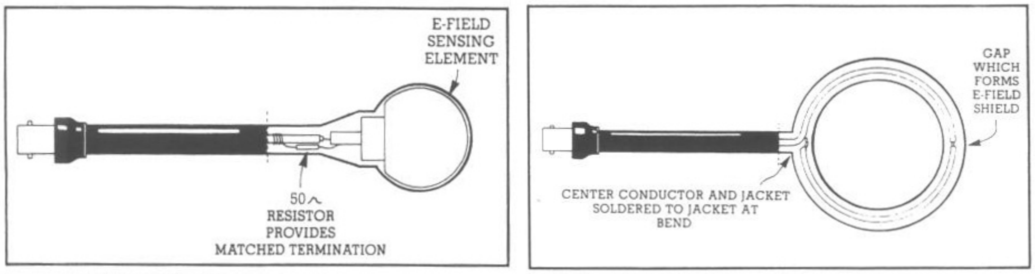

Figure A.2: The two main probes used in this work. The electric field probe (left) and the magnetic field probe (right) [© Rohde and Schwarz, 2009 with permission].

A description of the operation of the loop probe is given in King [King 1945]. The loop consists of a 50 Ω coaxial line which is looped around and whose center conductor and shield are then soldered to the shield at the start of the loop. The loop operates based upon Faraday’s law of induction which states [Jackson 1999] that the induced electromotive force, ε, in any closed circuit is equal to the time rate of change of magnetic flux, Φ, through the circuit. Mathematically this can be expressed as:

$$\varepsilon = -\frac{d\Phi}{dt}. \qquad \text{(A.10)}$$

The ingenious design of the loop probe involves the small gap in the shield as shown in Figure A.2. When the loop is placed in an electromagnetic field which has an electrical component along the same direction as the line which feeds the loop, then undesired equal and co-directional up and down currents are induced along the two sides of the loop. These currents can then induce equal and opposite currents in the wires feeding the probe (for example conductor and shield). If the probe is unsymmetrical these currents can lead to unwanted currents. However if the probe has a shield with structural symmetry as shown in Figure A.2, then the co-directional currents do not exist. Thus the gap acts as a balun to remove unwanted currents. With this setup the *H* field loop probe will reject the *E* field with up to 41dB of *H/E* rejection.

The *E* field probe is an insulator filled metallic semi sphere which has a 50 Ω resistor for matched termination. The inner conductor of the coaxial line extends into the insulator within the metallic semi sphere. The probe works on the basis of a capacitance between the coaxial inner conductor and the metallic semi sphere. An external *E* field will induce a charge on the semi sphere which is capacitively coupled to the inner conductor thus inducing a charge on it. Any *H* field pickup is rejected due to the fact that no closed loops exist. The *E* field ball probe will reject the *H* field with up to 30 dB of *E/H* rejection while the H field probe will reject the E field with 41 dB of rejection.

A.3 Performance Factors

Measurements conducted with an antenna or probe requires a calibration factor for the measured signal from the probe to the actual field strength value at the location of the probe. These conversion factors are known as antenna factors when the calibration is specifically done on an antenna (or probe) or performance factors when a batch of the geometrically equivalent antennas (or probes) is made and the same performance factor is used for all of the antennas (or probes). We used performance factors and will thus talk about the performance factor of a probe; the math is identical for antenna factors.

The relation between the performance factor (*PF*) and the actual field value (*Ψ*) is:

$$PF_{dB} = 20\log\left(\frac{\Psi}{V}\right) \qquad \text{(A.11)}$$

Where in our case *Ψ* will either be the electric (*E*) or magnetic (*H*) fields. And the subscript *dB* refers to the fact that performance factors are usually expressing in decibels. The performance factors for the two probes used throughout this thesis are shown in Figure A.3.

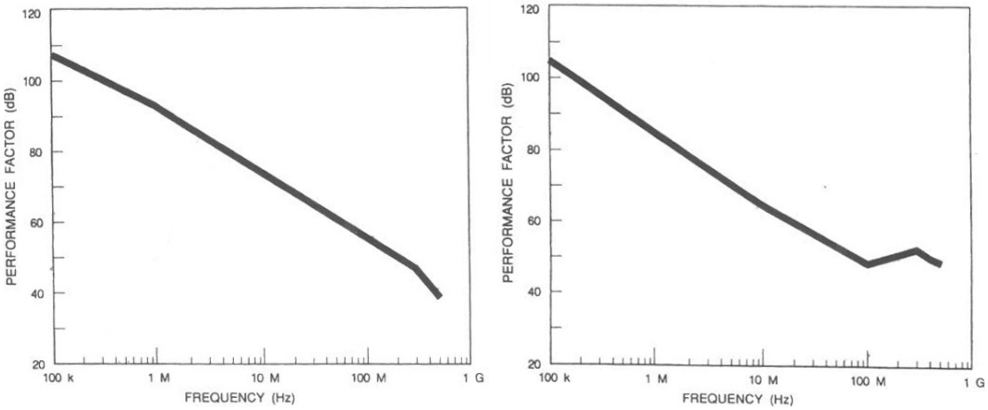

Figure A.3: Performance factors for the electric field probe (left) and the magnetic field probe (right). [© Rohde and Schwarz, 2009 with permission].

As a function of frequency the performance factors are:

$$PF(f) = 10^{\left(\frac{PF_{dB}}{20}\right)} \qquad \text{(A.12)}$$

Substitution of Equation (A.11) into (A.12) yields:

$$\Psi = PF(f)*V \qquad \text{(A.13)}$$

These relations were used to determine the field strength values from the measured signal.

A.4 Radiation Mechanism

In order to completely understand how an antenna works we must first understand the mechanism by which the fields are generated. Consider the lines of force shown in Figure A.4.

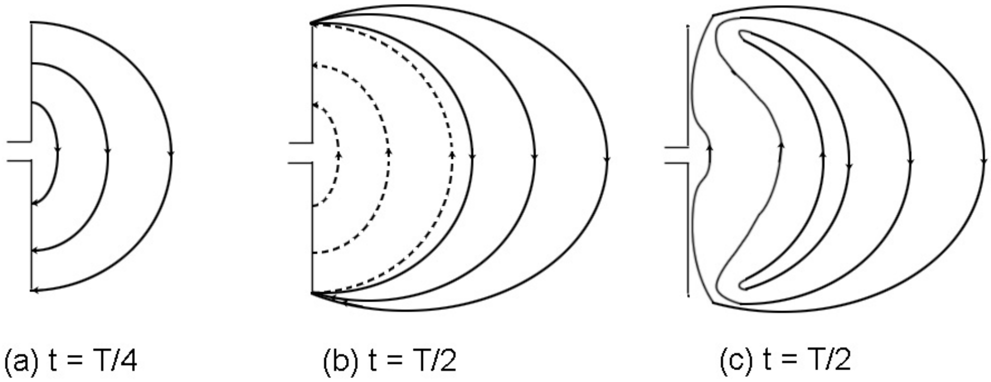

Figure A.4: The mechanism of radiation; the fields at specific times for an oscillating input for the E field.

Assuming a sinusoidal input current, Figure A.4 (a) shows the lines of force between the upper and lower poles of the dipole at maximum charge. During the next quarter period the lines of force created during the first quarter period travel λ/4 away from the dipole. In order for the total charge on the dipole to vanish at the end of the first half cycle, we can think of the lines of force in the second quarter period as being created by an opposite charge to the first quarter cycle, these lines are shown dashed in Figure A.4 (b). Finally once again since there is no net charge at the end of the first half cycle the lines of force must detach themselves from the dipole as shown in Figure A.4 (c). The same process is repeated in the next half cycle and so on, in this way electric patters we observe are created.

A.5 Field Regions

The nature of the electromagnetic fields surrounding an antenna allows its description to be broken up into three distinct regions: (1) reactive near field, (2) radiating near field (Fresnel region) and (3) far-field (Fraunhofer).

A.5.1 Reactive Near Field

The IEEE definition of the reactive near field is “That portion of the near-field region immediately surrounding the antenna, wherein the reactive field dominates.” The term “reactive” appears due to the fact that for non-resonant antennas, reactive power circulates between the reactive near field and the source. In this region the energy decays very rapidly with distance. Beyond the radiation term, which varies as $1/r^2$, the complex Poynting vector field contains imaginary terms indicative of reactive power. These imaginary terms, of order r^{-3} and higher, associated with the reactive near field, lead to stored energy. Physically the antenna input impedance is, in general, complex. Neglecting ohmic losses on the antenna structure, the real part of this input impedance represents radiation. The reactive near field power is associated with the imaginary part of the input impedance.

In the reactive near field the relationship between E and H becomes very complex due to the fact that the free space impedance is no longer constant. Beyond this, all four polarization types (horizontal, vertical, circular, or elliptical) can be present in the reactive near field; this is unlike the far-field in which one polarization usually dominates. The outer region of the reactive near field is commonly taken to be at a distance of $R \leq 0.62(D^3/\lambda)^{1/2}$ where λ is the wavelength and D is the largest dimension of the antenna.

A.5.2 Radiating Near-Field

The Radiating near field is "that portion of the near field region of an antenna between the far field and the reactive portion of the near field region, wherein the angular field distribution is dependent upon distance from the antenna." Generally the inner boundary is taken to be a distance of $R \geq 0.62(D^3/\lambda)^{1/2}$ and the outer boundary is taken to be $R < 2D^2/\lambda$. Electrically small antennas, antennas whose largest dimension is small compared to the wavelength, may not have a radiating near field region.

A.5.3 Far Field

The far field region is "That region of the field of an antenna where the angular field distribution is essentially independent of the distance from a specified point in the antenna region." This region is also referred to as the Fraunhofer region (since the physics governing the region is analogous to Fraunhofer diffraction; interference of plane waves in optics).

In the far field region the wave appears to an observer to be a plane wave. The definition of the far field region is where the parallel ray approximation (path length deviation is a sixteenth of the wavelength) begins to break down. Under this condition we have:

$$r > \frac{2D^2}{\lambda} \qquad r >> D \qquad r >> \lambda \tag{A.14}$$

Where once again D is the largest dimension of the antenna. In the high frequency region (3-30 MHz) and below (or regions where the antenna is small compared to the wavelength) the far field may have to be much greater than the first criterion above in order for the second and third criteria to be satisfied.

A.6 Fields from a Dipole Antenna

In chapter 2 the fields from a dipole antenna are both measured and simulated. The procedure for the calculation of the fields from a dipole antenna is as outlined in the end of section A.1. A sinusoidal current distribution is assumed on the dipole and the vector potential is solved for. This integration involves complicated integrals therefore only the result will be given here. Derivation of the fields is given in the first edition of Balanis [Balanis 2005]. The arrangement of the dipole antenna is shown in Figure A.5.

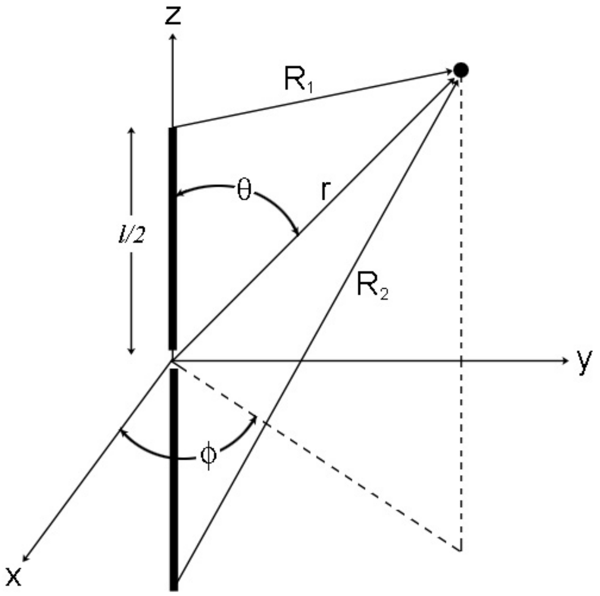

Figure A.5: Geometry used to determine the near fields from a dipole antenna.

With this geometry the fields are:

$$H_{\phi} = -\frac{I_0}{4\pi j}\frac{1}{y}\left[e^{-jkR_1}+e^{-jkR_2}-2\cos\left(\frac{kl}{2}\right)e^{-jkr}\right] \qquad \text{(A.15)}$$

$$E_{\rho} = j\frac{\eta I_0}{4\pi y}\left[\left(z-\frac{l}{2}\right)\frac{e^{-jkR_1}}{R_1}+\left(z+\frac{l}{2}\right)\frac{e^{-jkR_2}}{R_2}-2z\cos\left(\frac{kl}{2}\right)\frac{e^{-jkr}}{r}\right] \qquad \text{(A.16)}$$

$$E_{z} = -j\frac{\eta I_0}{4\pi}\left[\frac{e^{-jkR_1}}{R_1}+\frac{e^{-jkR_2}}{R_2}-2\cos\left(\frac{kl}{2}\right)\frac{e^{-jkr}}{r}\right] \qquad \text{(A.17)}$$

Where:

$$\begin{aligned} r &= \sqrt{x^2+y^2+z^2} = \sqrt{\rho^2+z^2} \\ R_1 &= \sqrt{x^2+y^2+\left(z-\frac{l}{2}\right)^2} = \sqrt{\rho^2+\left(z-\frac{l}{2}\right)^2} \\ R_2 &= \sqrt{x^2+y^2+\left(z+\frac{l}{2}\right)^2} = \sqrt{\rho^2+\left(z+\frac{l}{2}\right)^2} \end{aligned} \qquad \text{(A.18)}$$

A.6 Antenna Parameters

The radiation properties of an antenna are described by the antennas radiation pattern. According to the IEEE standards the radiation pattern is “The spatial distribution of a quantity which characterizes the electromagnetic field generated by an antenna”. Generally the pattern is normalized to the maximum value of power radiated at a given distance from the source. This pattern is observed in 2-D or 3-D and generally on a decibel scale. An example of such a pattern is shown in Figure A.6.

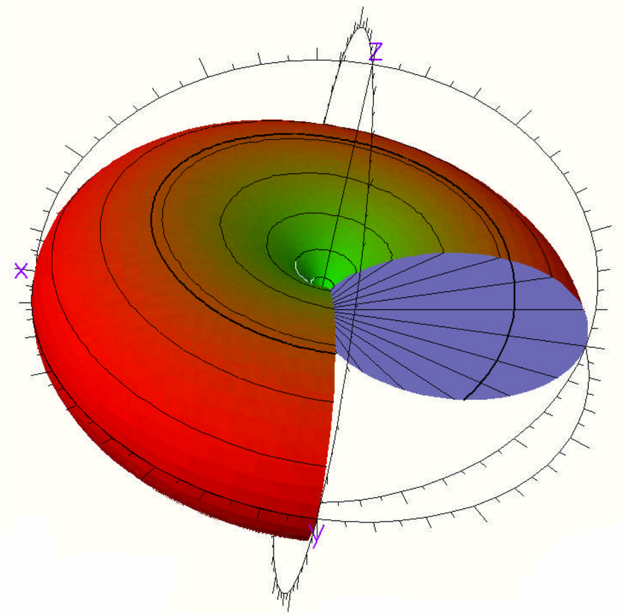

Figure A.6: Dipole radiation pattern for a dipole oriented along the z-axis shown.

The pattern itself represents the radiated power density in the far field region. Specifically it is a plot of the real part of the radial component of the Poynting vector, *W*.

$$W(\theta,\varphi) = \frac{1}{2}\left(\left[\vec{E}(\theta,\varphi) \times \vec{H}^*(\theta,\varphi)\right] \bullet \hat{a}_R\right) \tag{A.19}$$

Where $\hat{a}_R$ is the radial unit vector and $\vec{H}^*$ is the complex conjugate of the $\vec{H}$ field.

A.6.1 Input Impedance

The input impedance of an antenna is defined as [IEEE 1981 and IEEE 1991] “the impedance presented by an antenna at its terminals or the ratio of the voltage to current at a pair of terminals or the ratio of the appropriate components of the electric to magnetic fields at a point.” The impedance itself generally consists of resistive and reactive components. The resistive component represents dissipation generally in the form of ohmic heat loss on the antenna or radiation. The input reactance represents power stored in the near field of the antenna. Ideally a system is designed such that the power transfer to the antenna is maximized. It is well known that power transfer is maximized when the input impedance of the antenna is the complex conjugate of the transmission line's impedance. Thus the efficiency of an antenna to accept power from its source is governed by the input impedance the antenna presents. The complex reflection coefficient, Γ, is defined as:

$$\Gamma = \frac{Z_{in} - Z_0}{Z_{in} + Z_0} \tag{A.20}$$

Where Z_{in} is the input impedance of the antenna and Z_0 is the characteristic impedance of the transmission line used to transmit the power to the antenna. The reflected power is then:

$$P_{reflected} = P_{forward}\Gamma^2 \tag{A.21}$$

The power accepted by the antenna is given by:

$$P_{input} = P_{forward}(1 - \Gamma^2) \qquad \text{(A.22)}$$

Optimal impedance matching of an antenna to the transmission line only ensures that half of the power supplied is radiated. If the antenna is lossless and matched to the transmission line, half of the power supplied by the generator is dissipated as heat in the generator. Furthermore if the transmission line is lossy the available power to be radiated away by the antenna is reduced. If the antenna is lossy, power accepted by the antenna is split between heat dissipated in the antenna and radiated power.

A.6.2 Antenna Efficiency and Radiation Efficiency

The radiation efficiency is defined as [IEEE 1983 and IEEE 1991] “the ratio of the total power radiated by an antenna to the net power accepted by the antenna from the connected transmitter.” The antenna efficiency is a parameter which describes the losses at the input terminals and within the antenna structure itself. Power can either be dissipated in the form of heat via conduction and dielectric losses or lost in the form of reflections at the input terminal. The radiation efficiency involves the power radiated away from the antenna which is not lost in the form of heat. The antenna efficiency involves both the radiation efficiency and the reflection losses.

$$e = e_{ref} e_{rad} \qquad \text{(A.23)}$$

Where e is the antenna efficiency and e_{rad} is the radiation efficiency, e_{ref} is the reflection efficiency given by (1- Γ^2). Γ is the voltage reflection coefficient at the input terminals of the antenna as defined previously.

Rather than the reflection efficiency e_{ref} or reflection coefficient Γ, the quality of the impedance match at the terminals is generally given in terms of the Voltage Standing Wave Ratio or *VSWR*.

$$VSWR = \frac{1 + |\Gamma|}{1 - |\Gamma|} \tag{A.24}$$

The *VSWR* ranges from 1 to infinity, 1 being a perfect match and infinity being perfect reflection. High *VSWR* results in large reflections and high currents and voltages on the transmission line.

A.6.3 Directivity

The radiation pattern of an antenna, particularly the one shown in Figure A.6, can consist of many lobes. These lobes are directions in space in which the power density is peaked; antennas do not radiate power equally in all directions of space. According to the IEEE standard definitions and terms for antennas the directivity of an antenna is defined as [IEEE 1981 and IEEE 1983] "the ratio of the radiation intensity in a given direction from the antenna to the radiation intensity averaged over all directions. The average radiation intensity is equal to the total power radiated by the antenna divided by 4π. If the direction is not specified, the direction of maximum radiation intensity is implied". The directivity of an antenna is controlled only by the pattern; it is not dependent on antenna loss or mismatch. Mathematically this can be expressed as:

$$D = \frac{4\pi U}{P_{Rad}} \tag{A.25}$$

Where D is the directivity, U the radiation intensity (W/unit solid angle) and P_{Rad} is the total radiated power (W). An isotropic source, a hypothetical quantity, would have a directivity of 1. The directivity therefore gives an impression of the directional property of an antenna.

A.6.4 Gain

Gain is a quantity which is related to the directivity of an antenna, it however takes into account the efficiency of an antenna. According to the IEEE gain is defined as "the ratio of the intensity, in a given direction, to the radiation intensity that would be obtained if the power accepted by the antenna were radiated isotropically. The radiation intensity corresponding to the isotropically radiated power equal to the power accepted (input) by the antenna divided by 4π." The gain can be expressed as:

$$G = 4\pi \frac{U(\theta,\varphi)}{P_{in}} = e_{Rad} D(\theta,\varphi) \qquad \text{(A.26)}$$

Where G is the gain, P_{in} is the power accepted by the antenna and as defined previously U is the radiation intensity, e_{Rad} is the radiation efficiency and D is the directivity. It should be highlighted that gain is dependant on the power accepted by the antenna not the power sent to the antenna. Generally due to mismatch at the antenna input terminals not all power sent to the antenna is accepted. Thus gain does not take into account reflection losses when the antenna is connected to a transmission line.

A.6.5 Polarization

The electromagnetic fields radiated by an antenna are vector quantities and generally have some polarization. The polarization of an antenna is the polarization of the radiation emitted by the antenna.

It is important to understand that power received by an antenna can be affected by the orientation of the antenna. Polarization of radiation or of a receive antenna results in a polarization loss factor (PLF) defined as:

$$PLF = \left|\hat{p}_i \cdot \hat{p}_r\right|^2 = \cos(\varphi_p)^2 \tag{A.27}$$

Where $\hat{p}_i$ and $\hat{p}_r$ are the polarization unit vectors of the incoming wave and the receive antenna, φ_p is the angle between the two unit vectors. One need not concern themselves with the polarization loss factor as long as the receive antenna is rotated for maximum signal, when the polarizations of the incoming wave and antenna are aligned the PLF is one.

A.6.6 Friis Transmission Formula

For the setup shown in Figure A.7, the Friis transmission formula relates the power received by one antenna to the power transmitted by a second antenna, when the antennas under consideration are separated by at least $R > 2L^2/\lambda$, where L is the largest dimension of either antenna. However the error is only a few percent if the distance, R, becomes comparable to $2D^2/\lambda$ [Kraus 1950].

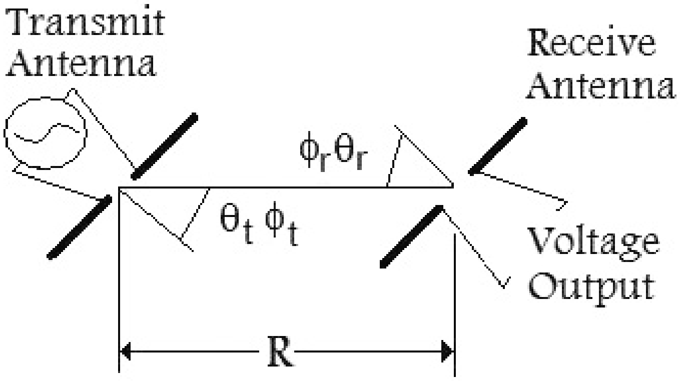

Figure A.7: Setup of transmitting and receiving antennas for consideration of the Friis transmission formula.

The formula itself is derived in Balanis [Balanis 2005]; the result will simply be stated here:

$$\frac{P_r}{P_t} = e_r e_t \frac{\lambda^2 D_t(\theta_t,\varphi_t) D_r(\theta_r,\varphi_r)}{(4\pi R)^2} = \left(\frac{\lambda}{4\pi R}\right)^2 G_t G_r \qquad \text{(A.28)}$$

Where P_r and P_t are the power delivered to the receiver load and the input power into the transmit antenna, e_r and e_t are the receive and transmit antenna efficiencies, $D_t(\theta_t,\varphi_t)$ and $D_r(\theta_r,\varphi_r)$ are the directivities of the receive and transmit antennas with the angles illustrated in Figure A.6 (with one of the angles being out of the page), R is the distance between the antennas. G_r and G_t are the receive and transmit antenna gains.

The formula assumes that the antennas are matched to their transmission lines or loads and that the antennas are oriented such that the polarization of the antennas produces maximum signal. If the antennas are not matched to their respective transmission lines the factors $(1-|\Gamma_t|^2)$ and $(1-|\Gamma_r|^2)$ must be included in order to account for the reflection losses. Finally it also assumes free space; if ground reflection exists the above power transfer ratio may lie between four times the value given above and zero [Kraus 1950].

A.7 References

Balanis C. “Antenna Theory” John Wiley and Sons Inc., New Jersey 2005.

Collin R. E. “Antennas and Radio wave Propagation” McGraw Hill Book Company, New York, 1985.

IEEE Antenna Standards Committee “IEEE Standard Methods for Measuring Electromagnetic Field Strength of Sinusoidal Continuous Waves, 30 Hz to 30 GHz” IEEE inc. 1991.

IEEE Antenna Standards Committee “IEEE Standard Definitions of Terms for Antennas IEEE” inc. 1983.

IEEE Antenna Standards Committee “IEEE Standard Test Procedures for Antennas” IEEE inc. 1979

Jackson J. D. “Classical electrodynamics” John Wiley and Sons pp 239-240 1999.

King R. W. P. “Transmission lines, antennas and waveguides” McGraw Hill Company Inc. New York 1945.

Kraus J. D. “Antennas” McGraw Hill, New York, 1950.

McLean J., Sutton R. and Hoffman R. “Interpreting Antenna Performance Parameters for EMC Applications: Part 1: Radiation Efficiency and Input Impedance Match” TDK RF solutions.

McLean J., Sutton R. and Hoffman R. “Interpreting Antenna Performance Parameters for EMC Applications: Part 2: Radiation Pattern, Gain and Directivity” TDK RF solutions.

McLean J., Sutton R. and Hoffman R. “Interpreting Antenna Performance Parameters for EMC Applications: Part 3: Antenna Factor” TDK RF solutions.

OSHA_internet http://www.osha.gov/SLTC/radiofrequencyradiation/electromagnetic_fieldmemo/\\electromagnetic.html\#Section\%206 visited August 22nd 2007.

Stutzman W. L. and Thiele G. A. “Antenna theory and design” John Wiley and Sons Inc. 1981.

Appendix B: TLM Theory

B.1 Basic Building Blocks

The work presented in section 2.2.1 provided an introduction to the TLM method. The following discussion follows that given by Hofer [Hofer 1989]. A transmission line itself consists of either parallel conductors or coaxial conductors. The model is visualized as a pair of parallel lines intersecting as shown in Figure B.1 (A).

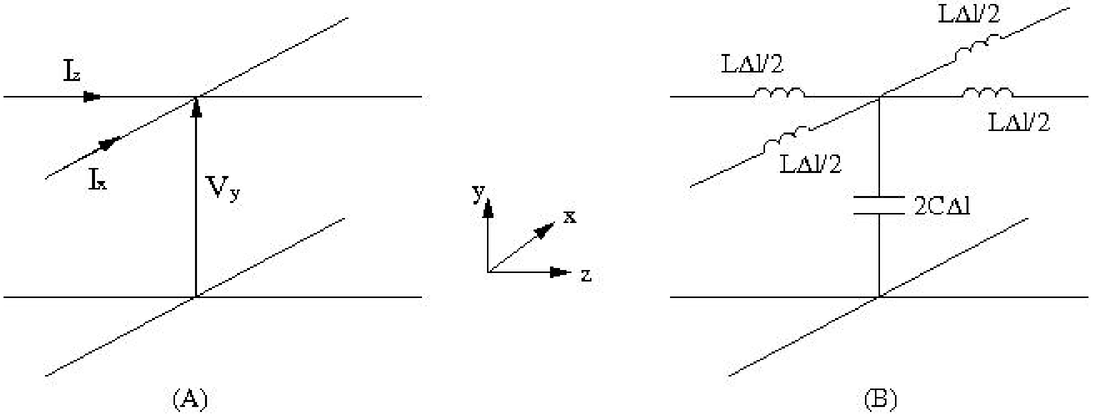

Figure B.1: Building block of the two-dimensional TLM model. (A) Shunt node; (B) equivalent lumped element.

The basic node shown in Figure B.1 (A) is known as the shunt node. In general a shunt is a relief valve or diverter. In electronics a shunt allows the passage of current from one part of a circuit to another. Figure B.1(A) should then be visualized as two parallel conductors (one transmission line) crossing each other.

The shunt node is the basic building block for the TLM method. The shunt building block consists of a line in which the inductance and resistance are distributed homogeneously along the line and the capacitance was distributed between the conductors. Computer modeling of such a system is quite difficult [DeCogan 2006]; therefore a lumped equivalent model is used instead. This model is shown in Figure B.1(B). The capacitance is twice that of an individual line section and the resistance and inductance of half that of an individual line section due to the parallel connection of the node.

B.2 Wave Characteristics

If the node separation *Δl* is small compared to the wavelength then the voltage and current changes from one node to the next in the x and z directions are [Hofer 1989]:

$$\frac{\partial V_y}{\partial x} = -L\frac{\partial I_x}{\partial t} \qquad \frac{\partial V_z}{\partial x} = -L\frac{\partial I_z}{\partial t} \qquad \frac{\partial I_z}{\partial z} + \frac{\partial I_x}{\partial x} = -2C\frac{\partial V_y}{\partial t} \qquad \text{(B.1)}$$

These expressions can be combined (differentiate the expressions in order as shown with respect to x, z and t respectively then substitute cross terms) to yield the two-dimensional wave equation:

$$\frac{\partial^2 V_y}{\partial x^2} + \frac{\partial^2 V_y}{\partial z^2} = 2LC\,\frac{\partial^2 V_y}{\partial t^2} \qquad \text{(B.2)}$$

This illustrates that the two-dimensional TLM network can simulate anything in which the two-dimensional wave equation can be used to solve. The relationship between the voltage and current on the transmission line and the Electric and Magnetic fields can be seen if we compare to the expansions for Maxwell's equations for $\partial/\partial y = 0$ and $E_x = E_z = H_y = 0$ (which are the TE_{n0} modes in a rectangular waveguide):

$$\frac{\partial E_y}{\partial x} = -\mu \frac{\partial H_z}{\partial t} \qquad \frac{\partial E_y}{\partial z} = +\mu \frac{\partial H_x}{\partial t} \qquad \frac{\partial H_x}{\partial z} - \frac{\partial H_z}{\partial x} = \varepsilon \frac{\partial E_y}{\partial t} \tag{B.3}$$

and

$$\frac{\partial^2 E_y}{\partial x^2} + \frac{\partial^2 E_y}{\partial z^2} = \mu\varepsilon \frac{\partial^2 E_y}{\partial t^2} \tag{B.4}$$

we can thus see that the following equivalences exist between field and TLM quantities:

$$E_y \equiv V_y \qquad H_z \equiv I_x \qquad H_x \equiv -I_z \qquad \mu \equiv L \qquad \varepsilon \equiv 2C \tag{B.5}$$

Thus we see how the TLM model can be used to determine the Electric and Magnetic fields given some initial input pulse. It should also be noted that the relationship between the current and voltage on a line and the field quantities depends on the problem being solved. For example currents on the line can represent either the Electric or Magnetic field. It should be noted that the velocity term in equation B.2 is $(2LC)^{-1/2} = c(2)^{-1/2}$. This means that the propagation velocity is $(2)^{-1/2}$ times smaller than that of the speed of light. Once the fields are known as a function of time a FFT analysis can determine the strengths of the fields in the frequency domain.

B.3 Series Connected TLM Network

Transmission lines in space can also be modeled as being a series connected mesh as shown in Figure B.2.

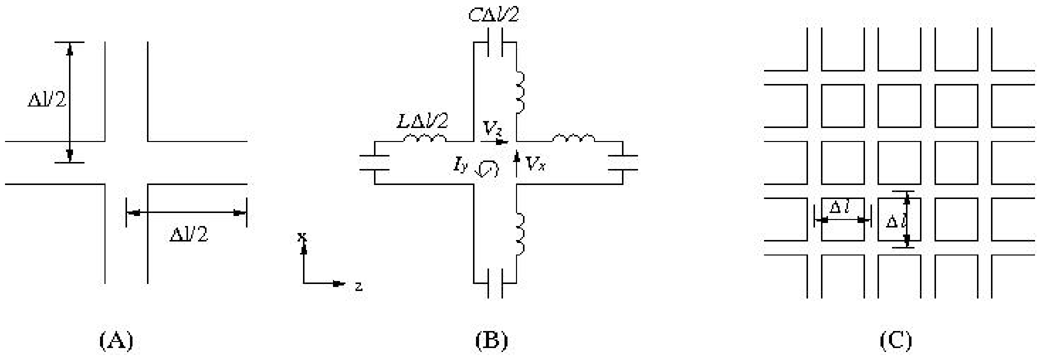

Figure B.2: The series node and the 2-D series network. (A) Series node; (B) equivalent series element; (C) two-dimensional series mesh.

Following the same procedure as in the case of the shunt node it can be shown that the voltage scattering at a node is given by:

$$ {}_{k+1}\begin{pmatrix} V_1 \\ V_2 \\ V_3 \\ V_4 \end{pmatrix}^r = \frac{1}{2}\begin{pmatrix} 1 & 1 & 1 & -1 \\ 1 & 1 & -1 & 1 \\ 1 & -1 & 1 & 1 \\ -1 & 1 & 1 & 1 \end{pmatrix} \cdot {}_{k}\begin{pmatrix} V_1 \\ V_2 \\ V_3 \\ V_4 \end{pmatrix}^i \qquad \text{(B.6)} $$

Two things should be pointed out here; if a two-dimensional grid is built up by series nodes then the permeability simulated is double that of free space and in order to model in three dimensions both the series and shunt nodes are required.

B.4 Modeling Lossy and Lossless boundaries

Due to the equivalence between the fields and the voltage and current boundaries can be modeled by assigning a suitable reflection coefficient at a node. The value of the reflection coefficient of course depends on the nature of the boundary being simulated.

B.4.1 Lossless Boundaries

In the case of a shunt node simulating a lossless boundary, if the voltage is equivalent to the electric field and the current is equivalent to the magnetic field then; electric walls are simulated by a short circuit and magnetic walls are represented by an open circuit. However if the voltage simulates a magnetic field then a magnetic wall is represented by a short circuit and an electric wall is represented as an open circuit. It must always be the case that a wall is placed half way between node so that reflected impulses reach adjacent nodes at the same time as other pulses arriving at the node. Curved walls are approximated by piecewise straight elements.

If an open circuit is being modeled then the reflected pulse is sent with equal sign to the incoming pulse, if a short circuit is being modeled the reflected pulse has the opposite sign of the incident pulse. Generally electric and magnetic walls are use when a model possesses symmetry. A wall can cut the computation time of a simulation down.

B.4.2 Lossy Boundaries

If the boundary is lossy with a surface impedance given by Z_c then the boundary reflection coefficient is given by:

$$\rho = \frac{Z_c - Z_0}{Z_c + Z_0} \tag{B.7}$$

Where Z_0 is the characteristic impedance of the mesh lines.

B.5 Modeling Lossy and Lossless Materials

Lossless homogeneous materials can be modeled without any modification to the model as described thus far. However changes must be made in order to accommodate lossy materials, both homogeneous and inhomogeneous.

B.5.1 Lossy Homogeneous Materials

Losses in the mesh must be introduced in order to simulate a lossy material. Two ways in which this can be done are to introduce losses equally along the transmission line by introducing a factor, $e^{-\alpha \Delta l}$, or to introduce the losses at the nodes in the form of a lumped resistive element. In the first case α is the attenuation constant of the medium and in the second case energy is lost at the mesh nodes. For homogeneous materials introducing the losses equally along the line works well and for inhomogeneous materials using lumped losses at the nodes works well.

B.5.2 Lossy Inhomogeneous Materials

This is the most general case, the permittivity and permeability can vary across the structure of interest. In this case the nodes of the TLM mesh can be ``loaded" with additional reactive and dissipative elements consistent with the properties of the material. That is these additional elements are directly related to the material properties.

B.6 Three Dimensional TLM Method

As stated previously both shunt and series nodes are required for the three-dimensional TLM node. Such a node, known as the distributed node, is shown in Figure B.3. The name comes from the fact that the six field points are separated by a distance of *Δl/2*. The node itself consists of three series and three shunt nodes.

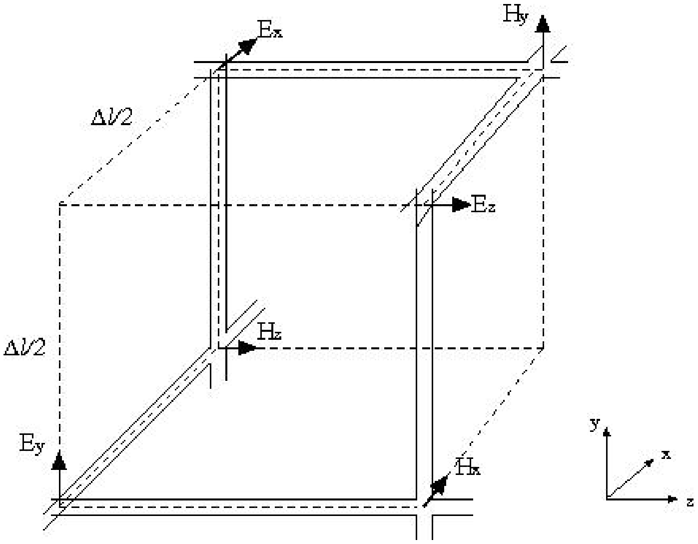

Figure B.3: The full three dimensional "unit cell" used for the three-dimensional TLM method, it consists of three shunt and three series nodes.

Because the three dimensional mesh is made up of the two-dimensional nodes described previously the numerical procedures which describe the scattering of pulses at the nodes are exactly the same.

The node generally used is the symmetrical condensed node; this node cannot be represented by an equivalent lumped element network.

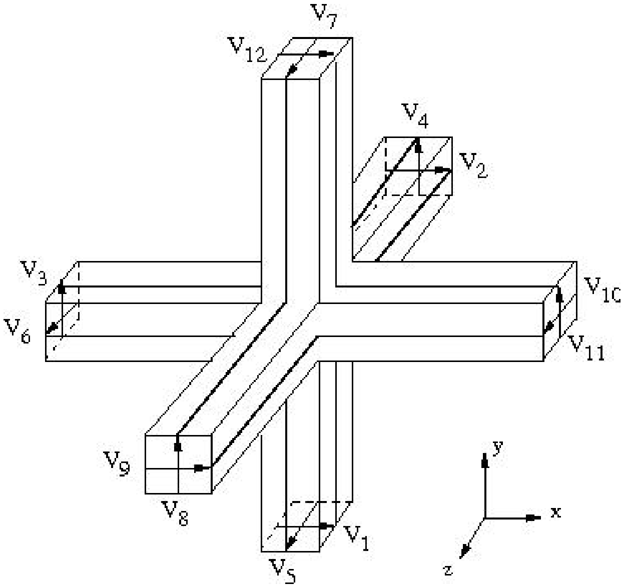

Figure B.4: The symmetrical condensed three-dimensional node, as described by Johns [Johns 1987].

An advantage of the symmetrically condensed node is that the misalignment error, described below, is not a problem. Furthermore, Allen [Allen et al. 1987] showed that the symmetrically condensed node is more accurate than other mesh types.

B.7 Errors Involved in the TLM Method

All numerical methods have some sort of errors involved, the main sources of error in the TLM method are:

1. The impulse response must be truncated in time.
2. The propagation velocity in the mesh depends on the frequency and direction of propagation.
3. The spatial resolution is limited by the finite mesh size.
4. Boundaries and dielectric interfaces are not aligned in the three-dimensional model when electric walls are place across shunt nodes.

B.7.1 Truncation Error

The above equations were all derived assuming a Dirac pulse. An infinite sum of continuous functions is needed in order to reproduce a discontinuous function. When approximating a discontinuous function the Gibbs phenomenon states that [Carslaw 1930] “the nth partial sum of the Fourier series has large oscillations near the jump, which might increase the maximum of the partial sum above that of the function itself. The overshoot does not die out as the frequency increases, but approaches a finite limit.” This error can be minimized by increasing the number of iterations and increasing the separation in the frequency domain between neighboring spectral peaks. Peaks in the frequency domain near the wanted mode can be separated by choosing the appropriate input and output points in the TLM network.

B.7.2 Velocity Error

As the ratio of the wavelength to the mesh parameter Δl decreases the velocity of pulse propagation becomes dispersive and depends on the direction of propagation. Like the coarseness error (to be discussed next), the velocity error can be reduced by ensuring the mesh size is much smaller than the wavelength. Beyond reducing the mesh size indefinitely dispersion relations can sometimes be used to correct for differences in velocity.

B.7.3 Coarseness Error

Coarseness error occurs when the mesh size is insufficient to properly resolve fields which vary rapidly or are highly non-uniform. The easiest way around such a problem is to generate a finer mesh, however such an approach is flawed since this can lead to simulation solve times which are unreasonable (especially when working in three-dimensions).

Generally the mesh size in possible "problematic" areas, such as corners, can be reduced locally. Another technique involves running multiple simulations while reducing the mesh parameter Δl and then extrapolating the results to $\Delta l = 0$.

B.7.4 Misalignments

In the three-dimensional TLM network dielectric interfaces are placed half-way between nodes while electric and magnetic walls are placed at the nodes. Thus at a flush interface between a dielectric wall and either a magnetic or electric wall there can be a slight misalignment of $\Delta l/2$. Generally this can be taken into account for by running the simulation with the dielectric both protruding and undercut and averaging the results. Or locally the mesh can be made fine enough such that the error caused by the slight misalignment is not significant.

The symmetrically condensed node of Figure B.4 does not suffer from the misalignment error and as such can be used so that the misalignment error does not occur.

B.8 References

Allen R., Mallik A. and Johns P. B. "Numerical results for the symmetrical condensed TLM node" IEEE Trans. Microwave Theory Tech. MTT-35 378-382 1987.

Carslaw H.S. "introduction to the theory of Fourier's series and integrals" New

York, Dover Publications Inc. 1930.

De Cogan D., O'Connor W. J. and Pulko S. “Transmission Line Matrix in Computational Mechanics” Taylor and Francis Group, New York 2006.

Hofer W. J. R. “Numerical Techniques for microwave and millimeter-wave Passive Structures” John Wiley and Sons Inc., New York Chapter 8 (edited by T. Itoh) 1989.

Johns P. B. “symmetrical condensed node for the TLM method” IEEE Trans. Microwave Theory Tech., vol. **MTT-35** pp. 370-377 1987.

Johns P. B. and Beurle R. L. “Numerical Solution of 2-Dimensional Scattering Problems using a transmission line matrix” Proc. Inst. Electr. Eng., **118**, 1203-1208 1971.

Appendix C: MRI Theory

C.1 Introduction to Magnetic Resonance Imaging

The basis for magnetic resonance imaging (MRI) is that a nucleus can have a magnetic moment μ. The magnetic moment arises due to circulating currents within nuclei and is a measure of the strength of a systems net magnetic source. An intrinsic property of many nuclei is angular momentum **I** called spin. The spin of a nucleus is measured in units of Planks constant $\hbar$. The discussion herein will be limited to those nuclei for which **I** = ½. For any given nucleus there is a given ratio, called the magnetogyric ratio γ, between the spin angular momentum and the magnetic moment.

$$\gamma = \mu / \mathbf{I}\hbar \qquad \text{(C.1)}$$

The magnetogyric ratio is an important constant (for a given nucleus) in the formation of an MRI image. The generation of an MRI image can be categorized into three principal stages: preparation, excitation and acquisition.

C.2 Excitation Process

Consider a number of nuclei whose magnetic moments are randomly oriented, as shown in Figure B.1(A), such a situation occurs under no externally applied interaction. Suppose a uniform and static magnetic field B_0 is applied to the magnetic moments, the magnetization vectors M, of the nuclei will orient themselves either parallel or anti-parallel to this field, as shown in Figure C.1(B).

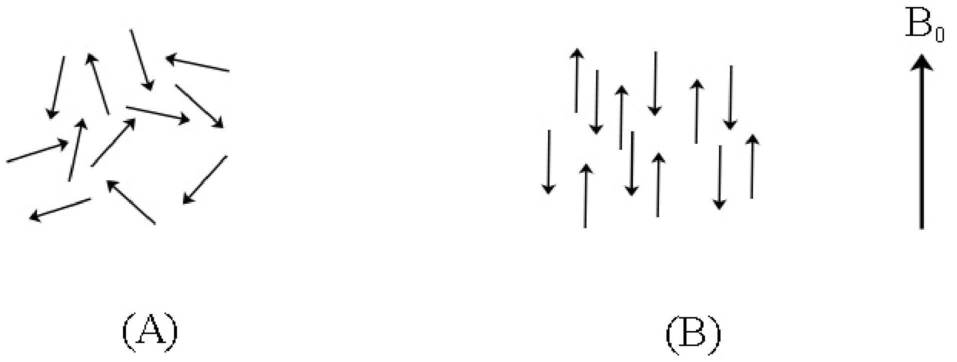

Figure C.1: Distribution of nuclear magnets (A) in thermal equilibrium and (B) in an externally applied magnetic field.

In terms of energy levels, the moments parallel to the B_0 field reside at a lower energy, as shown in Figure C.2.

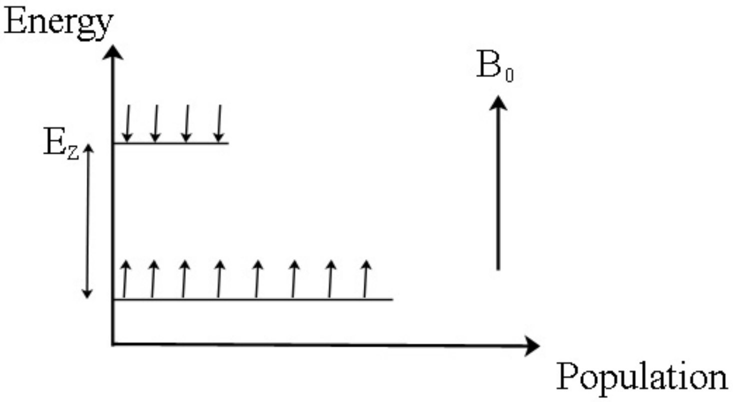

Figure C.2: Energy level diagram of magnetic moments in an externally applied magnetic field B_0.

At some temperature, T, the ratio of the number of moments anti-parallel, $n_{\downarrow}$, to those which are parallel, $n_{\uparrow}$, is given by the Boltzman factor [Nishimura 1996]:

$$\frac{n_{\downarrow}}{n_{\uparrow}} = e^{-E_Z / kT} \tag{C.2}$$

Where k is Boltzmann's constant and E_Z is the energy difference between a moment anti-parallel to one which is parallel, as illustrated in Figure C.2. At the macroscopic level the nuclei can be considered to act with a net magnetization given by the difference in moments parallel to those anti-parallel to the applied B_0 field.

C.2.1 Energy, Magnetization and Larmor frequency

The energy of a nuclear magnetic moment in the externally applied B_0 field is given by:

$$E = -\mu \cdot B_0 = -\gamma \mathbf{I} \hbar B_0 \qquad \text{(C.3)}$$

For a spin ½ nucleus the spin angular momentum is quantized to values of ± ½. The nuclei aligned anti-parallel are in the spin -½ state while the spin parallel to the B_0 field are in the spin ½ state. By Equation (C.3) the difference in energy, E_Z, between the two spin states is given by:

$$E_Z = E_{-1/2} - E_{+1/2} = \gamma \hbar B_0 \qquad \text{(C.4)}$$

The difference in energy levels is therefore dependent on the magnetogyric ratio for a given nucleus and the strength of the applied field B_0. This small difference in energy leads to an overall net magnetization, the difference can be calculated using Equations C.4 and C.2 (γ for Hydrogen nuclei is 267.4 radians$T^{-1}s^{-1}$). The strength of the net magnetization is given by [Nishimura 1996]:

$$M = \frac{N\gamma^2 \hbar^2 I(I+1) B_0}{3kT} \qquad \text{(C.5)}$$

Where N is the relative spin excess. Equation C.5 directly illustrates that stronger magnetic fields and larger magnetogyric ratios will produce larger net magnetizations.

From the energy difference, given in Equation B.4, we can also determine the frequency at which the nuclei possess a resonance. Using the relationship E = hν we have:

$$\omega_0 = \gamma B_0 \tag{C.6}$$

This frequency is known as the Larmor frequency.

C.2.2 Radio Frequency Field (B_1)

After the sample to be imaged has been placed in the B_0 field, an equilibrium state with the net magnetization along the field as depicted in Figure C.3 (A) is reached. In order to obtain an MRI image a second radio frequency field B_1 is applied in the x-y plane. This B_1 field is applied as a pulse of given duration. The applied field B_1 produces a torque on the net magnetization having the effect of spiraling the net magnetization into the x-y plane (as illustrated in Figure C.3 (B)).

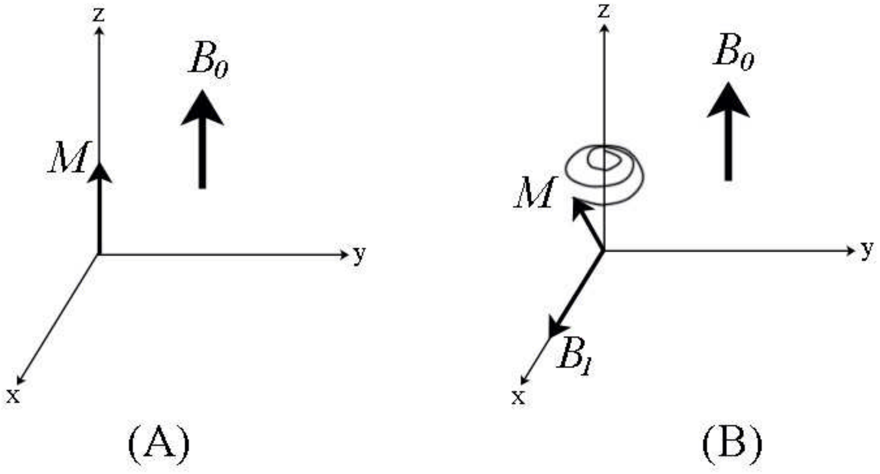

Figure C.3: (A) Magnetization vector in the B_0 field and (B) magnetization vector in the B_0 field as well as an externally applied RF field B_1.

C.2.3 Excitation

The equation of motion describing the excitation process is given by:

$$\frac{dM}{dt} = \gamma M \times B_{tot} \tag{C.7}$$

For which $B_{tot} = B_1 \cos(\omega t)\hat{x} + B_2 \sin(\omega t)\hat{y} + B_0 \hat{z}$. The two independent fields produce torques on the net magnetization leading to rotations about the longitudinal (z axis) and the transverse axes. Generally to simplify the mathematics, Equation C.7 is solved in a reference frame which rotates with the B_1 field. Under this condition, it can be shown that the equation of motion in the rotating reference frame is:

$$\frac{dM_\rho}{dt} = \gamma M_\rho \times \vec{B}_{eff} \tag{C.8}$$

Where $\vec{B}_{eff} = B_1 \hat{x}_p + (B_0 + \omega / \gamma)\hat{z}_\rho$ and the subscript ρ denotes the rotating reference frame. The net magnetization M_ρ will precess on the surface of a cone around the effective field at a frequency $\omega_{eff} = \gamma B_{eff}$. A resonance will occur when $B_0 + \omega/\gamma = 0$, under this condition the effective field is the RF field B_1. When B_1 is in the x_ρ direction the cone of precession will flatten to the $z_\rho y_\rho$ plane and M rotates in that plane around B_1 at a frequency $\omega = \gamma B_1$. The flip angle is known as the angle which M is deflected from its original z direction. The magnitude of the flip angle is given by:

$$\theta = \omega_{eff} t_{rf} = \gamma B_1 t_{rf} \tag{C.9}$$

The flip angle depends directly on the length of time it is applied and the strength of the RF field applied.

C.3 Bloch Equation and MRI Contrast Mechanisms

After the net magnetization has been excited into the x-y plane and the RF field is turned off it will slowly return to its equilibrium direction along the z-axis. The Equation which can be used to phenomenologically calculate the nuclear magnetization as a function of time is known as the Bloch Equation and is given by [Nishimura 1996]:

$$\frac{dM}{dt} = M \times \gamma B - \frac{M_x \hat{x} + M_y \hat{y}}{T_2} - \frac{(M_z - M_0)\hat{z}}{T_1} \qquad \text{(C.10)}$$

Where T_1 is the spin-lattice (longitudinal) relaxation time constant, T_2 is the spin-spin (transverse) relaxation time constant and M_0 is the net magnetization at equilibrium under the influence of the B_0 field.

C.3.1 Longitudinal Relaxation (T_1)

If we only consider the third term in Equation (C.10) then the solution to the Equation has an exponential form with a decay time constant T_1. A plot of the magnetization M_Z as a function of time after a 90^0 pulse or a 180^0 pulse is shown in Figure C.4.

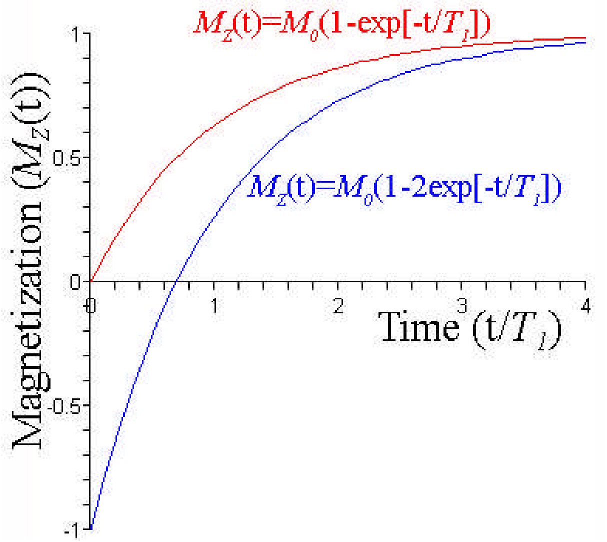

Figure C.4: Relaxation of the net magnetization back to the z-axis after a 90^0 flip, red curve, and a 180^0 inversion, blue curve (the plot is normalized to $M_z = 1$).

The physical mechanism giving rise to T_1 relaxation is spin-lattice interactions. A nucleus excited by the RF pulse is in a higher energy state than neighboring nuclei. While returning to equilibrium the nuclei in the higher energy state will share its excess energy with neighboring nuclei, the lattice.

C.3.2 Transverse Relaxation (T_2)

To this point we have assumed that the B_0 field is perfectly uniform. This however is not realistic; a real system will have local perturbations which vary both in time and space. These perturbations may be caused by small local fields caused by nuclear dipoles or electrons. In this case the field will be given by $B_{eff} = B_0 + b(x,y,x,t)$. In such a field the individual spins will precess at different frequencies and de-phase; as given by Equation C.6. The result of this de-phasing is a decay of the excited nuclei, M_{xy}, back to its equilibrium value. The rate equation describing this phenomenon is given by the middle term on the right hand side of Equation C.10. A plot of the decay of the transverse magnetization is shown in Figure C.5.

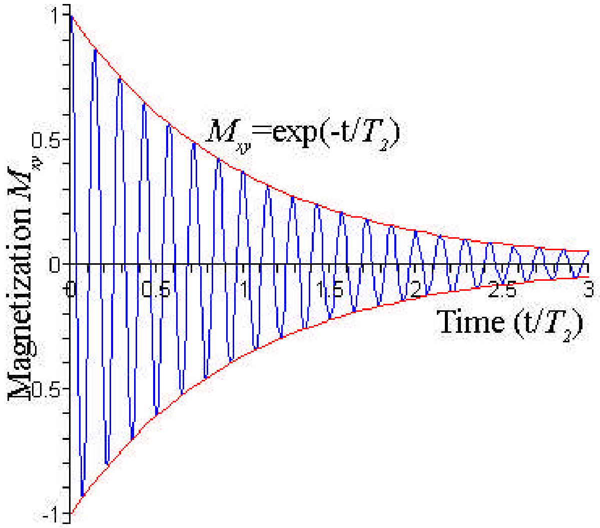

Figure C.5: Plot of the transverse magnetization, red curve, as a function of time. Also shown, in blue, is the detected signal as a function of time; this signal is known as the free induction decay.

Also shown, in blue, in Figure C.5, is a plot of the signal a receive coil would measure as a function of time; the oscillations result from nuclear spins not being in phase with the receiver. The shape of the detected signal is known as the free induction decay. In biological tissues, general values for T_2 are $\leq$ 100 ms, while for protons in water T_1 ~ 1 second.

A further source of magnetic field inhomogeneties results from the magnetic field itself not being homogenous. The field itself will have variations in all three spatial dimensions. These further field inhomogeneties lead to a second de-phasing constant known as T_2'. Together, T_2 and T_2' can be combined into one de-phasing constant known as T_2^*, in which:

$$\frac{1}{T_2^*} = \frac{1}{T_2} + \frac{1}{T_2'}. \qquad (C.11)$$

The inclusion of inhomogeneties in the main field will change the observed decay, shown in Figure C.5, to one with a smaller decay time.

C.4 Gradient Echo Imaging Sequence

Many imaging sequences which are designed to maximize different image contrast agents exist. The images acquired in this thesis were done using a gradient echo (GE) sequence. A GE sequence is shown in Figure C.6.

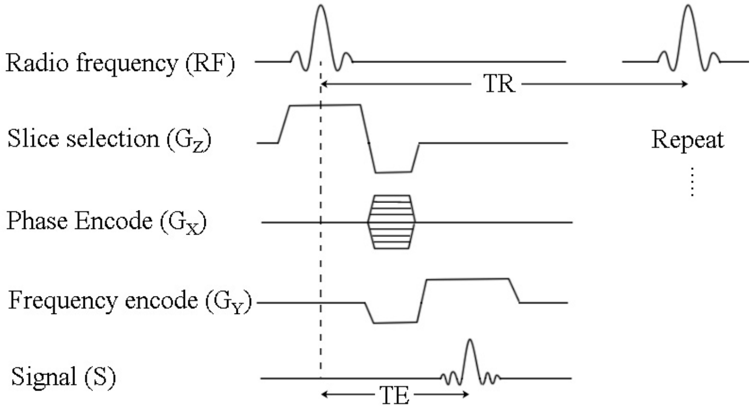

Figure C.6: Gradient echo sequence, showing the signals used to acquire a magnetic resonance image.

A RF signal is applied while at the same time a slice selection pulse is applied. The slice selection pulse produces a small gradient in the same direction as the B_0 field. The purpose of the slice selection gradient is to spread the frequencies of the spins in the material. The RF Pulse applied is a sinc pulse, which is a rectangular distribution in frequency space. Only those spins at the frequencies within the band of the sinc pulse will be excited; in this way a slice in a material is selected. After excitation a phase encode gradient is applied, the phase encode gradient alters the phase of the precession of M_{xy} as a function of position within the slice. It does this by temporarily altering the local Larmor frequency; once the difference in phase has been acquired the gradient is turned off. The frequency encode pulse is applied at the same time of signal readout. The frequency encode gradient is applied to alter the local field, and therefore Larmor frequency, of the spins in a direction perpendicular to the phase encode direction. The combination of the phase and frequency encoding provides two dimensional information within the slice.

C.5 Reference

Nishimura D. G. “Principles of magnetic resonance imaging” Stanford University 1996.

Appendix D: SPICE Theory

D.1 Nodal Analysis

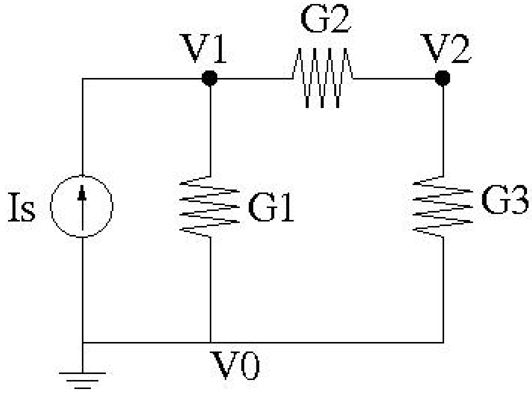

Figure D.2: Simple circuit used to demonstrate the use of nodal analysis.

SPICE uses nodal analysis to determine the matrix equations needed to solve the user's circuit. Kirchoff's current law (KCL) states that the sum of the currents leaving any node equals zero. As a simple example consider the circuit shown in D.1. In Figure D.1 the conductance is shown (conductance *G* = *1/R*) and a current source *Is* drives the network. Using KCL to describe the circuit at nodes 1 and 2, shown as *V1* and *V2* in Figure D.1, we have:

$$(V1 - V0)G1 + (V1 - V2)G2 = Is \text{ and} \tag{D.1}$$

$$(V2 - V1)G2 + (V2 - V0)G3 = 0 \tag{D.2}$$

where *V0* = 0 and so can be eliminated from the equations. These nodal equations can be put into matrix form as follows:

$$\begin{pmatrix} G1 + G2 & -G2 \\ -G2 & G2 + G3 \end{pmatrix} \begin{pmatrix} V1 \\ V2 \end{pmatrix} = \begin{pmatrix} Is \\ 0 \end{pmatrix}. \tag{D.3}$$

Using matrix methods, such as Gaussian elimination or LU factorization, and with knowledge of the source strength, *Is*, and the conductance's *G1*, *G2* and *G3* the voltages *V1* and *V2* can now be solved for. Nodal analysis is the basis of the setup of the problem in SPICE.

D.2 Numeric Integration

Two integration techniques are available using MultiSIM: trapezoidal or Gear. The trapezoidal integration technique is given by:

$$V_{n+1} = V_n + \frac{h}{2}\left(V'_{n+1} + V'_n\right) \tag{D.4}$$

where V_n is the voltage at the n^th^ time step, V'_n is the time derivative and h is the time step size between times n and $n+1$. This technique uses the slopes at the current point and the next time step to predict the voltage at the next time step.

The Gear integration formula is [McCalla 1988]:

$$V_{n+1} = \frac{4}{3}V_n - \frac{1}{3}V_{n-1} + \frac{2h}{3}V'_{n+1}. \tag{D.5}$$

This technique uses the voltages at the current and previous time steps along with the slope at the future time step are used to determine the voltage at the next time step.

D.3 Implementation of the Gear or Trapezoidal Technique

A linear system of equations which take the form:

$$x' = Ax + w\ . \tag{D.6}$$

In Equation D.6 w might represent a source, x and x' could represent a voltage and its time derivative and A a matrix of coefficients such as conductance values. As an example see section D.6, specifically Equation D.19. Since voltages and currents vary in time Equation D.6 can be discretized in time as follows:

$$x'_{n+1} = Ax_{n+1} + w_{n+1} \,. \tag{D.7}$$

Implementing the trapezoidal rule (Equation D.4) to eliminate the time derivative in Equation D.7 we have:

$$\left(1 - \frac{hA}{2}\right)V_{n+1} = \left(1 + \frac{hA}{2}\right)V_n + \frac{h}{2}\left(w_n + w_{n+1}\right). \tag{D.8}$$

An example illustrating the use of the gear or trapezoidal technique is illustrated in section D.6.

D.4 Companion Model for Inductors and Capacitors

Companion models are models which remove the time dependence of the current through a capacitor (I = CdV/dt) and the voltage across an inductor (V = LdI/dt) for one time step. The trapezoidal (or Gear) integration techniques can be used to simplify a capacitor to an equivalent impedance and current source in parallel (if the Norton representation is used) or an equivalent impedance in series with a voltage source (if the Thevenin representation is used). By using the Trapezoidal formula to removing the time derivative in Equation D.4 we have for a capacitor:

$$V_{n+1} = V_n + \frac{h}{2}\left(\frac{I_{n+1}}{C} + \frac{I_n}{C}\right) \tag{D.9a}$$

or

$$I_{n+1} = \frac{2C}{h}V_{n+1} - \frac{2C}{h}V_n - I_n \,. \tag{D.9b}$$

Equations D.9a and D.9b can be represented as a circuit as shown in Figure D.2.

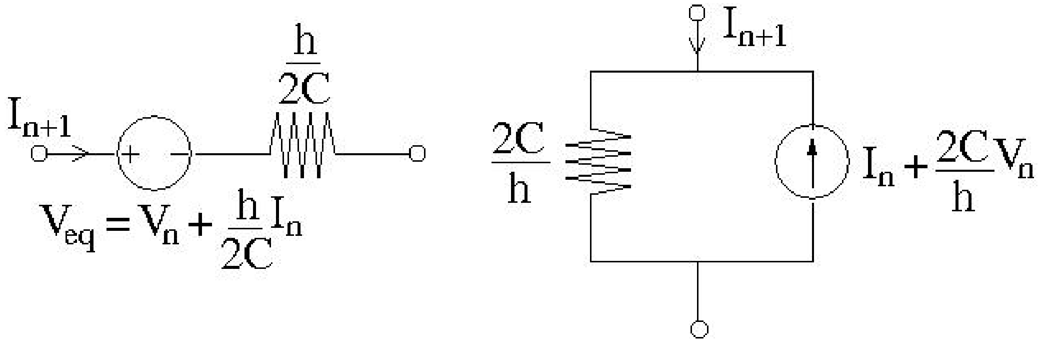

Figure D.2: Companion models for a capacitor. A capacitor can be modeled as one of the above equivalent circuits and is updated for each time step.

Similarly the trapezoidal rule can be used to remove the time dependence on the voltage across the inductor. Replacing the time derivative of the current yields:

$$I_{n+1} = I_n + \frac{h}{2}\left(\frac{V_{n+1}}{L} + \frac{V_n}{L}\right) \tag{D.10a}$$

or

$$V_{n+1} = \frac{2L}{h} I_{n+1} - \frac{2L}{h} I_n - V_n \,. \tag{D.10b}$$

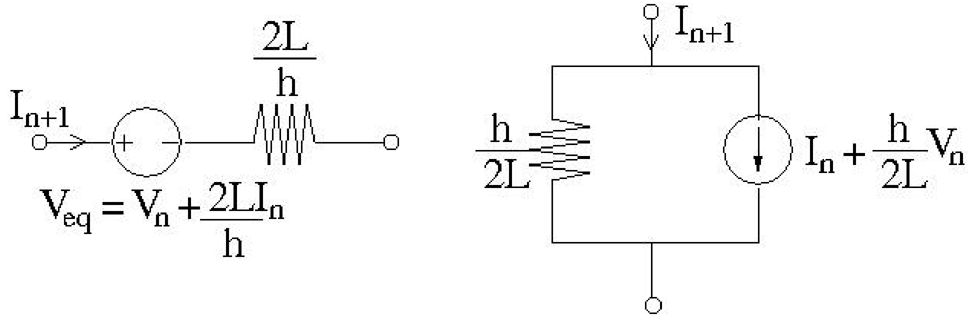

Figure D.3: Companion models for an inductor. An inductor can be modeled as one of the above equivalent circuits and is updated for each time step.

An inductor or capacitor can be replaced by their companion models whose controlled source model values are updated at each time step. This procedure removes the time dependence and nodal analysis can be used to solve the circuit.

D.5 Newton-Raphson Iteration

Newton-Raphson iteration is used to solve an equation or a system of equations for which $\vec{f}(\vec{x}) = 0$, the iterative process used is given by:

$$x^{k+1} = x^k - \frac{f(x^k)}{f'(x^k)}. \tag{D.11}$$

Where $f'(x^k)$ is the first derivative of *f(x)*, with respect to *x*, *k* is the iteration step and an initial guess x^0 is needed to start the iterative process. Equation D.11 is a Taylor expansion of the function *f(x)* about *x*. For an electronic problem, *x* in equation D.11 could represent a voltage and *f* a function of voltages across elements in the circuit.

Consider the system of non-linear equations (for example a system of nodal equations for which the total current out of a node is zero) given by:

$$\begin{gathered} f_1(x_1, x_2 \ldots x_n) = 0 \\ f_2(x_1, x_2 \ldots x_n) = 0 \\ \vdots \\ f_n(x_1, x_2 \ldots x_n) = 0 \end{gathered} . \tag{D.12}$$

Assuming the system of equations has a solution, which we denote by $\vec{x}^s$, expanding each function about $\vec{x}$:

$$\begin{aligned}
f_1(\vec{x}^s) &= f_1(\vec{x}) + \frac{\partial f_1}{\partial x_1}(x_1^s - x_1) + \frac{\partial f_1}{\partial x_2}(x_2^s - x_2) + \ldots \frac{\partial f_1}{\partial x_n}(x_n^s - x_n) + \ldots \\
f_2(\vec{x}^s) &= f_2(\vec{x}) + \frac{\partial f_2}{\partial x_1}(x_1^s - x_1) + \frac{\partial f_2}{\partial x_2}(x_2^s - x_2) + \ldots \frac{\partial f_2}{\partial x_n}(x_n^s - x_n) + \ldots \\
&\vdots \\
f_n(\vec{x}^s) &= f_n(\vec{x}) + \frac{\partial f_n}{\partial x_1}(x_1^s - x_1) + \frac{\partial f_n}{\partial x_2}(x_2^s - x_2) + \ldots \frac{\partial f_n}{\partial x_n}(x_n^s - x_n) + \ldots
\end{aligned} \tag{D.13}$$

If the expansion points, $\vec{x}$, are close to the solution $\vec{x}^s$, then formulate the approximation:

$$\vec{f}(\vec{x}^s) \approx \vec{f}(\vec{x}) + \vec{M}(\vec{x}^s - \vec{x}) \tag{D.14}$$

where $\vec{M}$ is the Jacobian matrix given by:

$$\vec{M} = \begin{pmatrix} \frac{\partial f_1}{\partial x_1} & \frac{\partial f_1}{\partial x_2} & \cdots & \frac{\partial f_1}{\partial x_n} \\ \frac{\partial f_2}{\partial x_1} & \frac{\partial f_2}{\partial x_2} & \cdots & \frac{\partial f_2}{\partial x_n} \\ \vdots & \vdots & & \vdots \\ \frac{\partial f_n}{\partial x_1} & \frac{\partial f_n}{\partial x_2} & \cdots & \frac{\partial f_n}{\partial x_n} \end{pmatrix}. \tag{D.15}$$

By using superscripts to indicate an iteration sequence equation D.14 can be written as:

$$\vec{f}(\vec{x}^k) + \vec{M}(\vec{x}^{k+1} - x^k) = 0 \,. \tag{D.16}$$

Given the values of the function *f* and its derivative the difference from the current to next time step can be determined. An example of the solution to a non-linear circuit problem is illustrated in section D.7.

The iterative process is as follows:

- Assume an initial guess at the solution.
- Linearize non-linear elements.
- Assemble linearized circuit equations.

- Solve system of linear circuit equations.
- Compare solution with last guess.

If the difference between consecutive iterations is larger than the error tolerance, then the current solution becomes the guess for the next iteration. If the difference in consecutive iterations is smaller than a user defined error tolerance a solution is reached.

D.6 Illustration of Nodal Analysis

To illustrate the technique consider the circuit shown in Figure D.4.

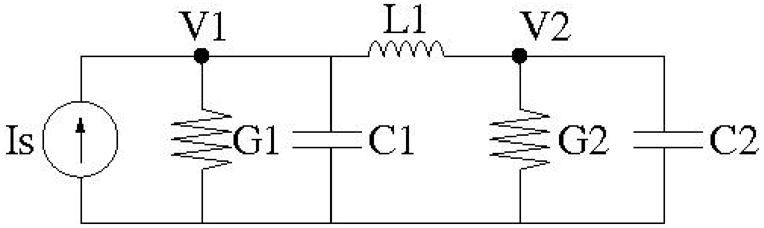

Figure D.4: Circuit used to illustrate the use of the trapezoidal rule.

Once again we use nodal equations to describe the circuit. This time however we also require an auxiliary equation. The current through a capacitor can be related to the time derivative of the voltage across the capacitor, the current through the inductor is related to the integral of the voltage across the inductor. However the voltage across the inductor is related to the time derivative of the current through the inductor. We have:

$$G_1 V_1 + C_1 \dot{V}_1 + I_{L1} = I_S \tag{D.17a}$$

$$G_2 V_2 + C_2 \dot{V}_2 - I_{L1} = 0 \tag{D.17b}$$

$$V_1 - V_2 - L \dot{I}_{L1} = 0 \,. \tag{D.17c}$$

Where I_{L1} is the current through the inductor *L1* and equations (D.17a) and (D.17b) result from applying KVL at the nodes shown as *V1* and *V2*. Equation (D.17c) is the auxiliary equation as determined by relating the voltage across the inductor to the time derivative if the current through the inductor. This can be written as:

$$\begin{pmatrix} C_1 & 0 & 0 \\ 0 & C_2 & 0 \\ 0 & 0 & L_1 \end{pmatrix} \begin{pmatrix} \dot{V}_1 \\ \dot{V}_2 \\ \dot{I}_{L1} \end{pmatrix} = \begin{pmatrix} -G_1 & 0 & -1 \\ 0 & -G_2 & -1 \\ 0 & -1 & 0 \end{pmatrix} \begin{pmatrix} V_1 \\ V_2 \\ I_{L1} \end{pmatrix} + \begin{pmatrix} I_S \\ 0 \\ 0 \end{pmatrix} \qquad \text{(D.18)}$$

Upon inverting the first matrix on the left hand side of Equation (D.18) and performing the matrix multiplication on the right hand side we get:

$$\begin{pmatrix} \dot{V}_1 \\ \dot{V}_2 \\ \dot{I}_{L1} \end{pmatrix} = \begin{pmatrix} G_1/C_1 & 0 & -1/C_1 \\ 0 & -G_2/C_2 & 1/C_2 \\ 0 & -1/C_1 & 0 \end{pmatrix} \begin{pmatrix} V_1 \\ V_2 \\ I_{L1} \end{pmatrix} + \begin{pmatrix} I_S/C_1 \\ 0 \\ 0 \end{pmatrix} \qquad \text{(D.19)}$$

This is of the form given by Equation (D.6) and can thus be solved using Equation (D.8). For the Gear integration technique a similar equation to Equation (D.8) can be derived.

D.7 SPICE Method

As an example of a solution to an electronic non-linear problem consider the circuit shown in Figure D.5.

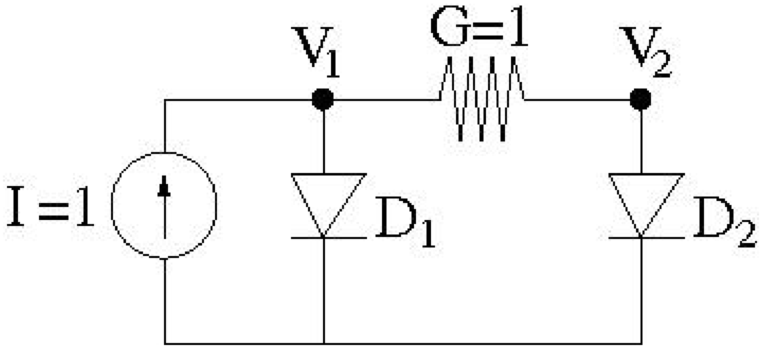

Figure D.5: Example of the use of the Newton-Raphson algorithm used to solve a non-linear system of equations.

Assume the current through the diodes has the relationship $I_D = e^{40V_d} - 1$, where V_d is the voltage across the diode. The nodal equations are:

$$\begin{aligned} I_{D1} + G(V_1 - V_2) &= I \\ G(V_2 - V_1) + I_{D2} &= 0 \end{aligned} \qquad \text{(D.20)}$$

This can be written in the same form as Equation (D.12):

$$\begin{aligned} f_1(V_1, V_2) &= e^{40V1} + V_1 - V_2 - 2 = 0 \\ f_2(V_1, V_2) &= -V_1 + V_2 + e^{40V2} - 1 = 0 \end{aligned} \qquad \text{(D.21)}$$

The Jacobian, $\vec{M}$ is:

$$\vec{M} = \begin{pmatrix} 40e^{40V1} + 1 & -1 \\ -1 & 40e^{40V2} + 1 \end{pmatrix} \qquad \text{(D.22)}$$

An initial estimate is needed before the iterative process can be run. We assume the initial values $V_1^0 = V_2^0 = 0.1$. Evaluation of Equation (D.21) at these initial estimates leads to $f_1 = 52.59815$, $f_2 = 53.59815$ and

$$\vec{M} = \begin{pmatrix} 2184.926 & -1 \\ -1 & 2184.926 \end{pmatrix} \qquad \text{(D.23)}$$

Equation (D.16) and our initial estimates can now be used to determine the values of V_1^1 and V_2^1. Doing this we obtain $V_1^1 = 0.12454$ and $V_2^1 = 0.12408$, these values are now used as our estimates for the next iteration. The procedure is the same as we have followed above, the values for f_1,f_2 and $\vec{M}$ are determined at the new points. From these values Equation (4.16) is used to determine our new values V_1^2 and V_2^2.

D.8 Reference

McCalla J. “Fundamentals of Computer-Aided Circuit Simulation” Kluwer Academic Publishers, Boston 1987.

Appendix E: Measurements of the Electromagnetic Field Strengths from a Siemens MD2 Mevatron Modulator

E.1 Introduction

The limit of RF exposure to workers is governed by health Canada. Specifically Safety Code 6 “Limits of Human Exposure to Radiofrequency Electromagnetic Fields in the Frequency Range from 3 KHZ to 300 GHZ” is a document which outlines the maximum RF limits, the method to measure RF noise and other safety considerations concerning RF exposure.

E.2 Purpose

To measure the electromagnetic field strength emissions from a Siemens modulator while the modulator produced microwave power in a pulsed fashion.

E.3 Theory

When the source contains more than one frequency the limit to an RF worker must satisfy the condition:

$$\sum_{f=3kHz}^{300GHz} R_f \leq 1$$

Where f is the frequency at which measurements were taken and:

$$R_f = \left(\frac{Measured\ Value\ of\ Field\ Strength\ at\ f}{Exposure\ Limit\ of\ Field\ Strength\ at\ f} \right)$$

Table E.1: Exposure limits for persons not classified as RF workers and microwave exposed workers (including the general public), taken from Reference [Safe_code_6].

Frequency (MHz)	Electric Field Strength; rms (V/m)	Magnetic field strength; rms (A/m)	Power Density (W/m^2)	Averaging time (min)
0.003-1	280	2.19		6
1-10	280/f	219/f		6
10-30	28	2.19/f		6
30-300	28	0.073	2*	6
300-1500	$1.585f^{0.5}$	$0.0042f^{0.5}$	f/150	6
1500-15000	61.4	0.163	10	6
15000-150000	61.4	0.163	10	$616000/f^{1.2}$
150000-300000	$0.158f^{0.5}$	$4.21x10^{-4}f^{0.5}$	$6.67x10^{-5}f$	$616000/f^{1.2}$

* Power density limit is applicable at frequencies greater than 100 MHz

E.4 Materials

A Rhode and Schwarz field probe set HZ-11 were used to measure the electric and magnetic field strengths separately. The signal from the field probes was read into an Agilent DS06104A oscilloscope in the time domain. The software program DADiSP was used for data transfer and analysis.

E.5 Method

The method to be followed for the proper reporting of field emissions is as outlined in Reference Safe_code_6.

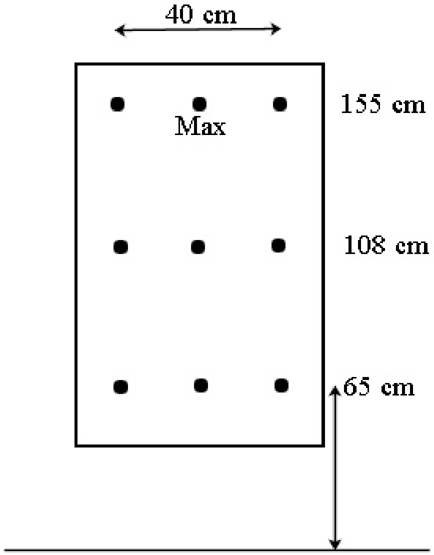

Figure E.1: Grid illustrating the points used to measure the fields from the modulator.

1. Initially the maximum field strength from the Siemens unit was determined by simply moving the field probes around the unit until a maximum signal was obtained.
2. Once the location of the maximum signal was obtained a grid around this signal is used to determine the average field. This grid is shown in Figure E.1.
3. The fields were measured at the nine points shown in Figure E.1 using the materials described above.
4. The average field strength for a grid of n points is given by:

$$F = \frac{1}{\sqrt{n}}\left[\sum_{i=1}^{n} F_i^2\right]^{1/2}$$

5. After being spatially averaged the data is then time averaged. The field strength at each frequency was determined by taking the Fourier transform over a 5µs window. (Note in this method the field strengths in the frequency domain are then those averaged over 5 µs). This window was enough to encompass all the noise emanating from the Siemens machine. The noise pulses came every 20.8 ms, therefore the data was multiplied by the factor (5 µs/20.8 ms) in order to get an average.

E.6 Results

Our measurements indicate values of $R_f = 0.0385$ for the electric field and $R_f = 0.010$ for the magnetic field.

E.7 Discussion

According to Reference [Safe_Code_6], RF workers shall not be exposed above the limits given in the table identified as “Exposure Limits for RF and Microwave Exposed Workers” in Reference [Safe_code_6]. In order to add an addition factor of safety, we have chosen to meet the limits in Table E.1 above. The limits given are for those which have been averaged both spatially and over time. Spatial and time averaging were done as described in methods.

E.8 Conclusions

The RF fields from the Siemens modulator have been shown to be well below the allowable limits for the general public. Working nearby the Siemens modulator is within the guidelines outlined by Safety code 6.

E.9 References

Safe_code_6, Environmental and workplace health: limits of human exposure to radiofrequency electromagnetic fields in the frequency range 3 kHz to 300 GHz-safety code 6. http://www.hc-sc.gc.ca/ewh-semt/pubs/radiation/99ehd-dhm237/index-eng.php

Bibliography

AAPM report 20. “Site planning for magnetic resonance imaging systems” NMR task group no. 2 1986 159

Allen R., Mallik A. and Johns P. B. “Numerical results for the symmetrical condensed TLM node” IEEE Trans. Microwave Theory Tech. MTT-35 378-382 1987 196

Antonuk L. E., “Electronic Portal Imaging Devices: a Review and Historical Perspective of Contemporary Technologies and Research” Phys. Med. Biol. 47 R31-R65 2002 3

Antypas C. and Pantelis E. “Performance Evaluation of a CyberKnife G4 Image-Guided Robotic Stereotactic Radiosurgery System” Phys. Med. Biol. 53 4697-4718 2009 5

Aqil S. Postdoctoral researcher, University of Alberta, Dept. of Phys. Private communication 2008 .... 45, 47

Artignnan X., Smitsmans M. H., Lebsque J. V., Jaffray D. A., van Her M., Bartelink H. “Online Ultrasound Image Guidance for Radiotherapy of Prostate Cancer: Impact of Image Acquisition on Prostate Displacement” Int. J. Radiat. Oncol. Biol. Phys. 59 595-601 2004 7

Ashcraft C. and Grimes R. “SPOOLES: An object-oriented sparse matrix library” *Proceedings of the Ninth SIAM Conference on Parallel Processing.* SIAM, Philadelphia, 1999. Software available at http://www.netlib.org/linalg/spooles .. 96

Athey T.W., Stuchly M.A. and Stuchly S.S. “Measurement of the radio frequency of biological tissues with an open ended coaxial line, part 1” IEEE Trans. Microw. Theory Tech. **MTT-30** 82-86 1982 32

Balanis C. “Antenna Theory” John Wiley and Sons Inc., New Jersey 2005 .... 35, 48, 65, 172, 178, 186

Berenger J. P. “A perfectly matched layer for the absorption of electromagnetic waves” J. comp. phys. **114** 185-200 1994 40

Biggs P. J., Goitein M. and Russel M. D. “A diagnostic X ray field verification device for a 10 MV linear accelerator” Int. J. Radiat. Oncol. Biol. Phys. 11 635-643 1985 6

Booth J. T. and Zavgorodni S. F. “Set-up Error and Organ Motion Uncertainty: a Review” Aust. Phys. Eng. Sci. Med. 22 29-47 1999 1

Brabbins D., Martinez A., Yan D. et al. “A Dose Escalation Trial with the Adaptive Radiotherapy Process as a Delivery System in Localized Prostate Cancer: Analysis of Chronic Toxicity” Int. J. Radiat. Oncol. Biol. Phys. **61** 400-408 2005..143

Brenner S., Scott R. L. “The Mathematical Theory of Finite Element Methods” Springer 2005..95

Brown J. “A Ham’s guide to RFI, Ferrites, Baluns and Audio interfacing” Revision 3, Audio Systems Group Inc. http://audiosystemsgroup.com 2008.....150

Brown P., Treado T., Aiguier D. and Hansen T. “Upgrade of Varian’s high power microwave magnetron test facility” Power modulator symposium, Conference record of IEEE 61-64 1992 106

Bucci M. K., Bevan A. ans Roach M. “Advances in Radiation Therapy: Conventional to 3D, to IMRT, to 4D and Beyond” A. Cancer. J. Clin. 55 117-134 2005..2, 143

Burke B., Lamey M., Rathee S., Murray B. and Fallone B.G. “Radio frequency noise from clinical linear accelerators” Phys. Med. Biol. 54 2483-2492 2009. ....14, 26, 53, 133, 137, 158

Burke B. “Measurement of radio frequency emissions from a medical linac” University of Alberta M.Sc. thesis 2008 ....26, 42, 43, 51

Burke B., Rathee S. and Fallone B. G. “Radiation induced effects in an 8.5 MHz magnetic resonance imaging coil” Med. Phys. **36** 2495 2009b 160

Canadian Cancer Society (2004) http://www.cancer.ca/canada-wide/about%20cancer/cancer%20statistics/~/media/CCS/Canada%20wide/Files%20List/English%20files%20heading/pdf%20not%20in%20publications%20section/Canadian%20Cancer%20Statistics%20-%202004%20-%20EN%20-%20pdf_195986411.ashx..1

Canadian Cancer Society (2009) http://www.cancer.ca/canada-wide/about%20cancer/cancer%20statistics/~/media/CCS/Canada%20wide/Files%20List/English%20files%20heading/pdf%20not%20in%20publications%20section/Stats%202009E%20Cdn%20Cancer.ashx 1

Carslaw H.S. “introduction to the theory of Fourier’s series and integrals” New York, Dover Publications Inc. 1930...197

Chen H., Wu A., Brandner E.D., Heron D.E., Huq M.S., Yue N.J. and Chen W-C. “Dosimetric evaluations of the interplay effect in respiratory-gated intensity modulated radiation therapy” Med. Phys. **36** 893-903 2009 54

Chen L., Price R. A., Wang L., Li J., Qin L., McNeeley S. et al. “MRI-based

Treatment Planning for Radiotherapy: Dosimetric Verification for Prostate IMRT" Int. J. Radiat. Oncol. Biol. Phys. 60 636-647 2004 9

Ciarlet P. G. "The Finite Element Method for Elliptic Problems" North-Holland 1978... 95

Clement G. C. "A provisional ground conductivity map for Canada" Proc. IRE, **49** 1674-1678 1961 37

Collin R. E. "Antennas and Radio wave Propagation" McGraw Hill Book Company, New York, 1985 172

Collins G.B. "Microwave Magnetrons" McGraw Hill Book Company Inc. New York Radiation Laboratory series no. 6 1948 .... 100, 134

Dawson L. A. Sharpe M. B. "Image-Guided Radiotherapy: Rationale, Benefits and Limitations" Lancet Oncol. 7 848-858 2006... 2, 7

Daswon L. A. and Jaffray D. A. "Advances in Image-Guided Radiation Therapy" J. Clin. Oncol. 25 938-946 2007 2

Davis T. A. "A column pre-ordering strategy for the unsymmetric-pattern multifrontal method" ACM Transactions on Mathematical Software, **30**, no. 2, pp. 165-195 2004a 96

Davis T. A. "Algorithm 832: UMFPACK, an unsymmetric-pattern multifrontal method" ACM Transactions on Mathematical Software, **30**, no. 2, pp. 196-199 2004b.. 96

Davis T. A. and Duff I. S. "A combined unifrontal/multifrontal method for unsymmetric sparse matrices" ACM Transactions on Mathematical Software, **25**, no. 1, pp. 1-19 1999 96

Davis T. A. and Duff I. S. "An unsymmetric-pattern multifrontal method for sparse LU factorization" SIAM Journal on Matrix Analysis and Applications, **18**, no. 1, pp. 140-158 1997 96

Dempsey J. F. "An Image-Guided Device Providing 4D CINE MRI Simultaneous to Radiotherapy Delivery" J. Radiother. Prac. 5 179 2006.......................... 13, 143

Eisbruch A., Dawson L. A., Kim H. M. et al. "Conformal and Intensity Modulated Irradiation of Head and Neck Cancer: the Potential for Improved Target Irradiation, Salvary Gland Function and Quality of Life" Acta. Otorhinolaryngol Belg. 53 271-275 1999.. 2, 143

Erridge S.C, Seppenwoolde Y., Muller S.H., van Herk M., De Jaeger K., Belderbos J.S.A., Boersma L.J., Lebesque J.V. "Portal imaging to assess set-up errors, tumor motion and tumor shrinkage during conformal radiotherapy of non-small cell lung cancer” Radiother. Oncol. **66** 75-85 2003 143

Fallone B.G., Murray B., Rathee S., Stanescu T., Steciw S., Vidokovic S., Blosser E. and Tymofichuk D. “First MR images obtained during megavoltage photon irradiation from a prototype linac-MR system” Med. Phys. 36 2084-2088 2009 ... . 12, 68, 143, 146, 151, 159

Feldkamp L.A., Davis L. C. and Kress J. W. “Practical cone-beam algorithm” J. Opt. Soc. A. A6 612-619 1984 7

Feryster Inductive components manufacturer http://www.feryster.pl/polski/nanoperm.php?lang=en Visited July 2009 123

Geyger W. A. “Nonlinear-magnetic control devices: basic principles, characteristics, and applications” McGraw Hill book Company, New York 1964... 98

Ghilezan M., Yan D., Liand J. et al. “Online Image-Guided Intensity-modulated Radiotherapy for Prostate Cancer: How Much Improvement can we Expect? A Theoretical Assessment of Clinical Benefits and Potential Dose Escalation by Improving Precision and Accuracy of Radiation Delivery” Int. J. Radiat. Oncol. Biol. Phys. 60 1602-1610 2004 .... 2, 143

Glasoe G. N. and J. Lebacqz V. “Pulse Generators” MIT Radiation Laboratory Series, Boston Technical Publishers Inc. Lexington 1964 .... 104, 106, 108

Godfrey D. J., Yin F. F., Oldham M. et al. “Digital Tomosynthesis with an on-Board Kilovoltage Imaging Device” Int' J' Radiat. Oncol. Biol. Phys. 65 8-15 2006 8

Grant J. P., Clarke R. N. Symm G. T. and Spyrou N. M. “A critical study of the open ended coaxial line sensor technique for RF and microwave complex permittivity measurements” J. Phys. E: Sci. Instrum. **22** 757-770 1989 .... 26, 42

Hansen V. N., Evans P. M., Swindell W. “The Application of Transit Dosimetry to Precision Radiotherapy” Med. Phys. 23 713-721 1996 3

Hansen E.K., Bucci M.K., Quivey J.M, Weinberg V. and Xia P. Repeat CT imaging and replanning during the course of IMRT for head-and-neck cancer” Int. J. Radiat. Oncol. Biol. Phys. **64** 355-362 2006 143

Hector C. L., Webb S. and Evans P. M. “The dosimetric Consequences of Inter-Fractional Patient Movement on Conventional and Intensity-Modulated Breast Radiotherapy Treatments” Radiother. Oncol. 54 57-64 2000 1

Herman et al. “Clinical use of Electronic Portal Imaging: Report of AAPM Radiation Therapy Committee Task Group 58” Med. Phys. 28 712-737 2001 3

Hestenes M. R. and Stiefel E. “Methods of conjugate gradients for solving linear systems” J. Res. Nat. Bur. Standards, **49** 409-436 1954 97

Hill R. A. “Analysis of modulator design problems by simulation” Proc. 7th symp. On Hydrogen thyratrons IEEE 165-176 1962 106

Hofer W. J. R. “Numerical Techniques for microwave and millimeter-wave Passive Structures” John Wiley and Sons Inc., New York Chapter 8 (edited by T. Itoh) 1989 .... 189, 190

Hoisak J. D., Sixel K. E., Tirona R., Cheung P. C., and Pignol J. P. “Correlation of lung tumour motion with external surrogate indicators of respiration” Int. J. Radiat. Oncol. Biol. Phys. 60 1298-1306 2004 3

Holm R. “Theory of sparking during commutation on dynamos” Conf. Record-AIEE IAS Annual Meeting pp 588-595 1962 65

Holupka E. J., Kaplan I. D., Burdette E. C. et al. “Ultrasound Image Fusion for External Beam Radiotherapy for Prostate Cancer” Int. J. Radiat. Oncol. Biol. Phys. 35 975-984 1996 6

IEEE Antenna Standards Committee “IEEE Standard Methods for Measuring Electromagnetic Field Strength of Sinusoidal Continuous Waves, 30 Hz to 30 GHz” IEEE inc. 1991 .... 181, 182

IEEE Antenna Standards Committee “IEEE Standard Definitions of Terms for Antennas IEEE” inc. 1983 .... 182, 183

IEEE Electromagnetic compatibility committee “IEEE Standard Method for Measuring the Effectiveness of Electromagnetic Shielding Enclosures” IEEE std. 299. IEEE 3 Park Avenue New York 2006 .... 144, 149

ICRU50 “Prescribing, Recording and Reporting Photon Beam Therapy” ICRU Bethesda. MD, 1993 .... 9, 10

ICRU62 “Prescribing, Recording and Reporting Photon Beam Therapy (supplement to ICRU report 50)” ICRU Bethesda. MD, 1999 10

Jabbar M.A. “Radio frequency interference of electric motors and associated electronics” *IEEE trans. Ind. Appl.* **27** 27-31 1991 59

Jackson J. D. “Classical electrodynamics” John Wiley and Sons pp. 239-240 1999 .... 35, 170, 172

Jaffray D. A., Siewerdsen J. H., Wong J. W. and Martinez A. A. “A Flat Panel Cone-Beam Computed Tomography for Image Guided Radiation Therapy” Int. J. Radiat. Oncol. Biol. Phys. 53 1337-1349 2002 8

Jang S. D., Son Y. G., Oh J. S., Lee H. G., Bae Y. S., Cho M. H. and Namkung W. http://psl.postech.ac.kr/publication/dom_poster_phy/kapra_kpsdpp_2004_july_sdjang.pdf KAPRA 2004 presentation...106

Jin J. "The finite element method in electromagnetics" John Wiley and Sons, New York 2002...92

Johns P. B. "symmetrical condensed node for the TLM method" IEEE Trans. Microwave Theory Tech., vol. **MTT-35** pp. 370-377 1987..................................27

Johns P. B. and Beurle R. L. "Numerical Solution of 2-Dimensional Scattering Problems using a transmission line matrix" Proc. Inst. Electr. Eng., **118**, 1203-1208 1971...196

Jordan E. C. and Balmain K. G. "Electromagnetic waves and radiating systems" Prentice Hall Inc. New Jersey 1968 ....27, 34, 36, 37

King R. W. P. "Transmission lines, antennas and waveguides" McGraw Hill Company Inc., New York 1945..150, 172

Kirkby C., Stanescu T., Rathee S., Carlone M., Murray B. and Fallone B. G. "Patient dosimetry for hybrid MRI-radiotherapy systems" Med. Phys. 35 1019-1027 2008...13

Kraus J. D. "Antennas" McGraw Hill, New York, 1950 ....172, 185, 187

Kuo YC., Wu TH., Chung TS., Huang KW., Chao K.S.C., Su WC., Chiou JF. "Effect of regression of enlarged neck lymph nodes on radiation doses received by parotid glands during intensity-modulated radiotherapy for head and neck cancer" Am. J. Clin. Oncol. **29** 600-605 2006 143

Lagendijk J. J. W. et al. MRI/Linac Integration Radiother. Oncol. 86 25-29 2008 .. ..13, 143

Langden K. M. and Jones D. T. "Organ motion and its Management" Int. J. Radiat. Oncol. Biol. Phys. 50 265-278 2001 ....1, 143

Langen K. M., Pouliot J., Anezinos C. et al. "Evaluation of Ultrasound-Based Prostate Localization for Image-Guided Radiotherapy" Int. J. Radiat. Oncol. Biol. Phys. 57 635-644 2003 7

Langen K. M., Meeks S. L., Poole D. O. et al. "The use of Megavoltage CT (MVCT) Images for Dose Recomputations" Phys. Med. Biol. 50 4259-4276 2005 7

Lattanzi J., McNeeley S., Pinover W. et al. "A comparison of Daily CT Localization to a Daily Ultrasound-Based System in Prostate Cancer" Int. J. Radiat. Oncol. Biol. Phys. 43 719-725 1999 6

Leksell L. “The Sterotaxic Method and Radiosurgery of the Brain” Acta. Chir. Scand. 102 316-319 1951 4

Little R.P., Ruppel H. M. and Smith S. T. “Beam Noise in Crossed Electric and Magnetic Fields” J. Appl. Phys. **29** iss. 9, 1376-1377 1958 .... 100, 135

Litzenburg D. W., Willoughby T. R., Blater J. M. et al. “Positional Stability of Electromagnetic Transponders used for Prostate Localization and Continuous Real-Time Tracking” Int. J. Radiat. Oncol. Biol. Phys. 68 1199-1206 2007 4

Lorenz L. “Ueber die fortpflanzung der Electricitat” Wied. Ann. Vol. 7 161-193 1879.. 104

Mackie T. R., Holmes T., Swerdloff et al. “Tomotherapy: A New Concept for the Delivery of Dynamic Conformal Radiotherapy” Med. Phys. 20 1709-1719 1993 7

Mackie T. R., Balog J., Ruchala K., Shepard D. M., Aldridge K. S., Fitchard E. E. et al. “Tomotherapy” Semin Radiat. Oncol. 9 108-117 1999 7

Mackie T.R., Kapatoes J., Ruchala K., Lu W., Wu C., Olivera G. et al. “Image Guidance for Precise Conformal Radiotherapy” Int. J. Radiat. Oncol. Biol. Phys. 56 89-105 2003 2

Mageras G. S. “Introduction: Management of Target Localization Uncertainties in External-Beam Therapy” Semin. Radiat. Oncol. 15 133-135 2005........................ 2

Mah D., Steckner M., Palacio E., Mitra R., Richardson T. and Hanks G. E. “Characteristics and Quality Assurance of a Dedicated Open 0.23 T MRI for Radiation Therapy Simulation” Med. Phys. 29 2541-2547 2002 9

McBain C. A., Henry A. M., Sykes J. et al. “x-ray Volumetric Imaging in Image-Guided Radiotherapy: the new Standard in on Treatment Imaging” Int. J. Radiat. Oncol. Biol. Phys. 64 625-634 2006... 8

McCalla J. “Fundamentals of Computer-Aided Circuit Simulation” Kluwer Academic Publishers, Boston 1987 211

Meyer J. L., Verhey L., Xia P. and Wong J. “New Technologies in the Radiotherapy Clinic” pages 1-17 from “IMRT-IGRT-SBRT Advances in the Treatment Planning and Delivery of Radiotherapy” Front. Radiat. Ther. Oncol. 40 2007... 2, 143

Microstripes reference manual, Release 7.5, Copyright Flomerics 2006 40

Miller H. C. “Inductance formula for a single-layer circular coil” Proc. IEEE. **75** 256-257 1987 104

Monossov H. G. “The two-dimensional mathematical model of electron interaction with UHF field in a magnetron and high-voltage UHF oscillations breakdown” Elec. And Radiophys. of ultra high freq. Int. Univ. Conf. 97-100 1999.. 101

Neculaes V. B. Gilgenbach R. M. and Lau Y. Y. “Low-Noise microwave magnetrons by azmuthally varying axial magnetic field” Appl. Phys. Lett. **83** no. 10 1938-1940 2003 100

Nill S., Unkelbach J., Dietrich L. and Oelfke U. “Online correction for respiratory motion: evaluation of two different imaging geometries” Phys. Med. Biol. **50** 4087-4096 2005 59

Nishimura D. G. “Principles of magnetic resonance imaging” Stanford University 1996.. 201, 202, 205

Okress E. “Crossed-Field Microwave Devices” Academic Press New York 1961 .. .. 100, 134

Ott H. W. “Noise reduction techniques in electronic systems” John Wiley and Sons Inc. 1988... 54

Padmanabhan A. and Srinivsan A. “Some important aspects in the phenomenon of commutator sparking” IEEE Trans. **PAS 84** 396-404 1965................................. 65

Pavlicek W. and Meaney T. F. “The special environmental needs of magnetic resonance” Appl. Radio. **13** 23-33 1984 159

Podgorsak E. B., pike G. B., Oliver A., Pla M. and Souhami L. “Radiosurgery with high Energy Photon Beams: a Comparison among Techniques” Int’ J’ Radiat. Oncol. Biol. Phys. 16 857-865 1989... 4

Pollack A., Zagars G. K., Starkschall G. et al. “Prostate Cancer Radiation Dose Response: Results of the MD Anderson Phase III Randomized Trial” Int. J. Radiat. Oncol. Biol. Phys. 53 1097-1105 2002 143

Raaijmakers A. J. E., Raaymakers B. W. and Lagendijk J. J. W. “Magnetic-Field-Induced Dose Effects in MR-Guided Radiotherapy Systems: Dependence on the Magnetic Field Strength” Phys. Med. Biol. 53 909-923 2008............................. 13

Raaijmakers A. J. E. et al. “Dose Optimization for the MRI-Accelerator: IMRT in the Presence of a Magnetic Field” Phys. Med. Biol. 52 7045-7054 2007a 13

Raaijmakers A. J. E. “Integrating a MRI Scanner with a 6MV Radiotherapy Accelerator: Impact of the surface Orientation on the Entrance and Exit Dose due to the Transverse Magnetic Field” Phys. Med. Biol. 52 929-939 2007b............. 13

Raaijmakers A. J. E., Raaymakers B. W. and Lagendijk J. J. W. “Experimental Verification of Magnetic Field Dose Effects for the MRI-Accelerator” Phys. Med.

Biol. 52 4283-4291 2007c.. 13

Raaijmakers A. J. E., Raaymakers B. W. and Lagendijk J. J. W. “Integrating a MRI Scanner with a 6 MV Radiotherapy Accelerator: Dose Increase at Tissue-Air Interfaces in a Lateral Magnetic Field due to Returning Electrons” Phys. Med. Biol. 50 1363-1376 2005 13

Raaymakers B. W. et al. “Integrating a MRI Scanner with a 6 MV Radiotherapy Accelerator: Dose Deposition in a Transverse Magnetic Field” Phys. Med. Biol. 49 4109-4118 2004 13

Richardson B., Sheldrake R and Pirrie C. “Thyratron Grid Protection and Monitor System” 16th IEEE Pulsed Power Conference **1** 438-441 2007.......... 123, 132, 136

Rietzel E., Rosenthal S. J., Gierga D. P., Willet C. G. and Chen G. T. “Moving Targets: Detection and Tracking of Internal Organ Motion for Treatment Planning and Patient Set-up” Radiother. Oncol. 73 S68-S72 2004 .... 1, 143

Robert A. “Dielectric permittivity of concrete between 50 MHz and 1 GHz and GPR measurements for building materials evaluation” J. Appl. Geophys. 89-94 1998.. 53

Rosa E. B. and Grover F. W. “Formulas and tables for the calculation of mutual and self-inductance” Bulletin of the Bureau of standards, **6** 1 1912 105

Rzepecks and Stuchly S.S. “A lumped capacitance method for the measurement of the permittivity and conductivity in the frequency and time domain-a further analysis” IEEE Trans. Instrum. Meth. **IM-24** 27-32 1975 32

Saad Y. and Schultz M. H. “GMRES: A generalized minimal residual algorithm for solving nonsymmetric linear systems” SIAM J. Sci. Statist. Comput. **7** 856-869 1986.. 96

Safe_code_6, Environmental and workplace health: limits of human exposure to radiofrequency electromagnetic fields in the frequency range 3 kHz to 300 GHz-safety code 6. http://www.hc-sc.gc.ca/ewh-semt/pubs/radiation/99ehd-dhm237/index-eng.php 221, 222, 223

Sawant A., Venkat R., Srivastava V., Carlson D., Povzner S., Cattell H. and Keall P. “Management of three-dimensional intrafraction motion through real-time DMLC tracking” Med. Phys. **35** (5) 2050-2061 2008 59

Schenk O., Gärtner K. and Fichtner W. “Efficient sparse LU factorization with left-right looking strategy on shared memory multiprocessors” BIT, **40** no. 1158-176 2000.. 96

Schewe J. E., Lam K. L., Balter J. M. and Ten Haken R. K. “A room-based diagnostic imaging system for measurement of patient setup” Med. Phys. 24

2385-2387 1998 6

Seiler P. G., Blattman H., Kirsch S. et al. "A Novel Tracking Technique for the Continuous Precise Measurement of Tumour Positions in Conformal Radiotherapy" Phys. Med. Biol. 45 N103-N110 2000 4

Sharpe M. B., Craig T. and Moseley D. J. "Image Guidance: Treatment Target Localization Systems" pp72-93, 2007, From "IMRT-IGRT-SBRT Advances in the Treatment Planning and Delivery of Radiotherapy" Front. Radiat. Ther. Oncol. 40 2007.. 2, 6, 7

Shirato H., Shimizu S., Kitamura M., Nishioka T., Kagei K., Hashimoto S., Aoyama H., Kunieda T., Shinohara N., Dosaka-Akita H., Miyasaka K. "Four-dimensional treatment planning and fluoroscopic real-time tumour tracking radiotherapy for moving tumour" Int. J. Radiat. Oncol. Biol. Phys. 48 435-442 2000... 6

Shrivastava V., Ranga Y "Ultra wide band CPW-fed printed pentagonal antenna with modified ground plane for UWB applications" IET int. conf. wireless mobile and multimedia networks 1-2 2008.. 41

Singh M., Koul S.K., Basu A. "Coplanar Waveguide Fed Ultra Wide Band Monopole Antenna" RFM Int. RF and Mcirowave conf. 44-47 2006.................. 41

Sobol W. "General site requirements including RF and magnetic shielding" from "The physics of magnetic resonance imaging" AAPM summer school Banff, Alberta 1992 159

Song W., Schaly B., Bauman B., Battista J. and Van Dyk J. "Image-Guided Adaptive Radiation Therapy (IGART): Radiobiological and Dose Escalation Considerations for Localized Carcinoma of the Prostate" Med. Phys. 32 2193-2203 2005.. 2

Stratton J. A. "Electromagnetic theory" McGraw Hill, New York pp 457 2007 .. 66

Stutzman W. L. and Thiele G. A. "Antenna theory and design" John Wiley and Sons Inc. New York 1981 .... 34, 171, 172

Suriano C.R., Suriano J.R., Thiele G., Holmes T.W. "Prediction of radiated emissions from DC motors" *IEEE* Syp. Elec. Comp. **2** 790-795 1998 .... 59, 64, 81, 83, 84

Suriano J. R. "Modeling of electromechanical and electromagnetic disturbances in DC motors" IEEE Nat. Symp. Elect. Comp. Denver 258-262 1989 65

Toledo S., Chen D. and Rotkin V. "TAUCS a library of sparse library solvers" http://www.tau.ac.il/~stoledo/taucs/ visited August 2009.................................... 96

Torok L. “Precision inductance modeling is the basis for accurate PFN simulation” Conf. record of the 21st international power modulator symposium 1994.. 104

van Zijtveld M., Dirkx M. L., de Boer H. C., et al. “Dosimetric Pretreatment Verification of IMRT Using an EPID; Clinical Experience” Radiother. Oncol. 81 168-175 2006 3

Verellen D., De Ridder M., Linthout N., Tournel K., Soete G. and Storme G. “Innovations in Image-Guided Radiotherapy” Nature Rev. Cancer 7 949-960 2007 .... 2, 3, 8, 143

Verellen D., De Ridder M. and Storme G. “A (short) History of Image-Guided Radiotherapy” Radio. Oncol. 86 4-13 2008... 2, 143

Viewray Inc. http://www.viewray.com/index.php (Visited Feb. 12th 2008) 13

Webb S. and Bortfeld T. “A new way of adapting IMRT delivery fraction-by-fraction to cater for variable intrafraction motion” Phys. Med. Biol. **53** 5177-5191 2008.. 59

Webb S. “Quantification of the fluence error in the motion-compensated dynamic MLC (DMLC) technique for delivering intensity-modulated radiotherapy (IMRT)” Phys. Med. Biol. **51** L17-L21 2006a 59

Webb S. “Motion effects in (intensity modulated) radiation therapy: a review” Phys. Med. Biol. **51** R403-R425 2006b.. 143

Webb S. “The effect on IMRT conformality of elastic tissue movement and a practical suggestion for movement compensation via the modified dynamic multileaf collimator (dMLC) technique” Phys. Med. Biol. **50** 1163-1190 2005.. 59

Webb S. “The Physical Basis of IMRT and Inverse Planning” Br. J. Radiol. 76 678-689 2003 8

Weiner M. M. “Monopole Antennas” Marcel Dekker Inc., New York 2003........ 66

Welsh J. S., Bradley K., Ruchala K. J. et al. “Megavoltage Computed Tomography Imaging: a Potential Tool to Guide and Improve the Delivery of Thoracic Radiation Therapy” Clin. Lung Cancer 5 303-306 2004......................... 4

Wu A. “Physics and Dosimetry of the Gamma Knife” Neurosurg. Clin. N. Am. 3 35-50 1992 4

Valentine R. “Motor Control Electronics Handbook” McGraw Hill, New York 1998.. 82

van Herk M. “Errors and Margins in Radiotherapy” Sem. Rad. Oncol. **14** 52-64

2004.. 143

Varian Transformer specification, drawing number 829003 1972...................... 106

Varian course book “Varian generic accelerator course book” 2nd ed. Medical and industrial Products service, Education Dept. 1989... 107

Yin F. F. et al. “Image-guided procedures for intensity-modulated spinal radiosurgery” J. Neurosur. Suppl. 3 101 419-424 2004.. 5

Yu S. P. Kooyers G. P. and Buneman O. “Time-dependent computer analysis of electron-wave interaction in crossed fields” J. Appl. Phys. **36** 2550-2559 1965...... 101